5-2024

Experimental and Numerical Analysis of Laminar and Transitional Flow through Annular Corrugated Pipes

Joseph Russell Sargent
Florida Institute of Technology, jsargent2008@my.fit.edu

Experimental and Numerical Analysis of Laminar and Transitional Flow through Annular Corrugated Pipes

By

Joseph Russell Sargent

A dissertation submitted to the College of Engineering and Science of

Florida Institute of Technology

in partial fulfillment of the requirements

for the degree of

Doctor of Philosophy

in

Mechanical Engineering

Melbourne, Florida

May, 2024

We the undersigned committee hereby approve the attached dissertation, "Experimental and Numerical Analysis of Laminar and Transitional Flow through Annular Corrugated Pipes," by Joseph Russell Sargent.

_____

Daniel R. Kirk, Ph.D.
Professor
Aerospace, Physics and Space Sciences
Major Advisor

_____

David Fleming, Ph.D.
Professor and Program Chair
Aerospace, Physics and Space Sciences

_____

Paul Schallhorn, Ph.D.
VADR Technical Manager
NASA Launch Services Program

_____

Hamidreza Najafi, Ph.D.
Associate Professor
Mechanical and Civil Engineering

_____

Ilya Mingareev, Ph.D.
Assistant Professor
Mechanical and Civil Engineering

_____

Ashok Pandit, Ph.D., P.E.
Professor and Department Head
Mechanical and Civil Engineering

Abstract

Title: Experimental and Numerical Analysis of Laminar and Transitional Flow through Annular Corrugated Pipes

Author: Joseph Russell Sargent

Advisor: Daniel R. Kirk, Ph. D.

This dissertation presents studies on pressure loss through annular corrugated pipes to determine a friction factor coefficient using nitrogen. Ten different corrugated pipes' geometries were evaluated via testing and experimentation. The ratio of corrugation height to inner diameter varied from 0.233 to 0.333 and the ratio of corrugation pitch to inner diameter varied from 0.181 to 0.446. Nitrogen flow rates between 0.25 to 94.4 standard liters per minute were used, resulting in Reynolds numbers, based on the corrugated pipe inner diameter, from 100 to 23,000. The experimental set-up was validated using smooth-pipe pressure loss measurements and the derived friction factor showed good agreement with the Moody diagram. Experimental uncertainty analysis was conducted, including the correlated bias error terms, encompassing 95% bounds of the data collected and presented for both derived results Reynolds number and friction factor from the measured inputs. The current results indicate that pipes with smaller pitch to inner

diameter ratios transition closer to Re = 1,600. An example of the experimental result includes a corrugated pipe with an inner diameter of 8.64 mm and corrugation pitch of 2.41 mm, at Reynolds number of 300 +/- 7%, the resulting friction factor was 0.183 +/- 32%. Experiments were conducted with two-dimensional bends varying up to 16 in bend radius and 180 degrees. The resulting additional pressure loss due to the bend was within the uncertainty analysis errors and concluded that secondary flow effects are still secondary even for flow through corrugated pipes. CFD was conducted and a comparison of nine different turbulence models were compared with the k-ε (K-epsilon) producing the most accurate results of the differential pressure loss to the experiments conducted within ~10% on average.

Table of Contents

List of Keywords

corrugated

Darcy–Weisbach friction factor

density

incompressible flow

lines

(standard) mass flow rate

pipes

Reynolds Number

viscosity

(standard) volume flow rate

List of Figures

List of Tables

List of Abbreviations

2D	Two dimensional
3D	Three dimensional
AKN	Abe, Kondoh and Nagano Low Reynolds Number K-Epsilon (depreciated) Turbulence Model
CFD	Computational Fluid Dynamics
EMT	Electrical Metal Tubing
EU	Expanded Uncertainty = $\sqrt{SSU\text{^}2 + RSU\text{^}2}$
GFSSP	Generalized Fluid System Simulation Program developed by NASA Marshall Space Flight Center [1]
Hz	Hertz
ID	Inner diameter of corrugated pipe
in	inch
KE Standard	(k-ε) K-e psilon Turbulence Model
KO Standard	Standard (Wilcox) K-Omega Turbulence Model
kPa	kilopascals
LSP	Launch Services Program (NASA Kennedy Space Center) – Info Book, https://www.nasa.gov/kennedy/launch-services-program/
mm	millimeter
n	Total number of pressure ports installed on a pipe

NASA	National Aeronautics and Space Administration
NPT	National Pipe Taper, FNPT female, MNPT male
OD	Outer diameter of corrugated pipe
pg.	Page number
r	Result defined as the average differential pressure per unit length
Re	Reynolds number
Re Stresses	Reynolds Stress Transport Turbulence Model
RSU	Random Standard Uncertainty
SAS	Special Aerospace Services, https://specialaerospaceservices.com/
scfh	Standard cubic feet per hour
slpm	Standard liters per minute
SKE L RE	Standard K-Epsilon Low Reynolds Number Turbulence Model
Std	Standard atmosphere internal to this dissertation defined as 25°C and 14.696 psia
SSA	Standard Spalart-Allmaras Turbulence Model
SST M KO	Shear-Stress Transport (Menter) K-Omega Turbulence Model
SSU	Systematic Standard Uncertainty
ST W KO	Standard (Wilcox) K-Omega – Low Reynolds number damping modification Turbulence Model, Wilcox [102]

VADR	Venture-Class Acquisition of Dedicated and Rideshare Launch Services
V2F	turbulent viscosity based on velocity fluctuations K-Epsilon, Davidson [105]

List of Symbols

b_x	Estimate of the standard deviation of the distribution of the parent population from which a systematic error originates
B_x	Individual systematic errors
$[B_x B_y]_{corr}$	Correlated bias between systematic errors B_x and B_y
D_h	Hydraulic diameter
d_n	Distance measurement between ports
E	Corrugation height
ε	Absolute roughness
f	Darcy–Weisbach friction factor
“	inches
ID	Inner diameter of corrugated pipe
L	Length of pipe
M	Mach Number
n	Total number of static pressure ports installed on a pipe
OD	Outer diameter of corrugated pipe
ρ	density
P	Corrugation pitch or distance between corrugations
ΔP_n	Differential pressure measurement between ports
$P^2_{\Delta P_n}$	2*standard deviation of differential pressure readings
P_x	Random error effects
$[P_x P_y]_{corr}$	Correlated bias between random errors P_x and P_y
Po	Poiseuille Number

r	Result defined as the average differential pressure per unit length
R	Corrugation element radius
Re	Reynolds number
Re_{eff}	Effective Reynolds number adjusted for Poiseuille number correlation
Re_T	Transition Reynolds number
μ	Dynamic viscosity
w.r.t.	With respect to

Acknowledgement

I would like to extend my sincere thanks to the following people:

Matthew Rodney for his contribution to the experimental test setup, including 3D printing components and resin casting needle holders.

NASA LSP Fluid Team – Dr. Michael Harris, Michael Elmore, Dr. Jedediah Storey, Dr. Curtis Groves, Jacob Roth, Lennie Duncil, and Andrew Brown for consistent communication and collaboration.

Brandon Marsell, who originated the NASA LSP study series.

Dr. Paul Schallhorn for advice, motivation, and expertise in uncertainty analysis and developing the empirical Poiseuille correlation.

Dr. Daniel Kirk as a major advisor who facilitated many different research opportunities.

This work was completed as part of a NASA Launch Services Program (NASA LSP) awarded contract NNK14522002R to Special Aerospace Services (SAS), LLC of Boulder, CO who subcontracted to the Florida Institute of Technology.

Special thanks to NASA LSP and SAS for their contribution of additional data collected in their follow-on effort for Table 8 pg. 109, and for their assistance in getting the pipes cut as shown in Figure 4 pg. 15.

Dedication

To my wife, Laura. For your enthusiastic support in the numerous hours in revisions and devotion to the future generations through our wonderful children.

Chapter 1
Introduction

Flexible corrugated pipes are widely used in many engineering applications because they can accommodate bends, turns, and temperature changes while keeping strength and rigidity. There are a variety of internal geometries of the corrugated pipes namely axial, annular (circumferential/transverse), d-type, and helical. Figure 1 presents a schematic representation of the internal geometry of the assessed annular corrugated pipe. The internal geometry of the annular corrugated pipes is characterized by the inner diameter (ID), outer diameter (OD), corrugation height (E), corrugation pitch (P), and radius of each individual corrugation element (R).

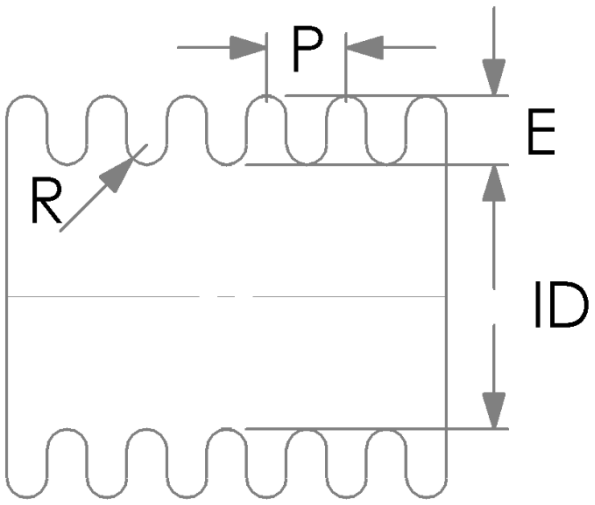

Figure 1 — Schematic of annular corrugated pipe geometry with corrugation element radius (R), corrugation pitch (P), corrugation height (E), and corrugation inner diameter (ID)

The motivation behind this study stemmed from a relevant application for corrugated pipes: the supply of purging gases to a rocket launch vehicle payload fairing prior to launch. These specific pipes can withstand high internal pressures and temperatures due to their braided stainless steel wrap reinforcement. The purging gases, typically air or nitrogen, are used to keep instrumentation clean and to manage environmental conditions – including flow rate, humidity, pressure, and temperature – inside of a launch vehicle payload fairing prior to launch. The diameters and lengths of the pipes vary based on mission-specific flow purging requirements, which are decided by the size and heat generation of the spacecraft instruments. A flow analysis must be conducted prior to each mission to properly determine the correct

flow rate range for an unknown and often varying purge system fluid resistance. A key element of a trustworthy flow analysis is the knowledge of the friction factor, or pressure drop, for a given pipe geometry and flow rate. The resulting correlation can be fed into NASA's GFSSP code [1] developed by NASA Marshall Space Flight Center.

Although corrugated pipes are used in many different engineering applications, the pressure drop and friction factor – as a function of pipe geometry and flow rate – are not readily available in literature. The standard Moody chart, which provides friction factor (f) versus the flow Reynolds number (based on hydraulic diameter) does not typically contain sand grain roughness dimensions (ε) that are as large as the corrugation element (E) . Further, the limited experimental measurements in literature show that the pressure drops are not in agreement with fully turbulent predictions or rough wall approximations. This holds true even if the notion of the sand grain roughness analogy is extrapolated to (E/ID) values that are consistent with typical corrugated pipes. Computational Fluid Dynamics (CFD) can be used to yield estimates on the pressure drop and resulting friction factor associated with the corrugated pipes, but these predictions would benefit from experimental benchmarking. All results presented in this study are assumed incompressible due to adiabatic, steady flow with low Mach number flow (M <

0.16). The analytical model for compressible adiabatic flow with friction loss, Fanno Flow, is theorized to recommend when determining pressure loss and energy balance for corrugated pipes.

The objective of this work was to experimentally quantify the pressure loss per length and friction factor coefficient of a series of relevant corrugated pipes commonly found in engineering applications, particularly for launch vehicle payload purging applications. The corrugated pipes used in this study had varying corrugation pitches, diameters, and flow rates.

A summary of the assorted sizes and important geometric parameters of corrugated pipe used in this study is provided in Table 1. For the pipes examined, the ratio of the corrugation height (E) to the inner diameter (ID) varied between $0.233 \leq (E/ID) \leq 0.333$ and the ratio of corrugation pitch (P) to the inner diameter (ID) of $0.181 \leq (P/ID) \leq 0.446$. For spacecraft fairing applications, the flow rates of interest are 0.25 to 94.4 standard liters per minute (slpm), which is equal to 0 to 200 standard cubic feet per hour (scfh), of nitrogen gas.

For each of the diameters shown in Table 1 and for the maximum flow rate, the Reynolds number based on the inner diameter and outer diameter is summarized. For example, the smallest diameter pipe has a Re_{ID} and Re_{OD} of 22,046 and 13,514, respectively, at 94.4 slpm of nitrogen. Conversely, the

largest diameter pipe has a Re_{ID} and Re_{OD} of 6,475 and 4,452, respectively, at 94.4 slpm of nitrogen. The Reynolds number based on the smaller inner diameter is higher than the Reynolds number based on the larger outer diameter. The reason for this is that although the diameter is smaller, the velocity must increase as the area is reduced to keep the same mass flow rate.

Table 1 — Geometry of tested annular corrugated pipes

Name Designation	Millimeters					Re_{ID}	Re_{OD}	Re_T[1]
	ID	OD	E	P	R	At 94.4 slpm		
Annuflex[2]								
6.35 (¼")	6.88	10.41	2.03	3.07	0.77	18,710	12,371	935
9.53 (3/8")	10.67	15.80	3.14	3.30	0.83	12,071	8,150	950
12.70 (½")	13.54	19.00	3.15	4.01	1.00	9,513	6,778	1,165
19.05 (¾")	19.88	28.93	4.94	5.72	1.43	6,475	4,452	1,149
Masterflex[2]								
6.35 (¼")	6.60	10.74	2.20	2.08	0.52	19,501	11,991	1,048
9.53 (3/8")	10.64	15.77	3.12	2.06	0.51	12,102	8,168	1,225
12.70 (½")	13.46	19.18	3.24	2.44	0.61	9,565	6,714	1,351
19.05 (¾")	19.63	29.18	5.07	4.47	1.12	6,559	4,414	1,312
Titeflex[3]								
6.35 (¼")	5.84	9.53	1.78	2.29	0.57	22,046	13,514	1,158
9.53 (3/8")	8.64	13.54	2.41	2.41	0.60	14,914	9,512	1,547

[1] Transitional Reynolds number from laminar

[2] ID provided by Manufacturer, measured, and derived remaining values.

[3] Not provided by the manufacturer. Measured and derived values in table.

Background and Literature Review

Current launch vehicle payload compartment analysis requires an estimated friction factor to approximate the pressure drop that occurs through the corrugated pipes. The low-pressure drop over small length, low speed, and consequently low Mach number corrugated pipe flow are assumed to be incompressible due to low density change. For incompressible flow, the Darcy-Weisbach equation and the widely referenced Moody Diagram [2] determine the friction factor in constant area pipes and ducts.

The Darcy-Weisbach equation (1), with a brief history given by Brown [3], is the accepted method for calculating energy loss in incompressible closed conduits where f is the friction factor, L is the length of pipe, D_h is the hydraulic pipe diameter, ρ is the density of the fluid, and V is the mean velocity of the flow. The friction factor is a measure of viscous loss for a flow in a pipe, and knowledge of the friction factor allows for estimation of the pressure drop per length associated with the pipe geometry and flow rate.

$$\Delta P = f \frac{L}{D_h} \frac{\rho V^2}{2} \tag{1}$$

$$Re = \frac{D_h V \rho}{\mu} \tag{2}$$

Reynolds number, Re (2), is used to describe the transition from laminar to turbulent flow where μ is the dynamic viscosity. For laminar flow in pipes with small Reynolds numbers less than 2,300, the Darcy friction factor, f, can be determined by the expression f = 64/Re.

The empirical relationship for turbulent flow in pipes (Re > 4,000) is calculated using the explicit Haaland [4] approximation to the Colebrook equation [5] given in (3) where ε is the absolute roughness. An ill-defined and ill-behaved region between those two limits is named the critical zone. Friction factor dependence on Reynolds number and the ratio of absolute roughness to the diameter was originally determined by Hunter Rouse, but Lewis Moody restructured the diagram to a convenient form for engineering use commonly called the Moody diagram. A detailed history, science, and technology of the Moody diagram is provided by LaViolette [6].

The last term is 6.9/Re which implies that as Re approaches infinity, this ratio goes to zero, thus the friction factor only becomes a function of the relative roughness (ε/D) and is defined as wholly turbulent where increasing the Reynolds number will not change the friction factor.

$$\frac{1}{\sqrt{f}} = -1.8\, log\left[\left(\frac{\varepsilon/D}{3.7}\right)^{1.11} + \frac{6.9}{Re}\right] \tag{3}$$

Yang [7] introduces drag reducing using polymer solutions for laminar to turbulent transition to reduce losses. Sletfjerding [8] and Afzal [9] provide friction factor values directly from transitional surface roughness. Willis[10] and Jimenez [11] provide comprehensive reviews with transitional flow and turbulent flow over rough walls. Newer numeric techniques, combined with increasing computing power, allowed for more numerical simulations to investigate roughness effects on turbulence. Per Jimenez, theoretical arguments are sound, but there is still a lack of conclusive experimental evidence.

With a base understanding of flow through smooth pipes, Chapter 2: Experimental Setup, in the Smooth Pipe Validation section, describes the initial validation testing to compare the new experimental setup with previous literature. The next section includes a literature review of various corrugated pipes.

Straight Corrugated Pipe Flow

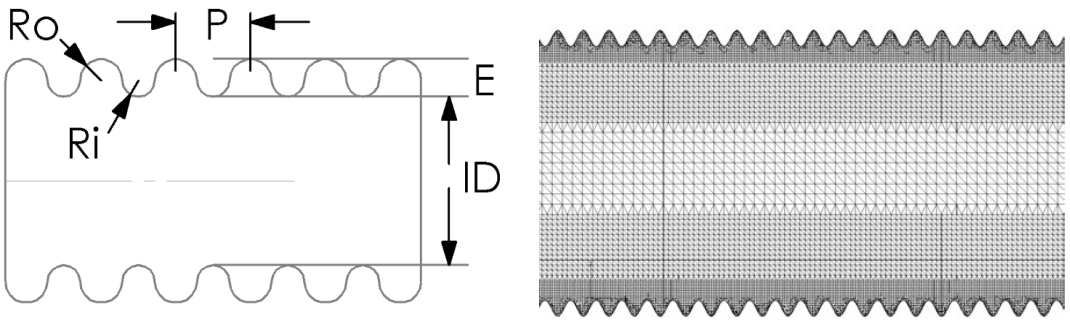

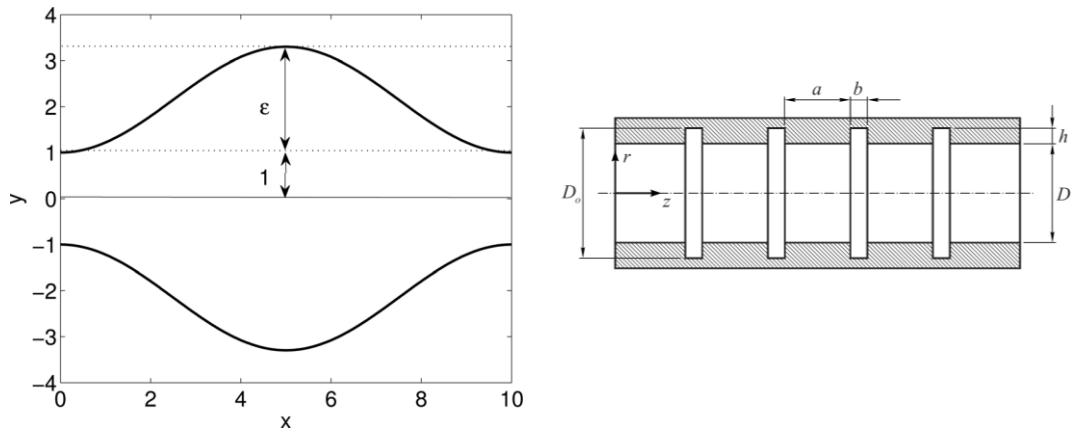

Figure 2 — Different types of corrugation S-type (upper left), triangular (upper right), sinusoidal (lower left), and square (lower right)

There are various geometric variations of annular corrugated pipes as shown in Figure 2. Esquivel [12] conducted a parametric study of laminar flow in sinusoidal pipes by varying the corrugation depth, corrugation pitch/frequency and corrugation expansion and contraction ratio. Some studies are conducted on 2D channel flow such as Sakar [13] and include calculations for heat transfer characteristics. Recent publications and applications include a variety of applications such as drainage ditch flows as in Calomino [14], which looks at water flow and free stream surface for corrugated pipes.

Table 2 categorizes different corrugation geometries and flow regimes while noting which papers are experimental, analytical, computational fluid dynamics, iteratively calculation methods, or a combination of experimental

and computational work for corrugated pipes. The references in bold are most identical to our experiment and compared against.

Table 2 — Summary of Literature Review

Corrugated Pipe Type		Laminar	Transitional	Turbulent
Annular	S-Type or Transverse	[This work]‡	[15]*, [19]*, [20]*, [22]*[4] , [This work]‡	[15]*, [22]*[4], [24]*, [25]*, [26]†
	Sinusoidal	[12]†, [13]†, [29]*, [30]†, [32]†, [33]**, [34]*, [35]**, **[38]***, [39]†, **[40]*, [42]***, [41]†, [45]**, [46]†, [47]†	[12]†, [13]†, [14]‡, [27]‡, [28]‡, [36]*, [37]* , **[38]***, [39]†, [40]*, [42]*, [46]† , [47] †	[26]†, [27]‡, [28]‡, [36]*
D-Type/Square			[48]‡, [49]†	[48]‡, [49]†, [50]*, [51]*, [52]†, [53]**, [61] †
Helical/Spiral		[57]‡, [58]**, [60]*	[15]*, [21]‡, [54]*, [55]*[5], [56]†, [59]*, [60]*, [64]*	[15]*, [21]‡, [54]*, [56]†
Teardrop				[65]*, [66]**‡
Sinusoidal Channel		[23]*, **[28]‡,** [44]‡	[23]*	[23]*

* Experimental data only

** Analytical

† Computational Fluid Dynamics only

‡ Experimental and Computational Fluid Dynamics

[4] Refers to 'helical' coil, but that is in a bent configuration, not axially helical

[5] Vertical

The first category, and the focus of this dissertation, is the transverse annular corrugated lines [See Figure 2-upper left]. The S-type category (different values for R_o and R_i) is bundled as concluded in Esquivel [12] when noting the minimal effect of expansion and contraction ratio for laminar flow. Figure 5 shows the characterization of annular corrugated pipes by plotting the relative corrugation depth to the minimum diameter (E/ID) vs corrugation pitch to the minimum diameter (P/ID). There are 4 different categories – slow variations, pocket corrugations, standard roughness approximations, and effectively finned pipes. Figure 3 shows four different annular corrugated pipes normalized to the inner diameter with different relative corrugation depth to the minimum diameter (E/ID) vs corrugation pitch to the minimum diameter (P/ID). The four different geometric categories are further described as slow variations, pocket corrugations, standard roughness approximations, and infeasible geometry. Slow variations appear when both E/ID and P/ID are large (i.e., Figure 3-red circles) and with low Re (Re < 10); the method of slow variations was studied Esquivel [12]. When both E/ID and P/ID become very small (<0.01, Figure 3-black diamonds), the pipes behave like traditional surface grain roughness approximation Moody. In between these two lies the presented annular corrugated lines. The final extreme categories (large E/ID

with small P/ID and small E/ID with large P/ID) are not feasible from a manufacturing perspective.

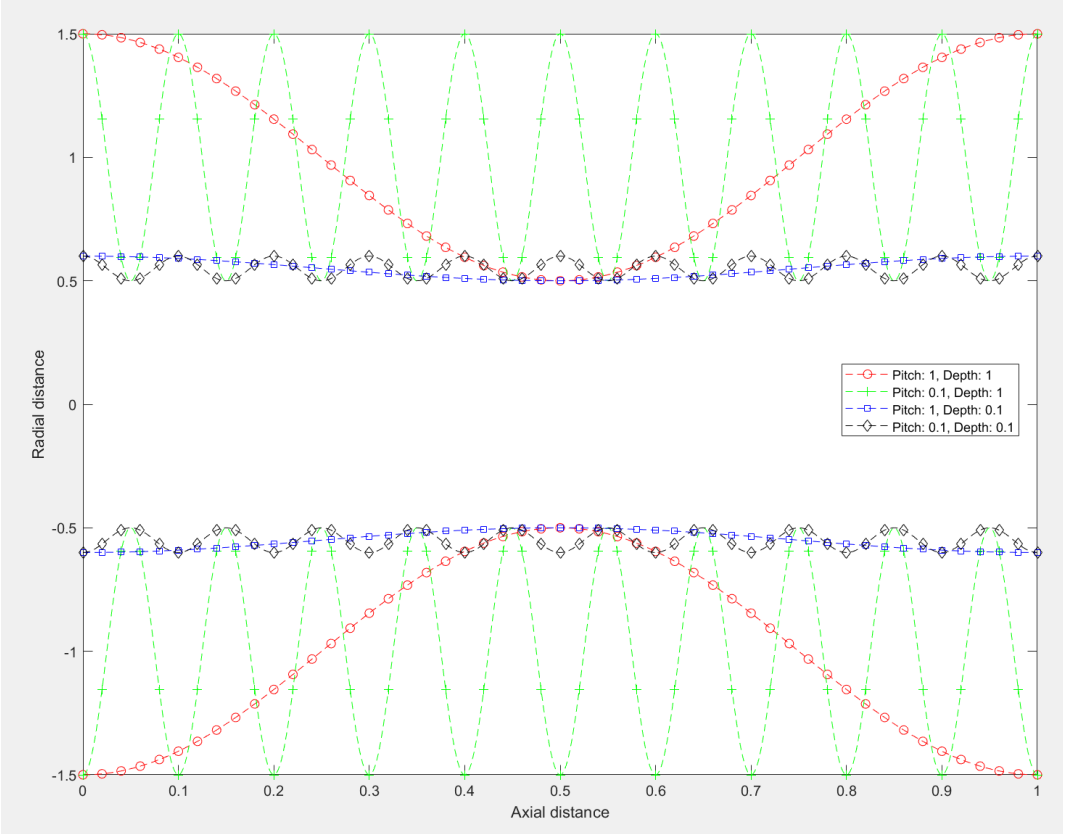

Figure 3 — Various ratios of pitch and depth to inner (minimum) diameter (normalized) ratios of corrugated pipes

Gibson [29] contains laminar water flow through corrugated pipes. The following papers compiled contain experimental data for transitional flow through corrugated pipes: Riley [15], Bernhard [19], Popiel [20], van der Linden [21], Ahn [22], Calomino [27], Shipton [36], Webster [37]. The following studied laminar flow in sinusoidal corrugated pipes: Lahbibi [32],

Esquivel [33], Inaba[34], Mahmud [41], and Chow [45] and for transitional flow Shipton [36] & Webster [37].

Corrugated Pipe Geometry Details

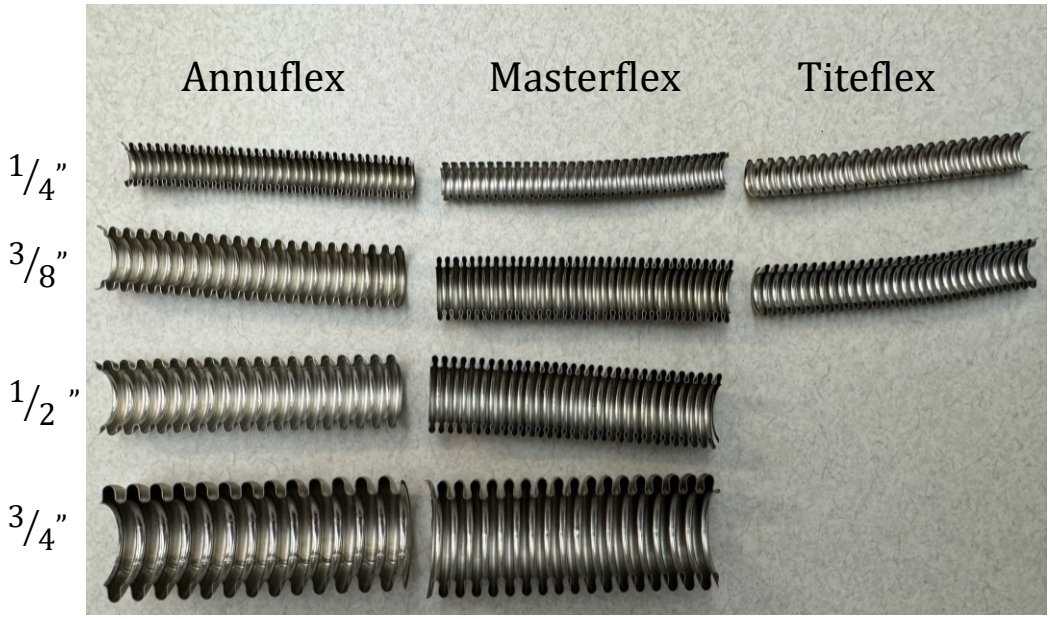

Figure 4 — Photo of tested corrugated pipes cross sectioned

Figure 4 provides a detailed look into the various geometric differences of the experimentally tested corrugated pipes. These cross-sections were provided through a follow-on study through NASA LSP and SAS Aerospace. The direct inner diameter measurements provided additional fidelity to the uncertainty analysis.

Figure 5 shows various combinations of P/ID with E/ID ratios normalized with the same minimum diameter for reference. These different non-dimensional parameters change the transitional Reynolds Number.

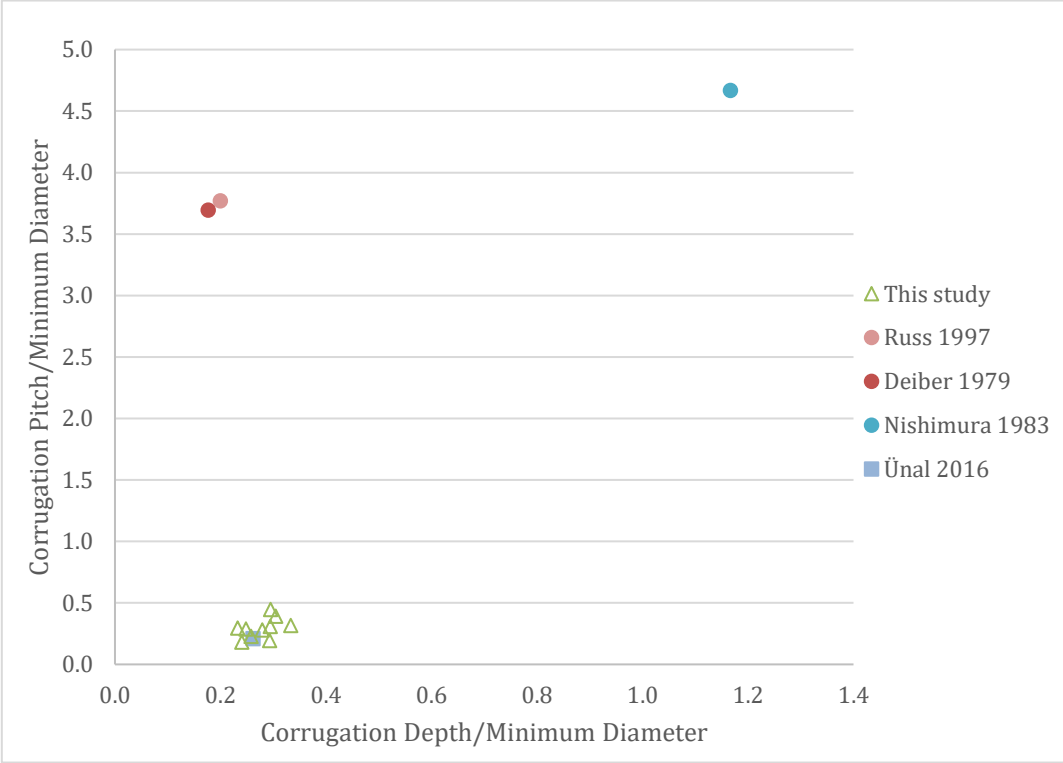

Figure 5 — Comparison of non-dimensional parameters for annular corrugated pipes (this study and references)

Table 3 shows a compilation of literature references for several different flow regimes: laminar, transitional, and turbulent flow in both S-Type and sinusoidal pipes. A sinusoidal axisymmetric profile is typically picked in analytical solutions because the expression for the radius is continuously differentiable. For Reynolds numbers less than 100, inertial effects are

negligible from Deiber [42] and a linear relationship should exist between f and Re^{-1}. For Reynolds numbers between 100 and 1,600, laminar flow is observed, but inertial effects in the corrugated pockets need to be considered compared to smooth pipe flow. For the corrugated pipes presented, the flow transitioned for Reynolds numbers between 1,400-1,600 and corresponds with Develi and Ahn [43]. As Reynolds number increases, the flow becomes fully turbulent.

Table 3 — Comparison of dimensionless parameters between current work and references

	Re_{ID}[6]	Friction $factor_{ID}$[7]	E/ID[8]	P/ID[9]
Deiber [42]				
	22-3,559	0.147-2.44	0.176	3.70
Russ [38]				
	370-15,780	0.089-0.221	0.200	3.77
Bian [40]				
	100-1,020	0.170-1.01	0.583	4.67
This study				
Annuflex 6.35 mm (¼")	117-18,710	0.078-0.422	0.295	0.446
Annuflex 9.53 mm ($^3/_8$")	75-12,071	0.078-0.566	0.294	0.309
Annuflex 12.70 mm (½")	59-9,513	0.067-0.733	0.233	0.296
Annuflex 19.05 mm (¾")	65-6,475	0.068-1.338	0.248	0.288
Masterflex 6.35 mm (¼")	122-19,501	0.075-0.439	0.333	0.315
Masterflex 9.53 mm ($^3/_8$")	91-12,102	0.064-0.557	0.293	0.194
Masterflex 12.70 mm (½")	60-9,565	0.053-0.850	0.241	0.181
Masterflex 19.05 mm (¾")	328-6,559	0.078-0.199	0.258	0.228
Titeflex 6.35 mm (¼")	138-22,046	0.052-0.316	0.305	0.392
Titeflex 9.53 mm ($^3/_8$")	93-14,914	0.048-0.580	0.279	0.279

With the definitions of common pipe flow regimes established, the question becomes what are the most important geometric factors that influence the flow through corrugated pipes? Even though there are multiple

[6] Reynolds Number calculated with inner diameter (ID)

[7] Darcy friction factor calculated with inner diameter (ID)

[8] Ratio of corrugation height (E) to inner diameter (ID)

[9] Ratio of corrugation pitch (S) to inner diameter (ID)

factors influencing the geometric properties of annular corrugated pipes, the most influential would be the definition of the hydraulic diameter being equivalent to the inner diameter. Esquivel [12] conducted a parametric study of the effects of the wall shape on laminar flow in corrugated pipes. As several authors have noted (Esquivel [12], Cotrell [35], Loh [47]), with incompressible flow, a lumped model can be used to describe the fully developed flow for any periodic section of pipe.

A third experimental investigation from van der Linden [21] compared basic CFD work to an experimental study for transitional flow through an annular corrugated geometry. He notes a periodic pressure variation in Figure 4 and shows the importance of where the static pressure is being measured. The fourth publication from Ahn [22] provided pressure drop in corrugated pipes for larger Reynolds numbers ($10{,}000 < Re < 60{,}000$) and determined that the flows were wholly turbulent. A unique result included a decreased friction factor with respect to increasing diameter. Ahn [22] states, "The reason for this contradiction remains to be explored." This study provides data $Re < 10{,}000$ which spans the range of laminar flow, critical zone, and transition flow, but not wholly turbulent flow.

Even though Ünal's [23] work on corrugated channels compared to pipe provides an insight into localized Reynolds number in the valleys. "When

the corrugation size d_2 (in Fig. 1) is used instead of the hydraulic diameter Dh, the Reynolds number corresponding to Re_{Dh} =1,500 is Re_{D2} = 300." The D2 designation is the diameter of the inner corrugation. Furthermore, Ünal notes, "for a circular cylinder, the range of 150<Re<300 represents the transition from laminar vortex street (known as periodic Karman vortices) to unsteady, turbulent vortex street while the boundary layer is laminar." The vortex shedding around the inner diameter can be observed in our results when the laminar flow deviates from the linear relationship of low-speed flows. The authors highly recommend viewing the digital videos taken during Ünal's experiments.

For laminar flow, the authors propose the minimum diameter as the hydraulic diameter of corrugated lines. Previous authors: Deiber [42], Bian [40], and Russ [38] compare geometrically (see Figure 6), but with results were presented with the mean diameter (D_{mean}) as hydraulic diameter. By shifting the hydraulic diameter definition from D_{mean} to the minimum diameter (ID), a more representative friction factor can be obtained and compared with smooth straight pipes. Translation of friction factor and Reynolds number calculations from the mean hydraulic diameter to the inner diameter for Bian, Deiber, and Russ are provided in the discussion section of Chapter 3 Experimental Results and results compared to this study in Figure 29.

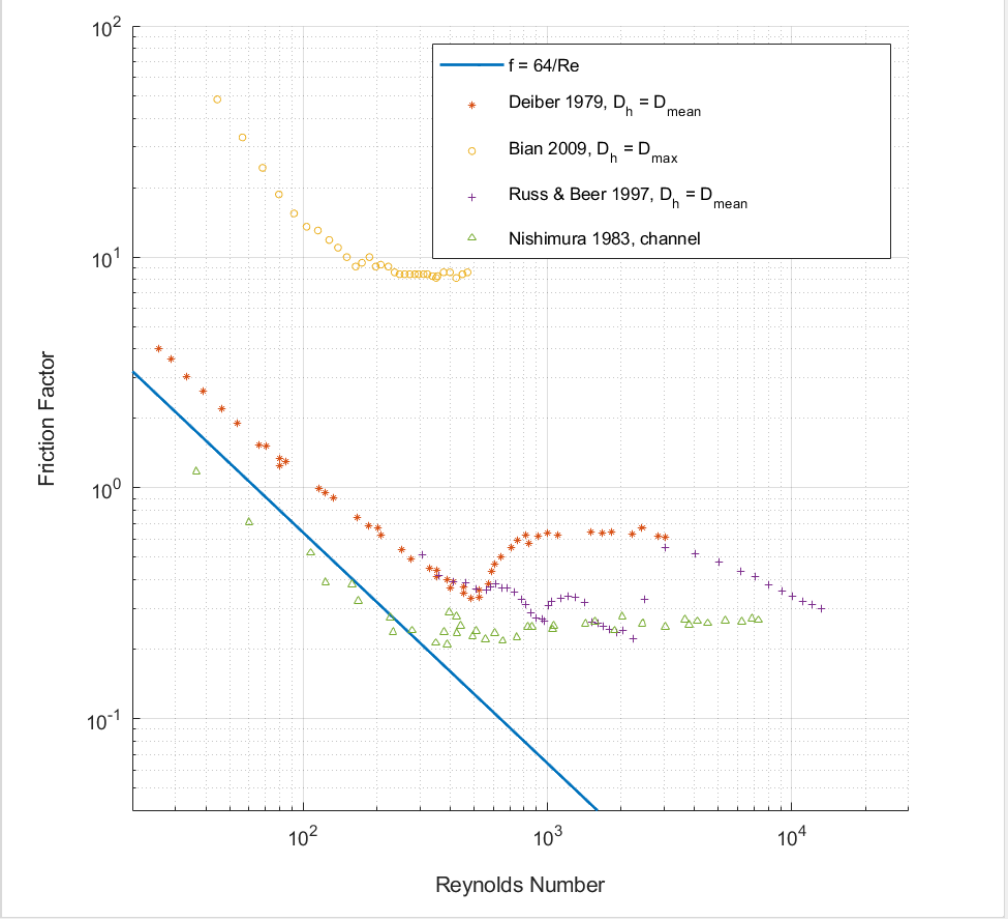

Figure 6 — As published references friction factor vs Reynolds Number annular corrugated pipes

Two-dimensional channel flow of a corrugation profile as in Nishimura [44] and Ünal [23] provides visual insight and direct velocity measurements as a reflection of circular corrugated pipes. The velocity profile varies in corrugated walls with the top of the flow being at a free stream compared to the pipes whose bulk central flow behaves like smooth pipe. Nishimura [44]

showed that two-dimensional laminar channel flow is periodic with vortices formed in the widening corrugation profile away from the center freestream. Ünal's [23] work is compared to Develi [43] who found a critical Reynolds number between 1,400 and 1,650, depending on the corrugation size, and that turbulent flow starts at the Reynolds number of 2,000 to 3,000.

The flow induced a high-frequency whistling with the smallest inner diameter corrugated pipes at the fastest flow rates, but minimal sound emanated from the straight pipes at the same flow rates. Several references studies the acoustical properties of flow through corrugated pipes including: Rudenko [89] ,Popescu [90], Ziada [91], Balaguru [92], Rajavel [93], Rudenko [94], Crawford [95], Cadwell [96], Golliard [97], and Tonon [98].

The third category of corrugated pipe is a square or rectangular periodic cavity along the axial direction of the pipe (See Figure 2-bottom right). Stel [48] & [49] noted a lower friction factor relative to an equivalent smooth line for Re = 5,000. Ohira [50] presents slush nitrogen flow for square corrugated pipes and compares experimental data with Daniels [24] and [25]. Djenidi [51] provides information on experimental laser-induced fluorescence and laser Doppler velocimetry measurements for the turbulent boundary layer over transverse square cavities. Vijiapurapu [52] contains LES simulation

results of turbulent flow in a square cavity pipe. Ismail [53] also describes the effects of a square corrugated pipe on the flow.

The fourth category of corrugated pipe is helical, spiral, or can be visualized as end over end like a gun barrel. From the most complicated and new geometries such as Kareem [57], while slightly increasing the friction factor 1.8-3.4, they can get 2.4-3.7 times the heat transfer through the new geometry. Wang [58] determined for laminar flow (low Reynolds numbers) that for a given pitch an optimal number of circumferential waves exist to minimize the resistance. Furthermore, with a fixed number of waves, there is an optimum pitch to maximize the axial rotation. Riley [15], van der Linden [21], Silberman [54], and Darzi [59] published various friction factor results for various geometries in the transitional flow regime. García [60] conducted experimental results with wire inserts and the corrugations slightly imposing the center flow (instead of expanding outwards). These results show a similar trend to the data collected. Pethkool et. al. [64] provides many geometric variations on the helical corrugated pipes to enhance heat transfer.

The final category of corrugated geometry is the teardrop shaped cross-section. The author does not see any benefit associated with creating a cavity for stagnant flow or vortex sheading trapping but referenced in early corrugated work as in Allen [65] and Hawthorne [66] with transitional flow.

After a review of literature associated with flow through straight corrugated pipes, Chapter 2 details the designed experimental setup. Chapter 3: Experimental Results covers the experimental results collected and the comparison to selected literature references. The next section introduces Chapter 4 Computational Fluid Dynamics.

Computational Fluid Dynamics (CFD)

With the recent invention of computers, computational fluid dynamics (CFD) has allowed research to give a different simulated perspective on the characteristics of fluid flow. Jaiman [26] conducted CFD modeling for a sinusoidal transverse corrugation with a low ratio of corrugation pitch to inner diameter. References with sinusoidal CFD work included: Saha [46] conducted DNS low-Re transition regime; Kim [39] references Russ [38] which is one of the references for comparison; Loh [47], whose work follows that of Cotrell [35] also focuses on CFD work for critical Reynolds numbers. Lahbabi [32] contains computational methods for laminar flow in corrugated pipes and is compared to Deiber [42].

Further studies have been conducted on various types of corrugated pipes: Jotkar [30] studied sinusoidal variation of a channel for very low Reynolds numbers. Konda [31] reviewed bubble motion through a sinusoidal

channel. Calomino [27] conducted experimental and numerical analysis of a sinusoidal profile lined corrugated pipe with free surface flow in a civil engineering drain application. Other studies including Stel [48] study d-type or square corrugations. Stel et. al. [49], Vijiapurapu [52] and Ismail [53] provide numerical simulation for d-type corrugated pipes. Azevedo et. al. [61] provides numerical simulation for d-type corrugated pipes of $10{,}000 < Re < 50{,}000$.

Pisarenco [56] provides turbulence modeling for helical transverse pipes. Reynolds numbers between $10{,}000 < Re < 50 \times 10^6$ were analyzed. The authors want to note the same trend of increasing and plateauing friction factor with increasing Reynolds numbers ($Re > 10^5$) observed to be wholly turbulent at these Reynolds numbers. A high-frequency whistling noise was observed during the data collection. Popescu et. al. [90] provides analysis of the acoustical noise for under-ocean corrugated pipes. Further studies have been conducted on diverse types of corrugated pipes.

Chapter 2 describes the experimental apparatus, data recording, and validation using smooth pipe flow. Chapter 3 contains the results of the corrugated pipes in a straight configuration. Chapter 4 covers the current CFD analysis using a commercial code STAR-CCM+ with various turbulent models; shows the computational fluid dynamics work to compare various smooth lines and which turbulence model matches the experimental data the best

using commercially available software. Finally, in Chapter 5, the lessons learned, conclusions, and future work are presented.

Chapter 2
Experimental Setup

Using theory from smooth internal wall and fully rough internal wall pipes – in laminar and turbulent flow Reynolds number regimes – an experimental set-up was specifically designed to determine the friction factors associated with the corrugated pipes, previously shown in Table 3. Figure 7 shows a schematic of the experimental setup used to measure fluid differential static pressure at evenly spaced intervals of 0.305 m (1 ft.) along a 3.05 m (10 ft.) length of corrugated pipe. The figure shows the relationship between the important components, including the pressure regulator, relief valves, flow controllers, diffuser section, pressure transducers, data acquisition devices, and computer for data recording. Selvam [10] emphasizes the necessity of using additional pipe for entrance and exit sections for developing flows. Therefore, to ensure that the flow was fully developed and free of entrance or exit effects, 0.61 m (2 ft.) corrugated extension segments were attached to the entrance and exit of the primary test section pipe with threaded fittings. The fittings were assumed to introduce negligible error but were included as physical deliverables and the length was approximated using Joshi [63]. The

nitrogen flow rate was controlled by two Alicat mass flow controllers, MC 20, and MC 100, providing 20 and 100 standard liters/minute, respectively.

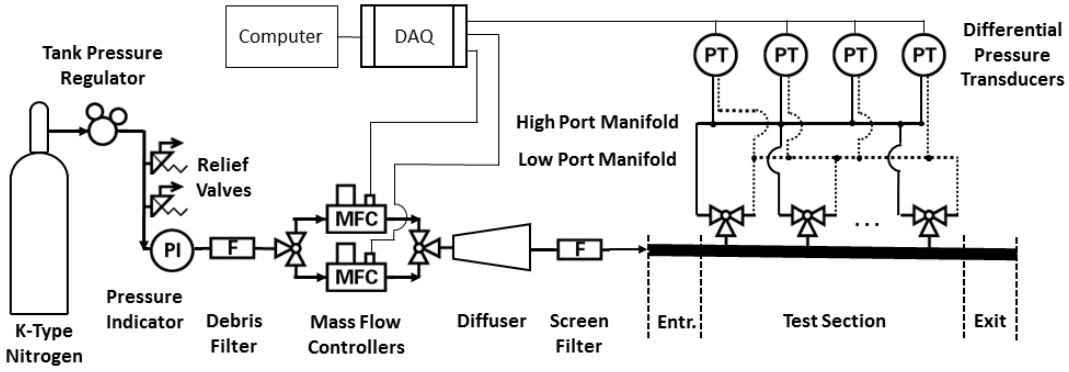

Figure 7 — Schematic diagram of experimental setup including pressurized nitrogen source, tank regulator, mass flow controllers, diffuser with screen filter connected to an entrance, test and exit section of corrugated pipe

Based on lessons learned during initial testing and data collection, changes were made to the experimental setup. Figure 8 shows photos of the completed assembly for the beginning of the second phase of data collection. The red arrows show the locations of the static pressure taps where the needles were located. The green arrows show where those static pressure taps are connected via polypropylene tubes to a pressure port manifold (later automated as shown in Figure 36 on pg. 115) to route the static pressure port directly to the high and low pressure sense ports of the differential pressure transducers. All the mass flow rate control and DAQ monitoring equipment are housed in the blue colored boxes and arrows (see Figure 31). The source

nitrogen flows through the selected mass flow controller (see Figure 9-left and Figure 10) and through a diffuser (see Figure 11).

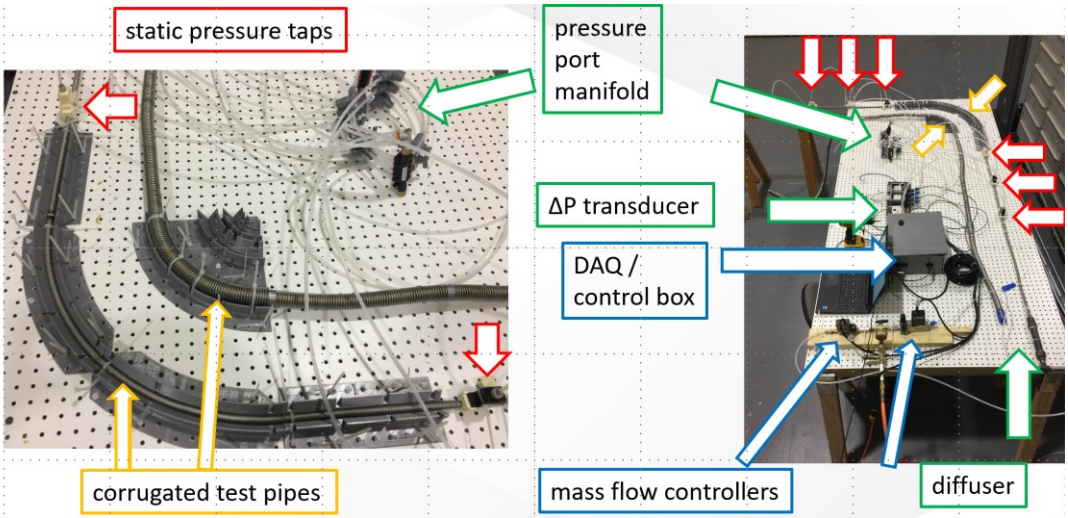

Figure 8 — Pictures of Experimental Assembly, left – corrugated pipes, static pressure ports and Phase I pressure port manifold, right – overall test setup

Figure 9 — Alicat mass flow controller (left) and Omega differential pressure transducer (right)

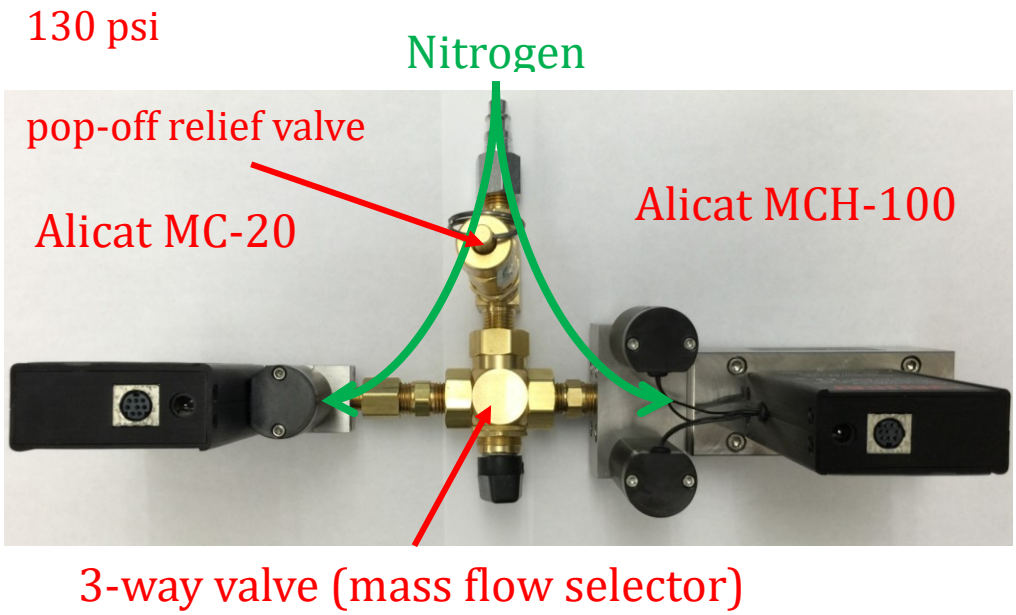

Figure 10 — Mass flow controller selector subassembly

To ensure that the pressure transducers and mass flow controllers were all of the sufficient sensitivity to measure with acceptable accuracy, the pressure differential between the gauges and a component selection study was performed. Two mass flow controllers were selected to minimize the error over the range of set points. Figure 41 pg. 127 in Appendix A – Experimental Setup shows the percent error readings for the mass flow controllers. Figure 39 on pg. 123 in Appendix A – Experimental Setup shows the percent error readings for the differential pressure transducers using an estimated differential pressure reading. The original set of four differential pressure transducers was inadequate for the smallest diameter pipes due to larger

measurements than predicted and a fifth differential pressure transducer was incorporated to complete the data collection. Table 11 pg. 119 summarizes the differential pressure transducers for this paper. A comprehensive uncertainty analysis was conducted and included in Appendix B – Uncertainty Analysis.

A diffuser section (see Figure 11) between the mass flow controllers and test section ensured uniform flow from a smaller diameter supply source to a larger diameter corrugated pipe test section. The diffuser contained a brass muffler allowing diffusion of the nitrogen stream through a plenum chamber. A wire mesh screen was installed at the end of the chamber, like mesh screens in the entrance section of wind tunnels, to help provide uniform flow. After the screen, the entrance length of the corrugated pipe was connected, then to the test section, and finally to an exit length before venting into the atmosphere.

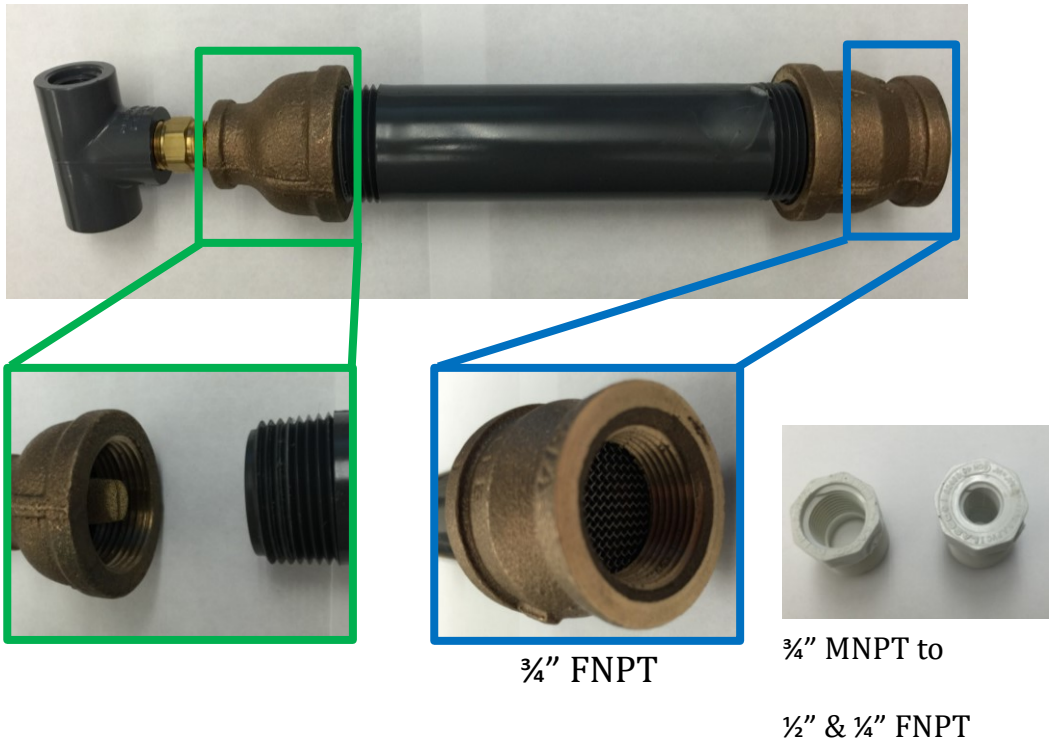

Figure 11 — Plenum chamber in between mass flow controllers and corrugated line entrance section

Typical static pressure ports for flow through pipes comprise of a smooth edge connection located on the outer surface or radially internal to the flow in a pitot static configuration. Given the unique configuration of the corrugated pipe geometry, static ports located on the outer diameter of the corrugated pipes could experience dynamic pressure as flow expands radially outward, which produces a pressure gradient along the wall of the tube (see [21 – Figure 4). Pitot static tubes required 15-20 times the diameter of the

pitot tube to be engaged in the upstream flow. While properly designed static pitot tubes provide a high degree of accuracy, even when angular misalignment occurs Mitchell [81], it was infeasible to install pitot static tubes with the small diameter pipes tested. A 22-gauge stainless steel needle 0.4064 mm ID, 0.7112 mm OD (0.016" ID, 0.028" OD) provided a small flow interference and the tip was adjusted to the *center stream pipe* for the static pressure measurement (see Figure 12). A 6.35 mm (¼" NPT) hub provided a connection to the pressure manifold. The needles were held in place using custom-made 3D printed holders, which matched the pipe's outer geometry. Each holder compensated for the depth of the needle into the freestream to ensure that the needle ended in the center of the corrugated pipe.

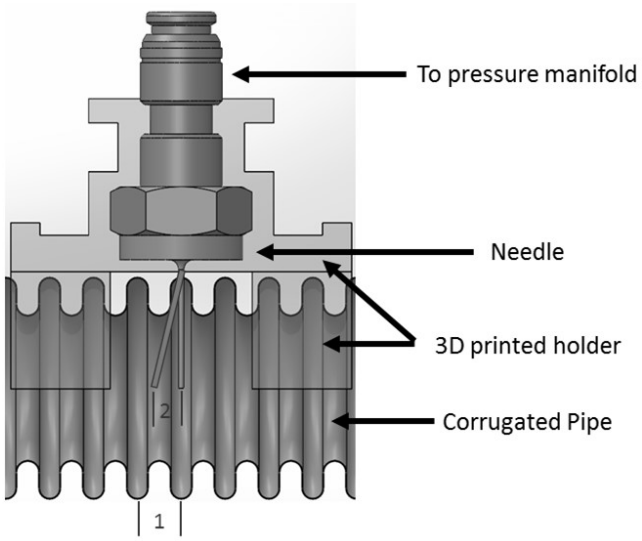

Figure 12 — Cross sectional CAD for the static pressure port holder with exaggerated outline of the needle in a bent configuration

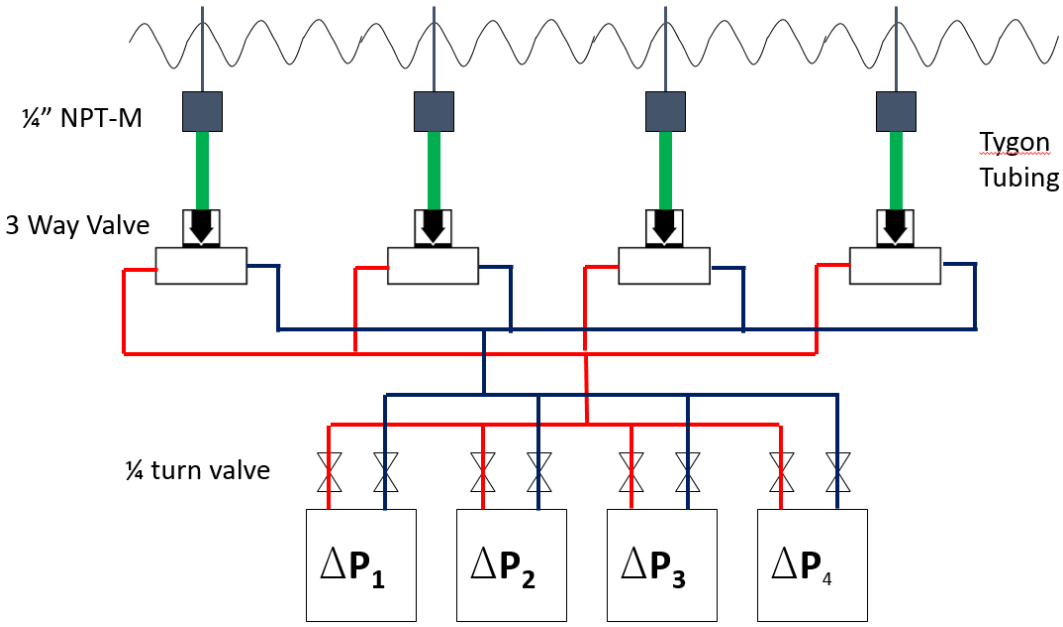

Figure 13 — Schematic representation of pressure ports and manifold routing to the differential pressure transducers in parallel

The distance between pressure port locations was nominally 304.8 mm (12 inches) and varied between each pipe due to the different corrugation frequencies or pitch. Each needle hole is located on the top outer peek of a corrugated segment with the distances between the pressure ports measured and given in Table 9 on pg. 111. 3D printed parts (See Figure 14) provided an accurate template for center punching, drilling holes, and holding the needles into place. After installation, the needles were sealed to the pipe using silicone and leak checked by pressure testing to 55.2 kPa (8 psi). The low pressure did not provide a visible extension or flexing of the fixed pipe apparatus. The

pressure taps were directed by three-way valves to two different manifolds, as shown in Figure 13, one designated as the high-pressure side (upstream) and one low side (downstream). Examples of static pressure routing are located in Appendix A – Experimental Setup, see Figure 34 on pg. 113 and Figure 35 on pg. 114. These high and low side manifolds were connected in parallel to the Omega differential pressure transducers (summarized in Table 11 on pg. 119) and simultaneously measured to ensure the most accurate range for the measurement. The burst pressure limit for the pressure transducers was 68.9 kPa (10 psi), which is 15% greater than the largest differential pressure recorded 58.6 kPa (8.5 psi).

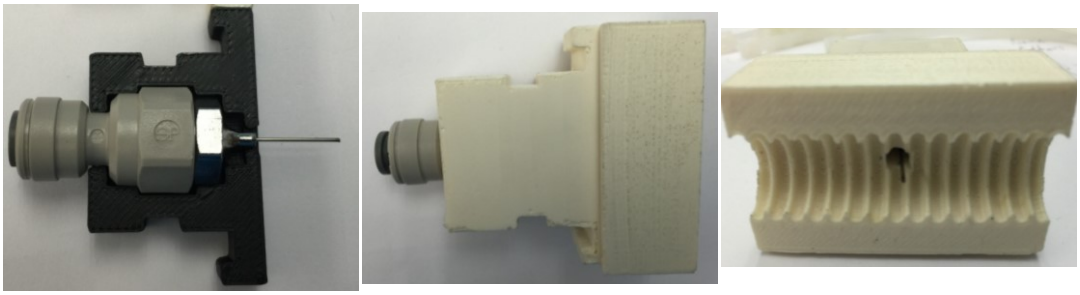

Figure 14 — Needle Holder Design cross section (left), assembled (middle) and bottom (right)

Data Recording

Based on previous work discussed earlier, it is likely that the flow through the corrugated pipes never establishes a steady state, but rather that

there are continuous, unsteady, and periodic effects associated with the flow over the corrugation elements. For example, as with a backward-facing step, there is a continuous creation and shedding of vortices from the discrete geometric element. However, the purpose of this work is to determine an average friction factor that can be used for engineering applications, and a suitable time averaging of the pressure measurements was performed. Similar techniques are used to determine the time-averages flow parameters downstream of a backward-facing step [82], [83], [84] &[85]. To determine a suitable data collection window, collected pressure data averaging was performed over a series of data sample sizes. Once the average value of the pressure data no longer changed with time, the unsteady and periodic effects were considered suitably averaged, and a 30-second data collection window was used on each test. The mass flow controller data (volumetric flow rate (liters/min), mass flow rate (standard liters per minute), outlet temperature (°C) and outlet pressure (psia)) was collected at 10 Hz while the pressure transducers (in. H_2O) were sampled at 10 Hz. The unsteady flow effects are averaged for each single data sample. All control and monitoring of the experimental apparatus was implemented via National Instrument's LabVIEW program with the front-end shown in Figure 15.

Figure 15 — LabVIEW screen shot of control panel with mass flow controller set point

Data Calculations

To obtain independent sets of differential pressure readings for a set flow rate and port configuration, required the following data reduction steps:

1. Use the ‘zero’ flow measurement to re-zero all pressure transducer voltage readings.
2. Truncate transient measurements between set point flow rates
3. Separate data per flow rate

Since all 4 pressure transducers were measured simultaneously, post processing calculations determined which pressure transducer was most accurate in range for a given flow rate.

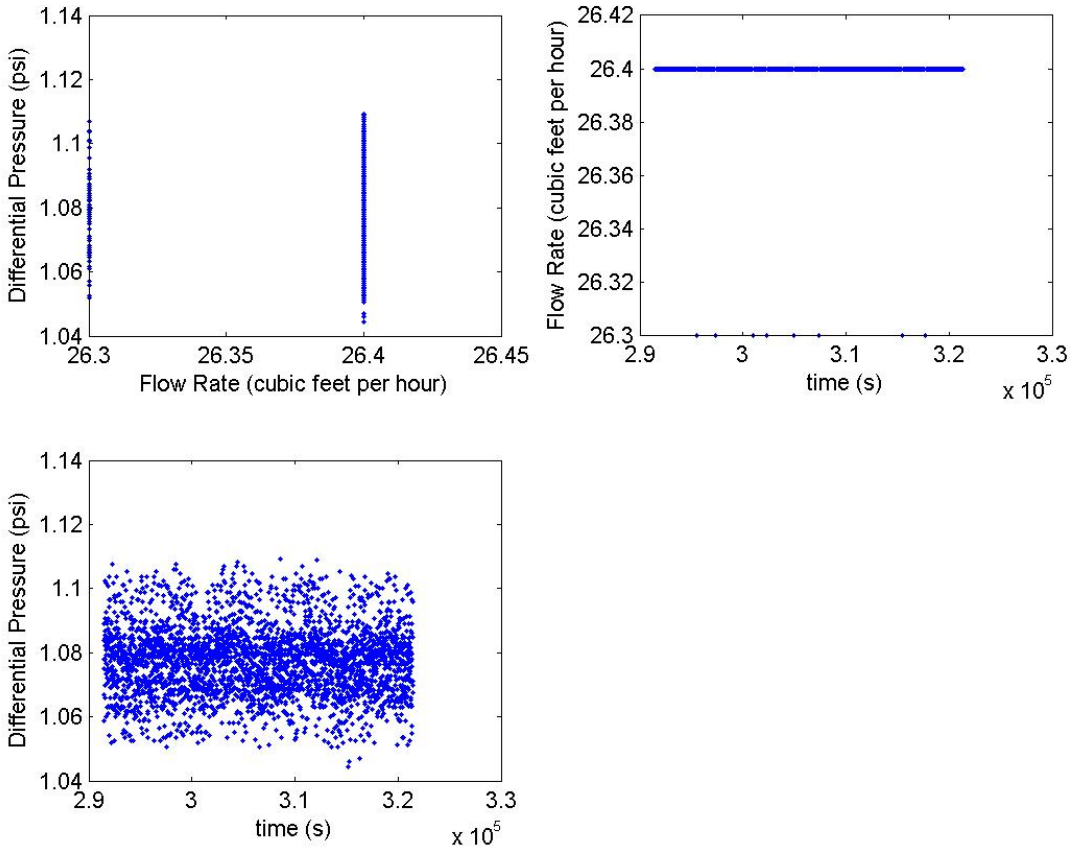

Figure 16 — Sample Data Line #17 at 70 scfh plot of differential pressure vs flow rate (upper left), flow rate vs time (upper right), differential pressure vs time (lower left) (step 4)

The uncertainty of the individual measurements is described in Appendix A – Experimental Setup (see Figure 37 on pg. 121, Figure 38 on pg. 122 and Figure 39 on pg. 123).

From the design of the experimental apparatus, all the controlled mass flow rates will remain constant throughout the corrugated pipe, as long as there are no leaks. The continuity equation (4) describes the relationship between mass flow rate, density, and velocity of the fluid flow, and the cross-sectional area where the flow occurs. Continuity remains true in turbulence flow representing a time-averaged mass value. The governing dimensionless parameters of friction factor and Reynolds number equations can be rewritten in terms of mass flow rate and controlled by the mass flow controller. By controlling the mass flow rate, the various geometries tested at different times and input conditions will be set and controlled to a mass flow rate – which will reduce the uncertainty of the overall experiment and provide consistent set points. Rewriting friction factor, equation (1) in terms of mass flow rate will yield equation (5). Reynolds number, equation (2), rewritten in terms of mass flow rate will yield equation (6).

$$\dot{m} = \rho V A \tag{4}$$

$$f = \left(\frac{\Delta P}{L}\right)_{Avg} \frac{2D_h}{\rho V^2} = \left(\frac{\Delta P}{L}\right)_{Avg} \frac{\rho \pi^2 D^5}{8\dot{m}^2} \quad (5)$$

$$Re = \frac{\rho V D}{\mu} = \frac{4\dot{m}}{\pi D \mu} \quad (6)$$

The uncertainty associated with the data reduction equations (5) and (6) are described in Appendix B – Uncertainty Analysis (see Figure 44 and Figure 45).

With the data recording and reduction described, the experimental setup validation process is described below. The validation of the experimental apparatus compares previous analytical and experimental results using a smooth pipe.

Smooth Pipe Validation

Electrical metal tubing (EMT) was used as a test flow pipe to validate the experimental apparatus by taking differential pressure loss measurements at various flow rates to compare smooth line Reynolds number and friction factor predictions. The importance of validating a new experimental apparatus is self-explanatory, but some of the detailed issues in validating fluids experiments are described in Roache [86]. EMT provided the rigidity, smoothness, and straightness for a test flow pipe, and a 15.875 mm ID and 20.955 mm ID (0.625” ID and 0.825” ID) pipe were used. To ensure a fully

developed flow free from entrance or exit effects, a 1.524 m (5 feet) long segment was attached to both ends of the 3.048 m (10 feet) test section. Figure 17 shows the measurement of differential pressure per unit length (Pa/m) vs set point standard volume flow rates (standard liters per minute). Theoretical laminar and turbulent pipes were recreated from the Haaland approximation of (3) for smooth wall pipes and extended into the transitional region. The error bounds calculations are detailed in the uncertainty analysis using Coleman and Steel [88] in Appendix B – Uncertainty Analysis. Results for the 0.825" EMT smooth pipe were similar to the 0.625".

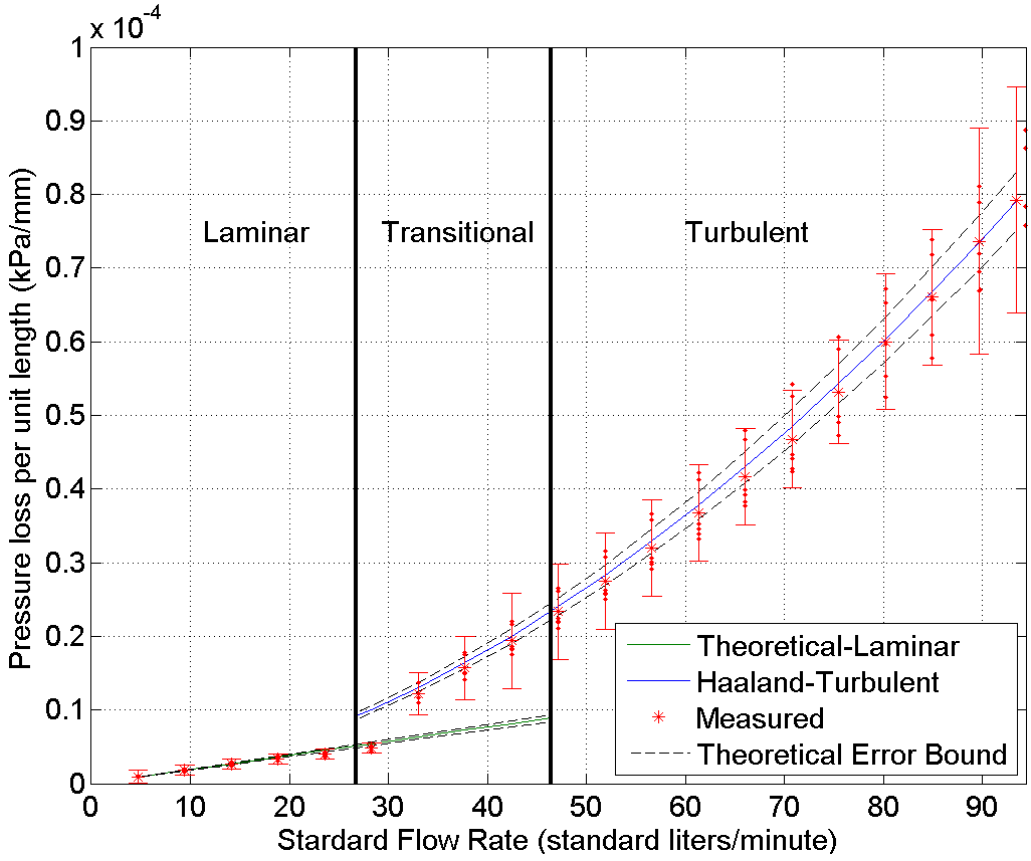

Figure 17 — Differential pressure per length and mass flow rate for smooth 0.625" EMT pipe

Figure 18 shows the calculated friction factor vs Reynolds number for the smooth pipes. Both smooth walled pipes show a high degree of agreement between established correlations and the experimentally measured data for friction factor vs Reynolds number. Both pipes start to deviate from the

laminar flow at approximately Re ~= 1,500, potentially due to internal disturbances including the fittings or the pressure tap needles within the flow.

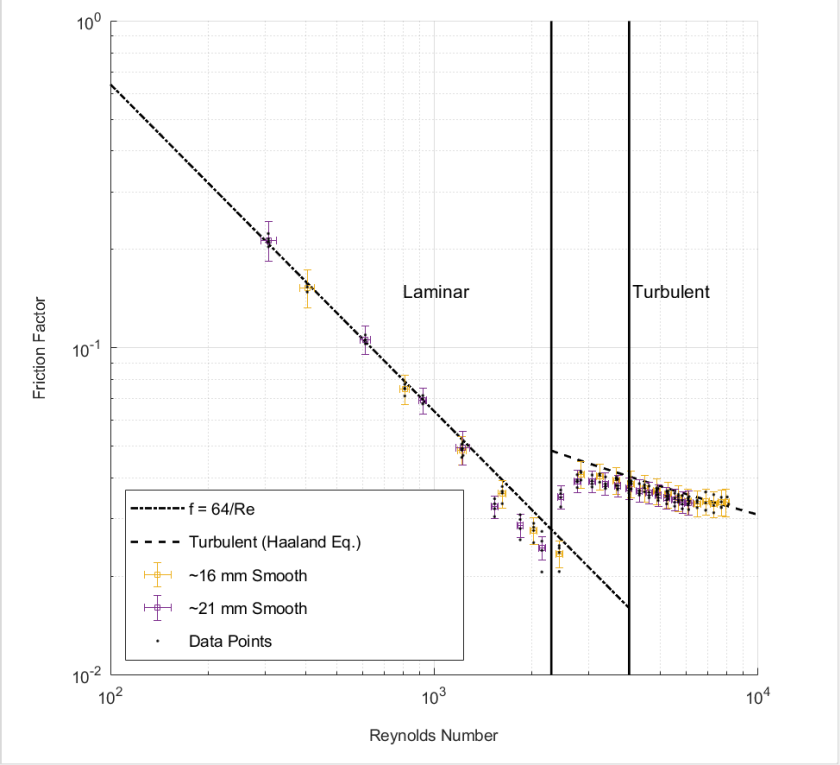

Figure 18 — Calculated friction factor vs Reynolds number for EMT pipe to validate experimental testing apparatus

Smooth Pipe Lesson Learned

Flexible polypropylene tubing does not maintain a uniform diameter and is practically impossible to keep straight as it usually arrives coiled.

With the experimental apparatus validated with smooth lines, the next chapter details the separate phases of data collection with corresponding results from the corrugated pipes in a straight configuration.

Chapter 3
Experimental Results

For each of the varying flow rate set flow rate points, the differential pressure was collected for each combination of pressure port locations. Three phases of data were collected with lessons learned being rolled into subsequent phases of data collection, as outlined in Table 4. All phases used gaseous nitrogen and mass flow readings, which were collected and controlled at 10 Hz.

Table 4 — Experimental Test Matrix Overview

Phase	Set mass flow rate Interval (scfh)	ΔP port locations	Steady state hold time (seconds)	Pressure transducer sampling (Hz)
Phase I (Straight)	Zero by 10 to 200	P1-P2, P1-P3, P1-P4, P1-P5, P1-P6, P1-P7, P1-P8, P1-P9, P1-P10	30	100
Phase 2 (Redo Phase I and 2D bends)	Zero by 10 to 200	Six locations (9 combinations): P1-P7, P1-P8, P1-P9, P2-P7, P2-P8, P2-P9, P3-P7, P3-P8, P3-P9	3	10
Phase III	Zero by 0.25 to 40			

Phase I

The first set of data collection included measuring the differential pressure between ports: 1-2, 1-3, 1-4, 1-5, 1-6, 1-7, 1-8, 1-9, 1-10 with a set standard flow rate of 0 to 200 scfh in ten scfh increments. These initial results showed a larger error when smaller distances were measured, but more importantly, it showed that all measurements were taken with respect to the first needle. Any error introduced by the first needle would be undetectable in the data set since it is common to all measurements.

If a needle was bent in the upstream direction, the measurement would not only be reading the static pressure but also a component of the dynamic pressure (installation bias error). See Figure 12 for an exaggerated bent needle. On the opposing effect, if the needle is bent toward the downstream direction of flow the localized flow near the needle would cause a decrease or negative pressure – similar to a venturi siphon. Initially, the needles were cut to the length which the needle was in the center stream of the corrugation to reduce any of these effects. In the early stages, the ends of the needles were not carefully taken into consideration, amplifying the error induced by the needle installation. Observations of independent needle installation error became apparent as shown in the resulting differential pressure per unit length and friction factor vs Reynolds number, shown in Figure 19.

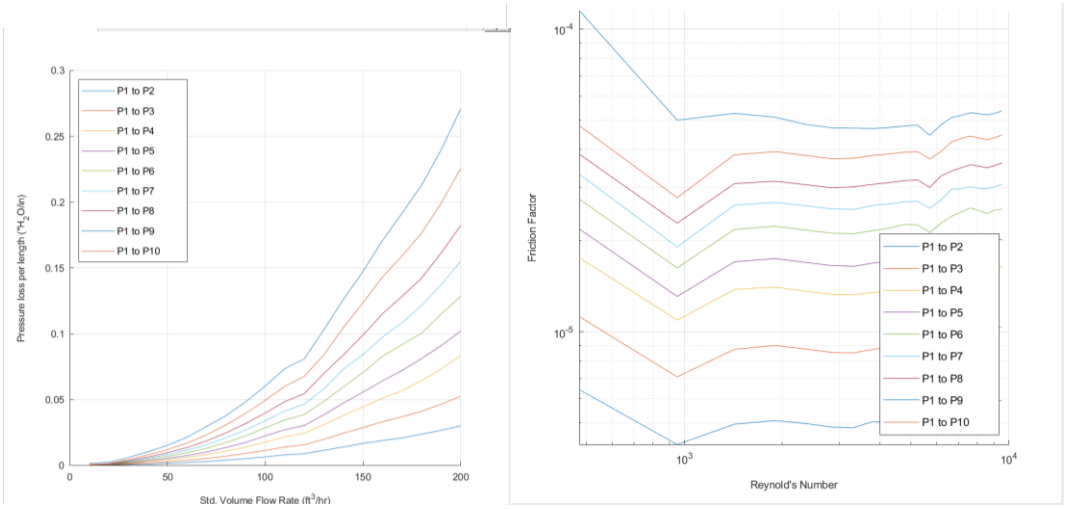

Figure 19 — Initial results of differential pressure per unit length for various distances in corrugated pipe (0.50" Annuflex)

The expectation was to have differential pressure per length provide consistent, repeatable results over varying lengths. This was based on the lower flow rates for short pipe lengths, which do not cause any compressible effects. These Phase I results were not included in any subsequent analysis/conclusions due to the major source of the error – the needle installation effects, which were replaced and fixed.

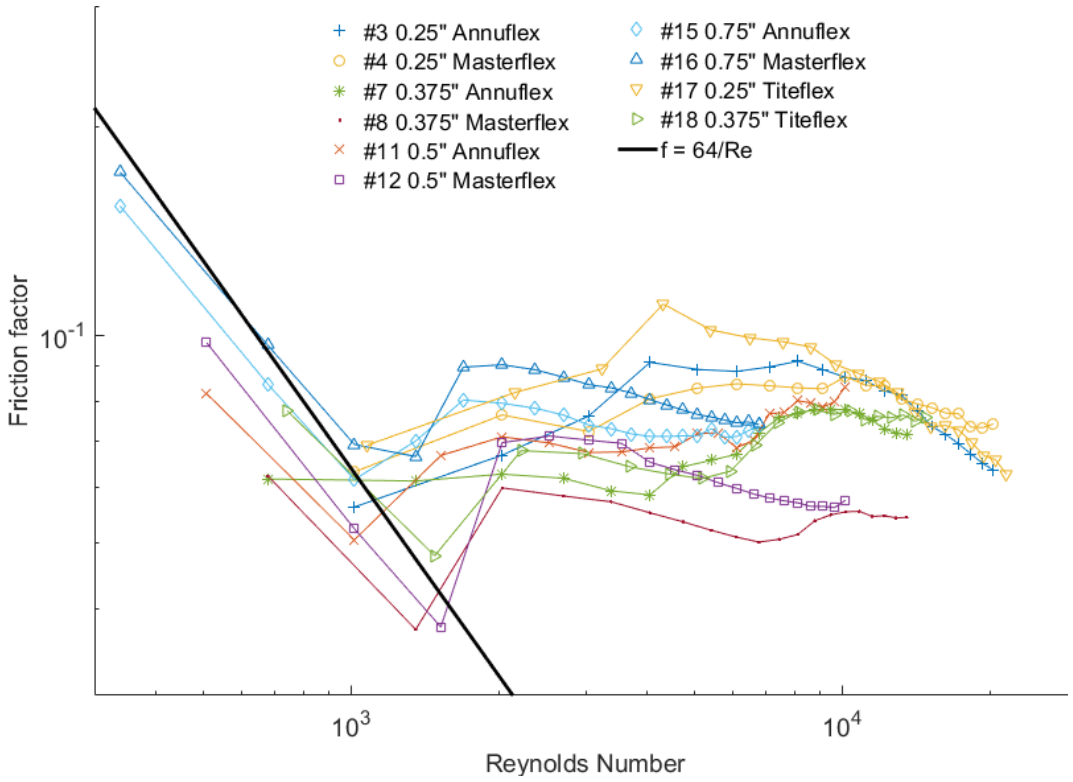

Figure 20 — Phase I results of friction factor vs Reynolds number for tested corrugated pipes

Figure 20 shows the resulting friction factor vs Reynolds number for the tested corrugated pipes for the initial Phase I.

Phase I Lessons Learned

1. The Alicat mass flow controller stated a standard *mass* flow rate of 40 standard liters per minute. While the units did not initially make sense to state a mass flow rate with units of volume flow, one can convert between the two by dividing or multiplying by the density at the

standard conditions. This led to a separate sanity check with creating a choked flow condition in an orifice to gain confidence and understanding of the output units of the mass flow controllers.

2. Pay attention to the transducer response times – oversampling adds unnecessary post processing time (i.e. the differential pressure transducers have a response time of 500 milliseconds – the Phase I sampling of the analog signal at 3,000 Hz was heavily oversampled).
3. One major observation is the "whistling" effect caused by the turbulent flow through the corrugated pipes. The experiments required double hearing protection per OSHA, for the maximum 120 dB acoustic whistling. The audio signals were captured and the oscillation shedding frequency for each geometry at each flow rate can be determined with a fast Fourier transform and remains future work.

Phase II

After the initial set of data was collected, the data collection scheme was modified to record each pipe summarized in Table 4 by measuring the pressure differential between all combinations of ports: 1, 2, 3, 8, 9, 10. The middle pressure ports were not installed and sealed. The resulting static pressure ports were: 1-8, 1-9, 1-10, 2-8, 2-9, 2-10, 3-8, 3-9, and 3-10 for

nitrogen flow rates between 0-94.4 slpm (0-200 standard cubic feet per hour scfh) in increments of 4.72 slpm (10 scfh). This allowed error tolerance and detectability; when there was a needle bent, the average differential pressure per length values would be skewed high or low, and the data for the needle could be removed.

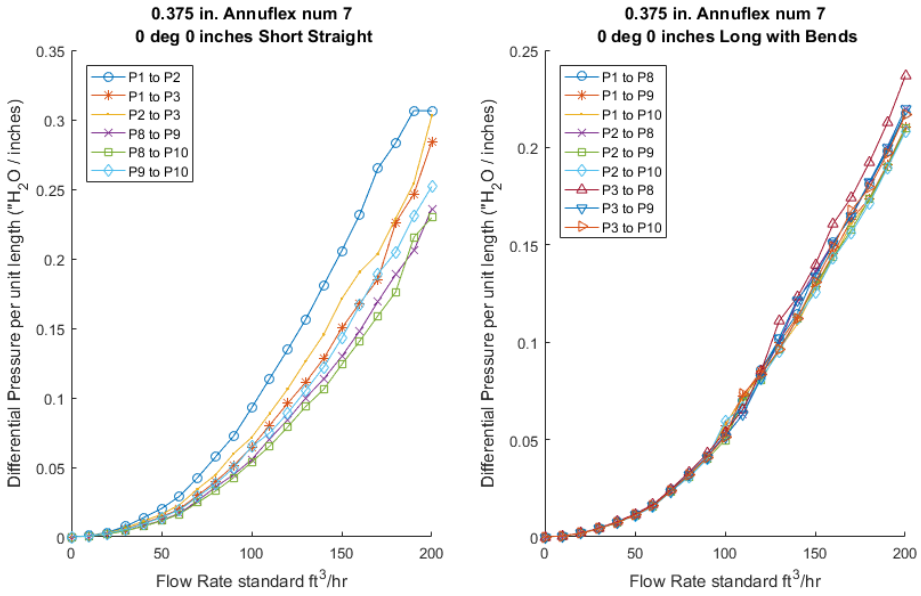

Figure 21 — 3/8" Annuflex - Standard volume flow rate (scfh) vs differential pressure per length ("H_2O/inches)

Figure 21 shows the resulting pressure loss per length at the set flow rates for the 3/8" Annuflex pipe. The left plot shows the variation associated with the smaller distances between differential pressure sensors (due to smaller pressure loss being measured) and the right plot shows the

consistency of averaging multiple combinations of pressure drop locations over longer distances. The combination of the longer lengths was used in the analysis.

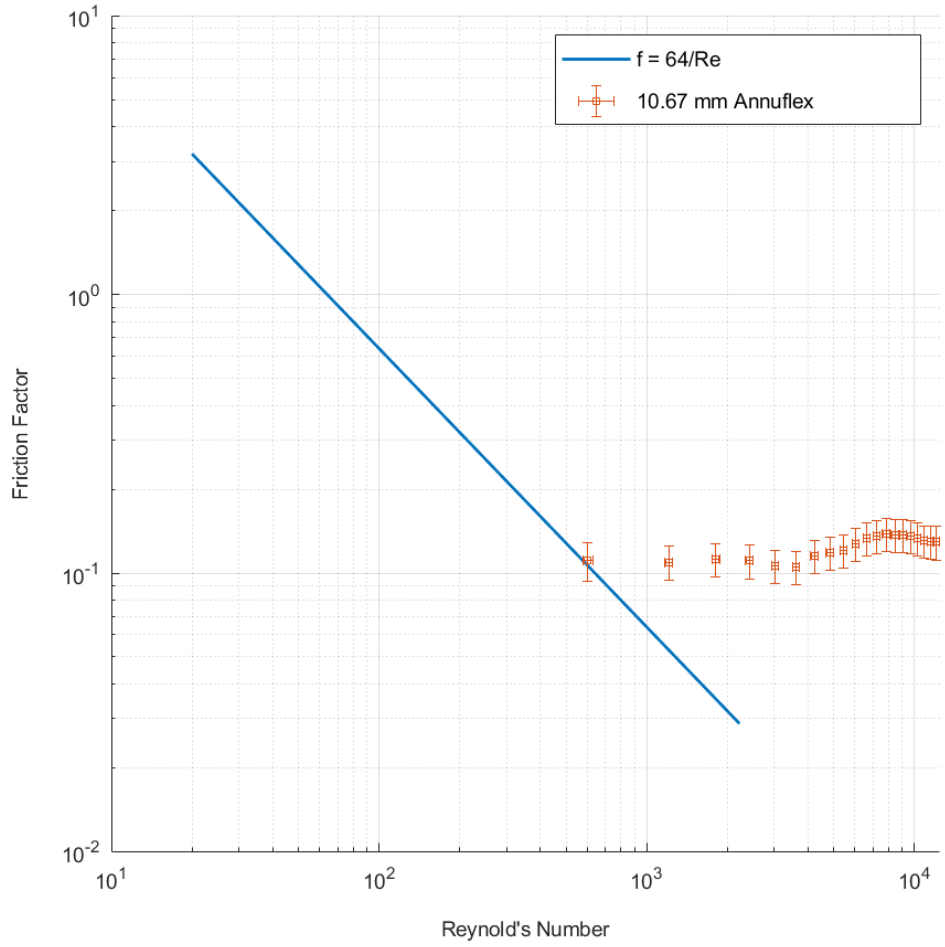

Figure 22 — Phase II friction factor vs Reynolds number for 3/8" Annuflex corrugated line

Figure 22 shows the resulting friction factor vs Reynolds number for the 3/8" Annuflex corrugated line, as per the original statement of work. It is unclear where the separation occurs between laminar and transitional flow, leading to adding a Phase III.

Secondary pressure loss effect of two-dimensional bends

One of the first attempts to theoretically account for the increased pressure losses in two-dimensional bends was Dean [67]-[68] in 1928. He introduced a concept now called Dean vortices, which was verified by Taylor [69]. The curved or bent pipes cause a secondary flow due to centrifugal forces changing the direction of the fluid. After 10 years, Beij published several experimental results [70]-[71] and compared several other experiments which he noted, "represent the best which have been obtained, and that the discrepancies are far too large to be accounted for by experimental errors alone." In 1983, Berger [72] presented a compilation of flow through smooth curved pipes.

The same entry and exit length for fully developed flow Ault [73] extends into curved pipes. Vester [74] is an overview reference for turbulent flow in curved pipes for both experiments and simulations including both 2D and 3D bends.

$$De = \sqrt{\gamma} Re \tag{7}$$

$$\gamma = \frac{R}{R_c} \tag{8}$$

The curvature ratio is limited to the range $0 \leq \gamma \leq 1$ where $\gamma = 0$ for straight pipe and $\gamma = 1$ corresponds to a sharp bend or elbow. Due to the geometry associated with the outer diameter of the corrugation, there is a manufacturing suggested limit on the minimum bend radius allowed for a given line. This would result in an upper limit of the curvature ratio on corrugated lines.

In 1938, Beij [71] produced one of the first studies on water flow through smooth walled pipes for transition and turbulent flow with 2D bends. Sakakibara [75] conducted PIV measurements in smooth walled pipes with 2D bends, focusing on the immediate exit of the bend. Their results show a large, non-uniform instantaneous velocity vector which highlights the importance of where measurements need to be taken in 2D bends. Carlsson [76] contains even more complex swirl switching in turbulent flow in 90-degree bends. Shusser [77] shows computational results for flow in a curved pipe with a sudden expansion, highlighting the lack of expansion into the entire curved surface flow.

An extension of two-dimensional bends is three-dimensional bends including helical smooth and corrugated pipe flow. A recent study by Datta

[78] compares experimental results in smooth pipe flow to computational fluid dynamics. Zachár's [79] CFD was based on the 3D helical experimental data of Datta [78]. Rainieri [80] also produced experimental results for 3D helical shaped on smooth walled pipes.

Table 5 — Summary Literature Review for pressure loss through corrugated pipes with 2D bends

Corrugated Pipe Type		Laminar	Transition	Turbulent
Annular	S-Type/ Transverse		[15]*, [22]*	[15]*, [22]*
	Sinusoidal			
D-Type/Square				
Helical/Spiral			[15]*, [79]‡, [80]*	[15]*
Teardrop				[66]**‡

* Experimental data only

** Analytical only

† Computational Fluid Dynamics only

‡ Experimental and Computational Fluid Dynamics

Table 5 contains a small list of compiled literature with pressure loss results from corrugated pipe flow with 2D bends.

Phase II of the study included measuring the differential pressure loss for 2-dimensional bends of varying bend radii and angles to determine if there was a major contribution of secondary flow effects in annular corrugated pipes. The focus of the work included 2" (or 2.5" a minimum bend radius

exists), 4”, 8”, and 16” in combination with 45°, 90°, 135°, and 180° for all previously collected flow rates. Figure 23 shows a photo of the 3D printed corrugated pipe holders for the 2-dimensional bend testing. The only way this phase was able to be accomplished was due to the automation of the data collection and recollecting of the straight corrugated lines.

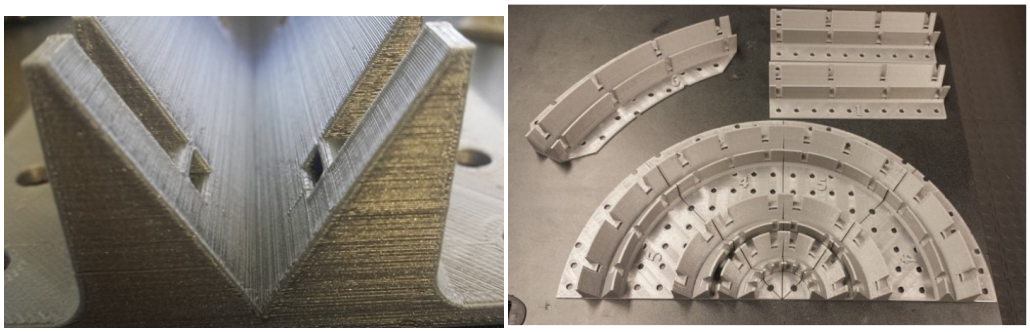

Figure 23 — Photos of 3D printed corrugated pipe holders for 2-dimensional bend testing

With 17 bend configurations for each combination of differential pressure readings collected, the overall magnitude of the secondary flow effects of 2-dimensional bends was not significant enough to differentiate within the uncertainty of the straight corrugated lines. These results are very similar to those presented by Riley [15] & [18]. The major conclusion being that the secondary flow effects are still secondary – even for corrugated pipes. Figure 24 shows an example $^{3}/_{8}$” Annuflex corrugated pipe with all the previous test conditions but normalized with the bend angle and bend radius. Even in the worst-case scenarios, the secondary flow effects were 7-10%

additional pressure loss than the straight corrugated pipes. The rest of this appendix contains the methodology and steps to reach this conclusion.

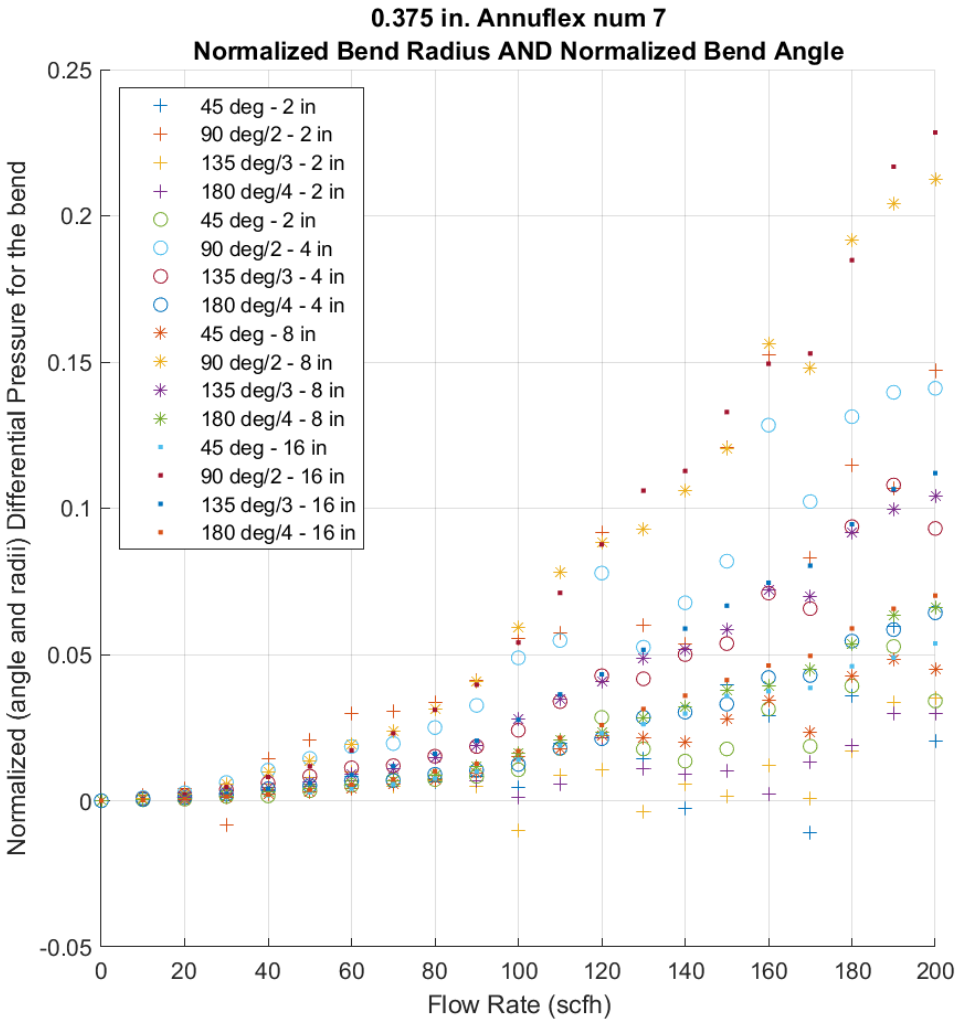

Figure 24 — 3/8" Annuflex with 2D bends – normalized bend radius and bend angle

Figure 25 shows the 3/8" Annuflex corrugated pipe for 2", 4", 8", and 16" bend radii for all the bend angles (45°, 90°, 135°, and 180°) for the

combination set of differential pressures across the bends, which have been subtracted from the straight corrugated pipe flow measurement. One general observation: the longer the arc length is for the bend, the higher the effect of the pressure loss from the bend. Overall, though the maximum pressure loss was found in the 16" and 180-degree bend, ~11 inches of water additional pressure loss due to this bend.

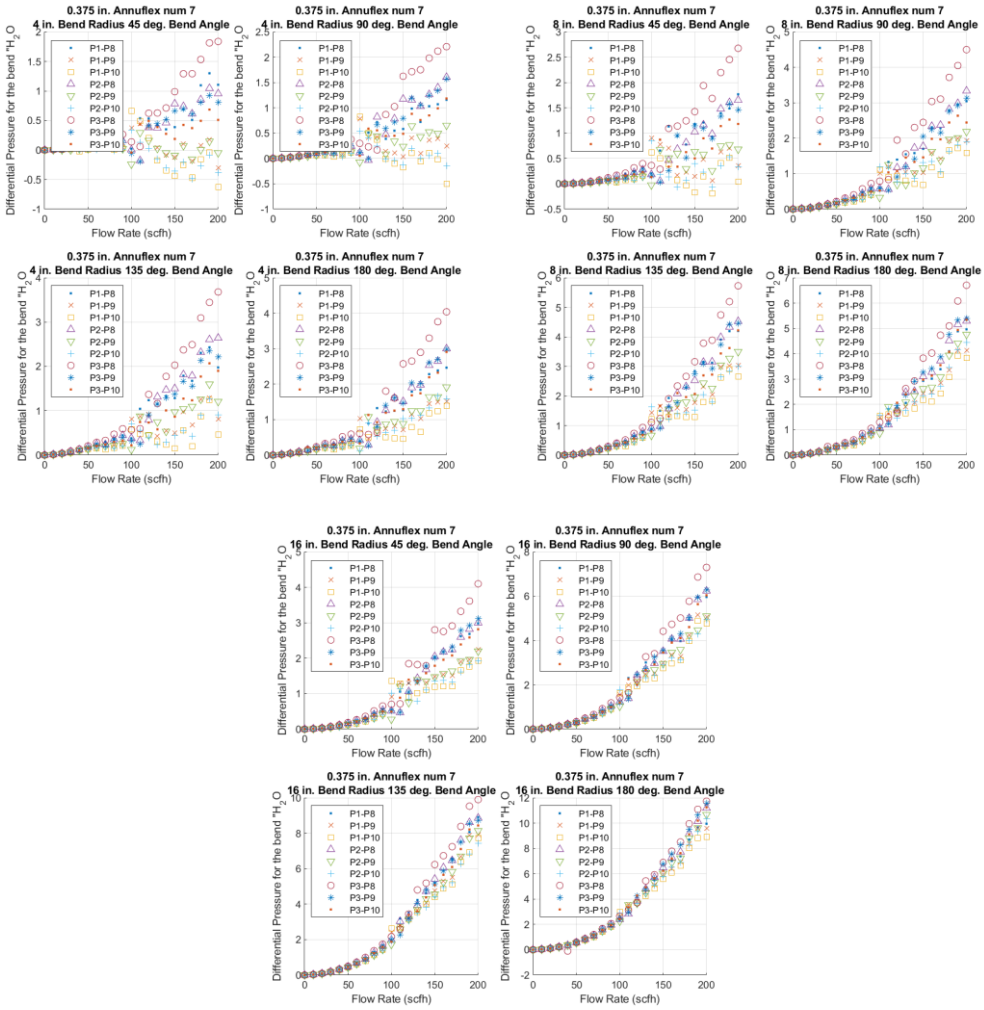

Figure 25 — 3/8" Annuflex with 2D bends

Figure 26 shows the 3/8" Annuflex with 2D bends summarized by bend radius, averaging the different differential pressure per unit lengths. The left plot shows this summary, and the right plot shows the same results but normalized to the 45° bend angle. The results show that the pressure loss for each bend radius is consistent for multiples of bend angles.

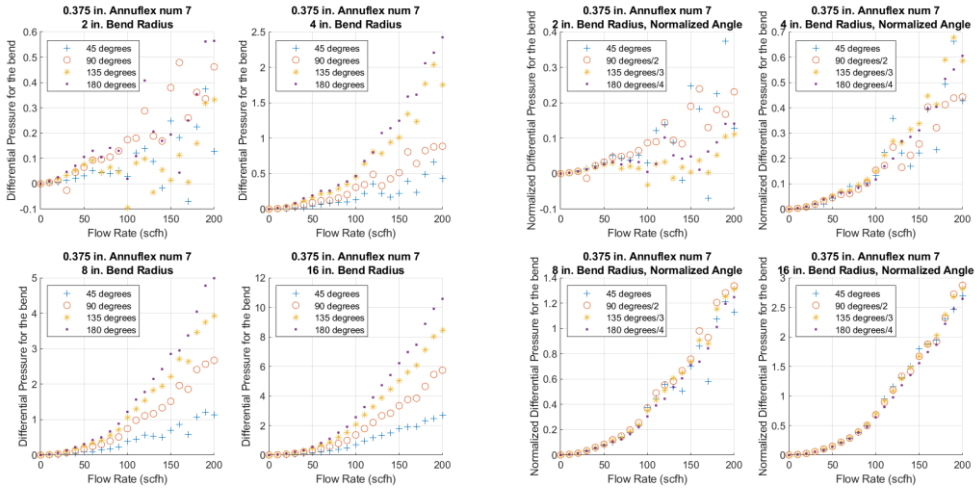

Figure 26 — 3/8" Annuflex with 2D bends – left, all measurements, right normalized to 45-degree bend radius

Phase II Lessons Learned

Control and monitoring automation through externally piloted control valves allowed for any pressure port to be directed to the 'high' and 'low' sides of the differential pressure transducer. Automation becomes necessary when repeated or quick tasks must be accomplished while controlling varying parameters. Appendix A – Experimental Setup (see Figure 33 on pg. 112, Figure 34 on pg. 113, Figure 35 on pg. 114, and Figure 36 on pg. 115) shows the original manual three-way valve manifold, the operational concept with two different examples, and the diagram of the piloted electronic valve system to replace the manual manifold.

Phase III

Upon completion of Phase II, the authors continued the data collection using a higher resolution of mass flow rates – particularly in the laminar to transition region to obtain an improved data set and capture the transitional Reynolds number. The same static pressure locations were used but for a finer resolution of flow rate 0 to 40 scfh by 0.25 scfh. This allowed the capturing of not only the laminar portion but also the transitional Reynolds number to a high degree of fidelity. The transitional Reynolds number is reported in Table 1 on pg. 5.

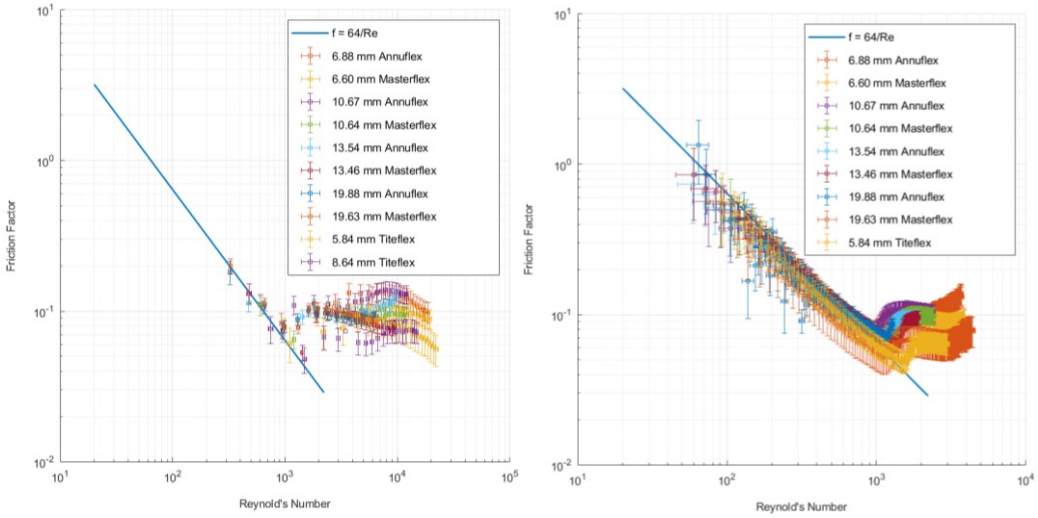

Figure 27 — Comparison of Phase II (left) to Phase III (right) data collection friction factor vs Reynolds number

Figure 27 shows the comparison of the resulting friction factor and Reynolds number calculations for Phase II (left) and Phase III (right). The

results were repeatable between phases for overlapping input set mass flow rates.

The individual corrugation resulting pressure loss per length vs mass flow rate and Reynolds number vs friction factor is located in Appendix C – Plots of Results.

Empirical correlation using Poiseuille Number

An empirical correlation using Poiseuille number grouped current tested corrugated lines by product type or frequency of corrugation pitch relative to minimum/inner diameter.

A correlation for the friction factor for the corrugated lines was developed using the approach for non-circular ducts outlined by Shah and London [3], as cited by White [17]. The correlation uses the Reynolds number based upon the inner diameter (Re_{ID}) and the laminar Poiseuille number (Po) as a function of corrugation height (E) and pitch (or period) of corrugation (P) for laminar flow. The Poiseuille number is the product of the Reynolds number and the Darcy friction factor (f) as shown in equation (5).

$$Po = Re * f \tag{9}$$

For turbulent flow (Re > 2,300), an effective Reynolds number, shown in equation (6), is calculated based on the ratio of the Poiseuille number for pipe flow to the Poiseuille number for rectangular duct flow. The friction factor is then calculated using the Moody chart.

$$\mathrm{Re}_{eff} = \mathrm{Re}_{ID}\left(\frac{\mathrm{Po}_{circular\ cross-section}}{\mathrm{Po}_{corrugated\ line}}\right) \tag{10}$$

In either the laminar or turbulent case, the Poiseuille number, as approached by Shah and London [3], defined in equation (7).

$$\mathrm{Po} = \mathrm{a} + \mathrm{b}\left(\frac{\mathrm{E}}{\mathrm{P}}\right) + \mathrm{c}\left(\frac{\mathrm{E}}{\mathrm{P}}\right)^2 + \mathrm{d}\left(\frac{\mathrm{E}}{\mathrm{P}}\right)^3 + \mathrm{e}\left(\frac{\mathrm{E}}{\mathrm{P}}\right)^4 \tag{11}$$

Where a, b, c, d, and e are coefficients obtained to collapse the data onto a typical circular cross-section pipe flow Moody Chart data fit. For the corrugated line data obtained in the current testing work, the type/product name of the corrugated line yielded different coefficients. Table 6 lists the Poiseuille number coefficients obtained for the three types of corrugated lines tested. Figure 28 illustrates the corrugated line data friction coefficient vs Reynolds number based upon the effective Reynolds number.

Table 6 — Poiseuille Number Empirical Correlation Coefficients

Corrugation Model:		Annuflex	Masterflex	Titeflex
Poiseuille Number Coefficient	a =	12	10	10
	b =	6	11	-2
	c =	-3	-1	2
	d =	-5	-6	5
	e =	2	2	0

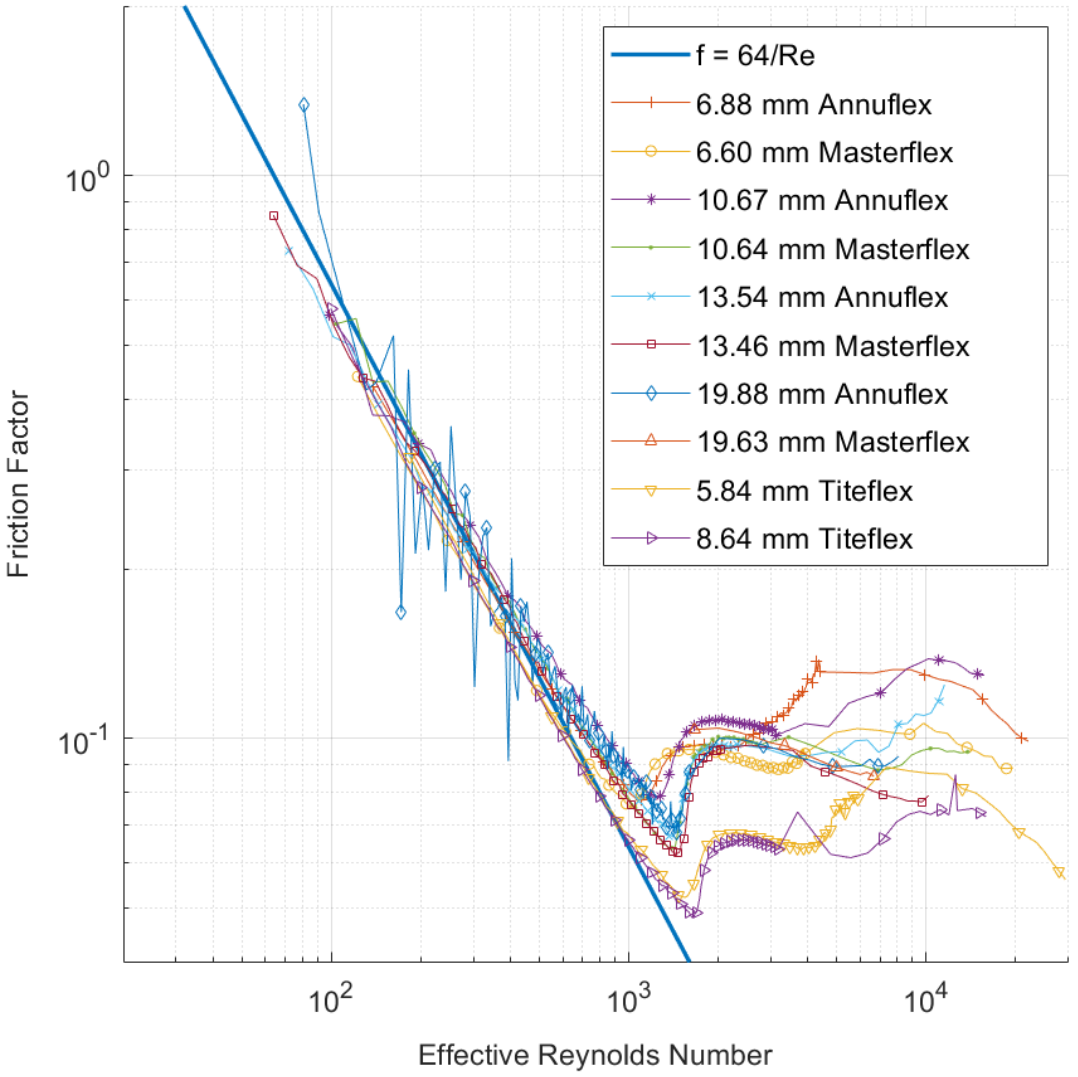

Figure 28 — Friction Factor vs Effective Reynolds Number with Poiseuille Number empirical correlation

This empirical relation will be programmed as an optional feature of NASA Marshall's Space Flight Center's GFSSP [1] program.

Discussion

The referenced authors used various definitions of hydraulic diameter, which change the resulting friction factor and Reynolds number calculations. Their friction factor and Reynolds number presented in this discussion have been transposed from their respective definitions of hydraulic diameter to hydraulic diameter calculated based on the inner diameter to compare directly to our results. From equation (12), the Reynolds number is calculated with the hydraulic diameter, mean velocity, density, and dynamic viscosity. The mean velocity is calculated by taking the volume flow rate (Q) and dividing it by the hydraulic cross-sectional area. Deiber [42] and Russ [38] defined the hydraulic diameter as the mean diameter. Bian [40] used a hydraulic diameter equaling the max diameter. To transpose these values from their referenced documents, the Reynolds number and friction factor were multiplied by $\frac{D_h}{D_{min}}$ and $\left(\frac{D_{min}}{D_h}\right)^5$ respectively.

where:

$$Re = \frac{D_h V\,\rho}{\mu} = \left(\frac{D_{max}\left(\frac{4Q}{\pi D_{max}^2}\right)\rho}{\mu}\right)_{[42]} = \left(\frac{4Q\rho}{\pi\mu D_{max}}\right) \qquad (12)$$

By changing the characteristic length – hydraulic diameter, a multiplication ratio is used (13):

$$\frac{Re_{D_{min}}}{Re_{D_{max}}} = \frac{\left(\frac{4Q\rho}{\pi\mu D_{min}}\right)_{[This\ study]}}{\left(\frac{4Q\rho}{\pi\mu D_{max}}\right)_{[42]}} = \frac{D_{max}}{D_{min}} \tag{13}$$

Similarly, for friction factor (14):

$$f = \frac{\Delta P}{L}\frac{2D_h}{\rho V^2} = \frac{\Delta P}{L}\frac{2D_{max}}{\rho\left(\frac{4Q}{\pi D_{max}^2}\right)^2} = \frac{\Delta P}{L}\frac{\pi^2 D_{max}^5}{8\rho Q^2} \tag{14}$$

Which makes the multiplication ratio (15):

$$\frac{f_{D_{min}}}{f_{D_{max}}} = \frac{\frac{\Delta P}{L}\frac{\pi^2 D_{min}^5}{8\rho Q^2}}{\frac{\Delta P}{L}\frac{\pi^2 D_{max}^5}{8\rho Q^2}} = \left(\frac{D_{min}}{D_{max}}\right)^5 \tag{15}$$

Note: This same exercise is completed to translate the hydraulic diameter definition of Deiber who used the mean diameter to compare with this study using a hydraulic diameter of the minimum diameter. The ratio to translate the Reynolds numbers is linear while for friction factor it is the ratio of the diameters to the 5th power.

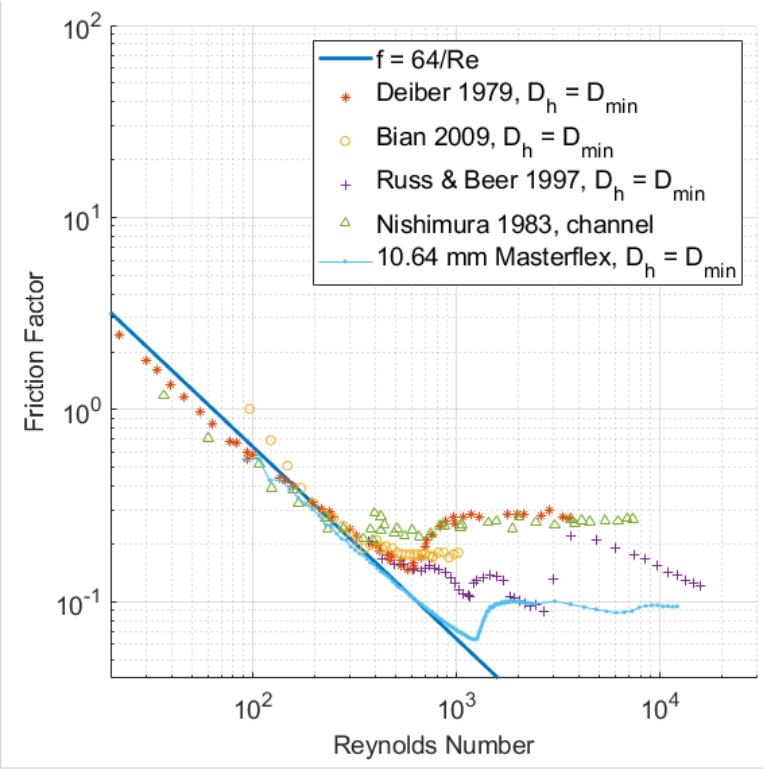

Figure 29 — Friction Factor vs Reynolds number using inner diameter as the definition for hydraulic diameter

Figure 29 shows a comparison between other journal references and a select 10.64 mm Masterflex pipe from this study. The first observation occurs when translating the respective paper's definition of hydraulic diameter, either average diameter or the maximum diameter, to the minimum diameter correlates well to the analytical smooth wall laminar flow definition of f = 64/Re. Furthermore, for much of the laminar regime, the friction factor is less

for a corrugated pipe than an equivalent inner diameter smooth pipe at the same Reynolds number. For laminar flow, the corrugated pipes experienced less pressure loss than a pipe with an equivalent inner diameter, resulting in less friction, due to the flow in the corrugation pockets providing less sheer stress than a solid wall. This result also corresponds with Esquivel [12], where it was noted that all of the flow rates from an imposed pressure gradient per length on a corrugated pipe were more than an equivalent smooth walled pipe, which would imply a lower friction factor. Esquivel [12] conducted a parametric study of the effects of the wall shape on laminar flow in corrugated pipes. For the best comparison, only the symmetric shapes with uniform expansion and contraction are considered.

The next observation, the previous journal papers pipe transitioned from laminar flow at a lower Reynolds number attributed to a larger pitch relative to the inner diameter (P/ID) of 3.5-4.6 compared to this study, which has a (P/ID) between 0.18 and 0.44. The fluid flow has a distance (pitch) to axially traverse before another contraction to the next inner corrugation and the flow expands into the cavity.

Deiber [42] initially noted that if inertial effects are absent there exists a linear relationship between f and Re^{-1}. For low Reynolds number values, the slope is negative 1. Flow separation starts at the diverging portion of the inner

wall and the consequent vortex formation is observed. Quantitative agreement between theory and experiment decreases as one moves into the inertial regime. Transition to turbulent flow is impossible to locate without ambiguity, but this shows the abrupt increase in pressure drop, which is expected at the transition flow rate. Deiber's experiment has a similar transition from laminar flow to transitional flow then a near constant friction factor with increasing Reynolds number-similar to our two tested corrugated pipes (10.64 mm Masterflex and 19.88 mm Annuflex). While other tested corrugated pipes initially exhibit the same behavior, as Reynolds' number continues to increase past 4,000 the friction factor starts to deviate from a constant value. Similar behavior is captured in the Moody diagram with various relative roughness lines until the Reynolds number increases enough past the wholly turbulent flow and the friction factor stays constant.

Russ's [38] results show close similar results for the laminar regime but then vary widely through the transition region. They account for the variances of the experimental apparatus due to the experimental process of sublimating naphthalene which would introduce additional particles and mass into the flow field. The goal was to gain visual effects and to calculate the heat transfer efficiency of the corrugated pipe. Russ' definition of hydraulic diameter was the mean diameter and by rescaling the hydraulic diameter definition to the

inner diameter, the experimental results correlate with previous and current studies. Russ' experimental results are similar to the tested corrugated pipe (8.64 mm Titeflex).

Bian's [40] experimental results contained the largest pitch relative to the inner diameter ratio and the largest depth relative to the inner diameter ratio. After rescaling the results to the hydraulic diameter being defined as the inner diameter, increasing Re > 230, results in a Reynolds number independent of friction factor because of a circulation vortex. Reported results in terms of the outer diameter, but translating the results to the inner diameter reflects the f = 64/Re since the bulk flow is in the center stream of the corrugated pipe and negligible flow occurs in the corrugation pockets. Bian's steady friction factor with increasing Reynolds number for transitional flow is similar to Deiber's results and the two corresponding tested corrugated pipes (10.64 mm Masterflex and 19.88 mm Annuflex). A similar conclusion can be drawn about the experimental results not being fully or wholly turbulent due to the limited tested range of Reynolds numbers.

In 2016, Ünal [23] conducted visualization experiments of a cross-section of a corrugated wall which would create a channel with transparent sides. Ünal identified that flow in a corrugated channel would create a simplified, two-dimensional reflection of a corrugation pipe with a circular

cross-section. This experimental setup was intended to address problems in industry more directly, compared to simplistic corrugation geometries from literature. The results showed a critical Reynolds number at 1,500. Ünal also found that for laminar flow, Reynolds number < 1,300, the motion in the groove is circulatory, resulting in a large stable vortex. For the turbulent flow region (beyond 1,400), however, the vortex in the respective groove propagates to the subsequent groove and erupts intermittently into bulk flow. Ünal's work agrees with the work of Develi and Ahn [43] that studied stainless steel circular corrugation geometries. They found the critical region to be between 1,400 and 1,650 for transition and turbulent starts at 2,000-3,000.

Similar to channel flow, Nishimura [28] and [44] investigated two wavy plates with smooth sides placed at a distance with a medium of glycerol and city water. They found circulated flow vortices occurring at Re = 95-350 (laminar flow, without inertial effects). In this study, the flow becomes unsteady until Re = 670, where the mainstream is violently disturbed by the unsteady vortex motion. At a Reynolds number over 670, the pattern is the same but more violent due to an increase in intensity and frequency. For laminar flow without inertial effects, the friction factor decreases with increasing Reynolds number according to the smooth wall f = 64/Re monotonically until Re = 350. Again, just like with Deiber and Bian, after the

transition Reynolds number, the friction factor seems to become constant with increasing Reynolds number.

Allen's [65] teardrop incompressible experiment observed a transitional "Reynolds number at approximately 1,700 instead of the normal 2,300". Furthermore, the results were similar to our results for the laminar flow. Even though the corrugation pitch geometry was different, the hydraulic diameter definition was based on the inner or minimum diameter.

An empirical correlation for the test data obtained from the corrugated line study has been developed with an effective Reynolds number based on the Poiseuille number. The Poiseuille number is based upon a fourth-order polynomial of the ratio of the corrugated pitch to corrugation height. The coefficients are unique for each type/product name of corrugated line. The results correspond well with the typical pipe flow Moody Chart, but the data is biased to the low end of the effective Reynolds number range, and it is recommended that further test work be executed to provide higher Reynolds number data ($Re_{eff} > 20{,}000$).

The corrugated pipes show good agreement for approximate Reynolds numbers typically found in the laminar flow regime for smooth-wall pipes ($Re < 2{,}300$). The transition point from laminar flow to transitional flow for decreasing Reynolds numbers and increasing inner pipe diameter. The friction

factor correlation to the Reynolds number for laminar flow also follows the same trend, but all lower than f = 64/Re. For larger Reynolds numbers near the smooth-wall pipe turbulent region (Re > 4,000), the corrugated pipes tested show a decrease of friction factor with increasing Reynolds numbers. Several pipes show the same relationship as Popiel, et. al [20] and Bernhard and Hsieh [19], where the friction factor increases with increasing Reynolds number. While some of the pipes seem to converge, it is inconclusive to extrapolate to the full range of the Reynolds number for the Moody diagram correlations where $Re < 10^8$.

Chapter 4
Computational Fluid Dynamics of Corrugated Pipes

Computational Fluid Dynamics (CFD) utilizes numerical methods to solve problems that include fluid flow. The governing differential equation for most CFD problems are the Navier-Stokes equations. The methodology to solve CFD problems include geometry via computer aided drafting (CAD) creation, discretizing the volume (a.k.a. the mesh), defining the physics model(s) of fluid motion and solving techniques, defining the boundary conditions, running the simulation in steady-state or transient and finally using a postprocessor to view the results. The entire CFD process has been privately and commercially implemented throughout various companies. One of the commercial off the shelf solutions is called Simcenter STAR-CCM+ by Siemens. Simcenter STAR-CCM+ is a multiphysics computational fluid dynamics software that enables engineers to create complex models and explore design capabilities to real-word conditions. The objective of the CFD phase was to determine which of the prebuilt in turbulence models closest match the test data.

Nine turbulence models were compared (See List of Abbreviations pg. xvii for reference): KO Standard, Reynolds-Stress, SST M KO, V2F, AKN, SKE L RE, SSA and ST W KO. The total number of CFD cases ran were 2,070 = 10 geometries * 23 flow rates * 9 solvers.

Selection of Geometry to Simulate

Several initial test cases were run to compare the different fidelities of the solution which include: 2D axisymmetric & periodic, 2D axisymmetric, 3D periodic - 1 corrugation, 3D periodic - 5 corrugations, 3D full length of 10 feet. Ideally, the highest level of geometric fidelity (compressible, 3D full 10 feet length) of corrugated pipe should be modeled, but became too computationally expensive (189 million cells, 1 week to converge on 500+ node NASA server) on a single test corrugated geometry at a particular flow rate for a particular turbulence model. Since most of the flow rates and geometry produce a small pressure drop across a small length of simulated section of pipe (5 corrugation pitches) then the simulation can be run with an incompressible assumption. Note the simulations presented in this chapter represent short lengths of pipe where there are minor pressure differences which would result in minor density changes down the length of pipe of less than 5%. With no density change, the pipe simulation of the test section is

assumed repeatable down the entire length of the pipe. End user care needs to be taken when using these simulations for long lengths of pipe or smaller diameter pipes with faster flow rate – resulting in a non-negligible pressure drop across the test section and thus the density does substantially change down the length of the pipe – compressible flow. Chapter 3's application note introduces a theory for using the Fanno Flow relations for adiabatic compressible flow in corrugated pipes. The next few sections describe the 3D periodic CFD cases.

Mesh Description & Grid Independence

Mesh quality was verified and included: Cell skewness angle (<85 degrees), face validity metric (0.5 to 1 [goal]), cell quality metric (0 to 1, 10^-5 bad), volume change metric (0 to 1), chevron quality indicator (0 is good). A grid convergence study was conducted using various densities of meshes and comparing the resulting measured values: net mass flow rate, velocity and static pressure. The mesh had 3 levels of refinement and showed that the resulting measured values did not change greater than 0.1% between meshes. Figure 30 — Sample mesh for 0.25" Annuflex with cross sections at the inner diameter below shows a cross sectional view of the resulting mesh.

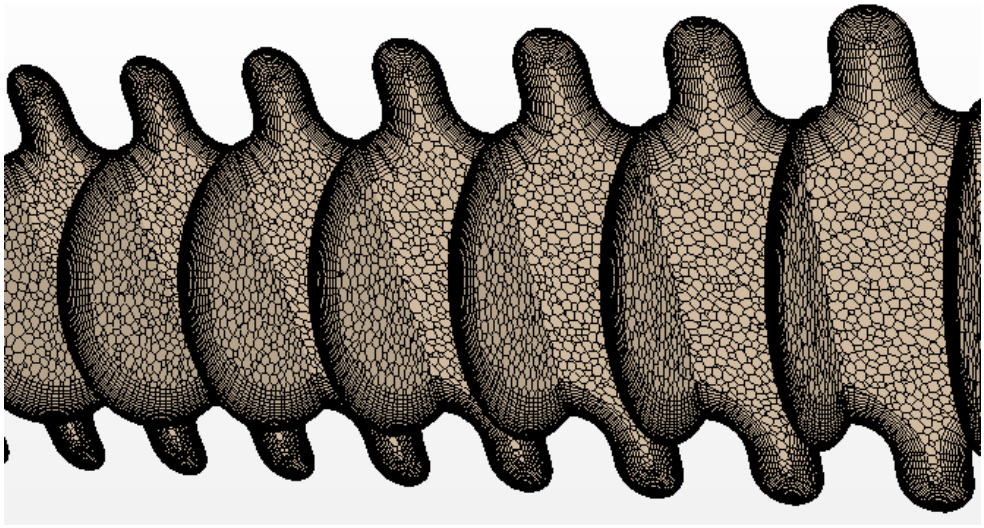

Figure 30 — Sample mesh for 0.25" Annuflex with cross sections at the inner diameter

There are several different wall functions which model the wall functions of the shear stress that the outer wall boundary condition places on the fluid elements. The dimensionless parameter of y+ of less than 1 would resolve the viscous sublayer and gauge which wall function is best represented – calculated by the first cell height at the wall compared to the cell velocity. For the overwhelming majority of the simulations presented the y+ value was much less than 1 due to the low flow with the largest y+ occurring at the fastest flow rate (200 scfh) with the smallest geometry (0.25" Titeflex), but still with a y+ of less than 2.5.

Boundary Conditions

Boundary conditions – the inlet condition is a set target mass flow rate and a periodic boundary condition (repeated to the inlet) was the exit condition. For the CFD cases presented, the 23 target flow rates: 2.5, 5, 7.5, 10, 12.5, 15, 17.5, 20, 22.5, 25, 27.5, 30, 40, 50, 60, 70, 90, 110, 130, 150, 170, 190, 200 standard cubic feet per hour (scfh). These target flow rates were selected to follow more of a representative log scale since the resulting dimensionless parameters are also on a log scale.

Turbulence Modeling

All turbulence models used a low y+ wall treatment except KE Standard which used a Two-Layer All y+ wall treatment. All models used a segregated flow solver with a constant density. All models were 3-dimensional steady state flow.

Note that all turbulence modeling options selected remained with the default implementation for the respective model coefficients. The turbulence models' references include: Lien [99] – RANS, Lien [100] – Low-Re Eddy Viscosity Modelling, Wilcox [101] – Kw revisited, Wilcox [102] – Kw revisited 2, Wray [103] – Low-Re Kw, Abe [104] – New turbulence model, and Davidson [105] – Modified V2F.

StarCCM+ Design Manager Utilization

For comparison and repeatability, there was a single mesh per geometry generated by an external macro (Java script) to import the geometry mesh and not repeat the meshing operation between simulations. Another Java macro was created to automate: importing the geometry mesh between various pipes, resetting the boundary conditions, resetting the derived measurements and derived geometries used in post processing. Additionally, the last converged solution was interpolated as the initial condition onto the next case's flow rate to speed up convergence. Utilizing STAR-CCM+'s design manger allowed for parametric analysis of the geometries and flow rates for each turbulent model in a single simulation. The post processing was focused on comparing the simulated differential pressure over 5 corrugation pitches and the experimental data.

CFD Model Results

To determine the most accurate turbulence model results compared to the experimental results, an average error for all of the set flow rates as in equation (16). This methodology is similar to the uncertainty analysis conducted to get an average weight of the error between the CFD and experimental results.

$$mean\left(\sqrt{\left(\frac{\frac{\Delta P}{L}_{CFD} - \frac{\Delta P}{L}_{experiment}}{\frac{\Delta P}{L}_{experiment}}\right)^2 + \left(\frac{\dot{m}_{CFD} - \dot{m}_{experiment}}{\dot{m}_{experiment}}\right)^2}\right)_{flow\ rates} \quad (16)$$

The results were calculated for a Reynolds Number > 2,000 and displayed in Table 7 for each of the different corrugated pipes and turbulence models. The KE Standard method produced the most accurate pressure loss per length measurements for the set flow rates with an average error of 10%. Furthermore, the CFD results were also calculated for a range of all flow rates that were experimented on including laminar flow presented in Table 14, pg. 157. The KE Standard method remained the most accurate with an average error of 13%. In conclusion, for the 10 tested corrugated pipes with flow rates between zero to 200 scfh, the KE Standard model is recommended with an average error of ~13% and a maximum error of ~20%.

Table 7 — Summary of CFD Turbulence Model Resulting average % error for each geometry for Reynolds Number greater than 2,000

Pipe	KE Std.	KO Std.	Re Stresses	SST M KO	V2F	AKN	SKE L Re	SSA	ST W KO
0.25" Annuflex	12.5	34.5	3.7	24.6	23.9	54.3	17.9	22.3	39.8
0.25" Masterflex	7.8	21.2	13.8	16.8	14.7	32.7	21.5	16.1	25.8
0.375" Annuflex	15.2	16.9	28.6	10.3	5.7	26.1	36.0	6.2	11.7
0.375" Masterflex	14.5	29.8	12.4	21.9	22.5	49.0	17.1	28.3	39.4
0.50" Annuflex	7.5	31.1	7.9	21.8	23.8	44.4	9.6	23.7	32.3
0.50" Masterflex	11.7	27.8	13.2	21.5	23.7	52.9	17.2	28.8	32.7
0.75" Annuflex	3.7	24.6	12.5	17.5	18.9	32.8	8.9	22.1	14.3
0.75" Masterflex	5.9	18.0	11.0	16.9	14.7	41.1	11.1	26.6	34.9
0.25" Titeflex	12.5	12.5	26.1	8.7	11.5	28.5	36.3	12.9	14.9
0.375" Titeflex	9.6	14.6	21.7	6.0	6.9	23.3	25.2	10.0	23.5

Chapter 5
Lessons Learned, Conclusions and Future Work

Lessons Learned

1. Uncertainty analysis can be utilized during all phases of an experimental set up:
    a. Preliminary design/concept – determine the significance and contribution associated with individual types of measurements and their effect on the desired outcome.
    b. Component selection – depending on the analysis above, there is a cost associated with the level of precision required for each type of measurement.
    c. Experimental debugging – if the measured random standard uncertainty is outside of the systematic uncertainty, then there is something not understood or captured through your experimental set up process (i.e., the data collection system recollected a data set if the standard deviation of the differential pressure was above a threshold. The random standard uncertainty (RSU) should have been calculated (standard

deviation of the measurements but divided by the mean of the measurements) and compared to the systematic standard uncertainty to determine if the measurement was at a steady state.)

   d. Reporting uncertainty of results – provide confidence intervals of the independent measured results and how the combination of those uncertainties propagates through to the result.

2. State the standard associated with the mass flow rate. For this dissertation, the standard was 25°C and 14.696 psia. There are different standards and different references which will result in different mass flow rates.
3. Collect instrumented sensors in the most direct and primitive form (i.e. unfiltered, unscaled, unprocessed). More likely than not, there will be a change in the underlying understanding of the processing of the raw data through filtering or various ways to calculate derived measurements. If only the derived measurements are recorded, then the data would have to be manipulated back to the primitive measurements then the new derived measurement process can be applied. If the derived measurement was filtered, then the underlying data might be permanently lost.

4. One test point out of the test matrix should be at the maximum capability of the equipment. During test matrix design, look for opportunities to increase or decrease resolution between test points. For example, Reynolds number vs friction factor is typically plotted on a log-log scale and since Reynolds number is a linear function of mass flow rate, the mass flow rate input test matrix is better suited to be selected on a log scale.

Conclusions

This study developed a new method of measuring differential pressure per unit length of corrugated pipes of various diameters, geometries, and manufacturers. The method was evaluated on 12 different pipes, ten of which were corrugated and two that were smooth. Results from the experimental apparatus were validated through comparison with theoretical flow loss calculations for smooth pipe, having about ~10% deviation from experimental correlations in smooth pipes. Experimentation showed that there is a larger differential pressure loss in corrugated pipes than smooth pipes of equal inner diameter. It also shows that it is much more accurate to model the pipes with an equivalent inner diameter than using the outer diameter with an equivalent surface roughness equal to the corrugation depth.

The developed test apparatus successfully measured differential pressure at varying locations on different pipes. The experimental setup accommodated both corrugated pipes for new data collection, and smooth lines for verification and comparison to theoretical data. Corrugated pipes used in this study came from multiple manufacturers, to demonstrate universality of this experimental setup.

A sufficient number of data points were collected to produce an accurate differential pressure loss per unit length calculation. A comprehensive uncertainty analysis was conducted on the results and the relative error for all test scenarios was 20-25%. Transitional Reynolds number varied based on inner pipe diameter. For laminar flow, the pipes experienced less friction than the standard $f = 64/Re$ due to the corrugation providing a fluid blanket.

This study developed a new method of measuring differential pressure per unit length of corrugated pipes of various diameters, geometries, and manufacturers. The experimental setup was verified on two EMT pipes and then experimentally evaluated on 10 different pipes which were annularly corrugated. The corrugated pipes resulted in approximately a 10% deviation from experimental correlations in smooth pipes for the laminar flow regime. Experimentation resulted in a smaller differential pressure loss in corrugated

pipes than smooth pipes of equal inner diameter. The results from the experimental apparatus were also validated through comparison to theoretical flow loss calculations for smooth pipe and other literature sources.

The experimental setup was capable of accommodating both corrugated lines for new data collection, and smooth lines for verification and comparison to theoretical data. Corrugated lines used in this study came from multiple manufacturers, to demonstrate the universality of this experimental setup. For laminar flow, the pipes experienced less pressure loss, resulting in less friction, due to the corrugation pockets providing a fluid blanket. As a rule of thumb, for laminar flow in corrugated pipes, the inner diameter should be used as the equivalent hydraulic diameter to compare to smooth pipes. A conservative estimate on friction factor for laminar flow through corrugated pipes would be an equivalent pipe with the minimum diameter of the corrugated pipe bounded by the standard laminar correlation of $f = 64/Re$. This remains true until the flow transitions around $1{,}400 < Re < 1{,}600$ for pitch relative to inner diameter ratios between 0.181 to 0.446. An empirical correlation using Poiseuille number grouped current tested corrugated lines by product type or frequency of corrugation pitch relative to minimum/inner diameter.

Secondary flow effects with a single two-dimensional bend produce such an insignificant increase in pressure loss for laminar and transitional flow through corrugated pipes that the recorded values were within our error bars for the uncertainty of the experimental setup.

For the 10 tested corrugated pipes with flow rates between zero to 200 scfh, the KE Standard turbulence model is recommended with an average error of ~13% and a maximum error of ~20%.

Future Work

Determining a relationship for the hydraulic diameter as a function of pipe geometry (and possibly flow rate).

Implement Poiseuille correlation for tested annular corrugated pipe flow into NASA GFSSP [1] software code.

Determine critical Reynolds number for transitional limit in a corrugated pipe.

Determining entrance/exit length associated with corrugated pipes.

Determining flow-induced vibration magnitude and tonal noise frequency of corrugated pipe flow.

High fidelity numerical solution, direct numerical simulation (DNS) of pressure loss through corrugated pipes with measured geometric parameters.

References

[1] Majumdar, A. K., LeClair, A. C., Moore, R., and Schallhorn, P. A., 2015, "Generalized Fluid System Simulation Program (GFSSP), Version 6," 51st AIAA/SAE/ASEE Jt. Propuls. Conf., pp. 1–25, DOI:10.2514/6.2015-3850.

[2] Moody, L. F., 1944, "Friction Factors for Pipe Flow," Trans. ASME. DOI:10.1115/1.4018140.

[3] Brown, G. O. "The History of the Darcy-Weisbach Equation for Pipe Flow Resistance." Environmental and Water Resources History Sessions: *ASCE Civil Engineering Conference and Exposition* 2002. Washington, D.C. DOI:10.1061/40650(2003)4.

[4] Haaland, S. E., 1983, "Simple and Explicit Formulas for the Friction Factor in Turbulent Pipe Flow," ASME J. Fluids Eng., **105**(1), pp. 89–90. DOI:10.1115/1.3240948.

[5] Colebrook, C. F., 1939, "Turbulent Flow in Pipes with Particular Reference to the Transition Region between the Smooth and Rough Pipe Laws," J. Inst. Civ. Eng. London, **11**, pp. 133–156. DOI:10.1680/ijoti.1939.13150.

[6] LaViolette, M., 2017, "On the History, Science, and Technology Included in the Moody Diagram." ASME J. of Fluids Eng., **139**(3) pp. 030801. DOI:10.1115/1.4035116.

[7] Yang, S., and Ding, D., 2014. “Drag-Reducing Flows in Laminar-Turbulent Transition Region.” ASME J. of Fluids Eng., **136**(10) pp. 101202-101202-9. DOI:10.1115/1.4027455.

[8] Sletfjerding, E., and Gudmundsson J. S., 2003. “Friction Factor Directly From Roughness Measurements.” ASME J. of Energy Resources Technology, **125**(2) pp: 126-130. DOI:10.1115/1.1576264.

[9] Afzal, N., 2007. “Friction Factor Directly From Transitional Roughness in a Turbulent Pipe Flow.” ASME J. of Fluids Eng., **129**(10) pp. 1255-1267. DOI:10.1115/1.2776961.

[10] Willis, A. P., Peixinho, J., Kerswell, R. R., and Mullin, T., 2008. “Experimental and theoretical progress in pipe flow transitions.” Phil. Trans. R. Soc. A. **366** pp. 2671-2674. DOI:10.1098/rsta.2008.0063.

[11] Jiménez, Javier. 2004. "Turbulent Flows over Rough Walls." Annual Review of Fluid Mechanics 36: pp. 173-196. DOI:10.1146/annurev.fluid.36.050802.122103.

[12] Esquivel, P. I. R. & Boonkkamp, J.H.M. Dam, J. and Mattheij, Robert M. M., 2011. “A Parametric Study of the Effect of Wall-Shape on Laminar Flow in Corrugated Pipes.” ASME-JSME-KSME 2011 Joint Fluids Engineering Conference, AJK. pp. 1389-1398. DOI:10.1115/AJK2011-03044.

[13] Sakar, M., Paramane, S. & Sharma, A., 2017. “Periodically Fully Developed Heat and Fluid Flow Characteristics in a Furrowed Wavy Channel.” Heat Transfer Engineering. **38**(2) pp. 278-288. DOI:10.1080/01457632.2016.1177434.

[14] Calomino, F., Alfonsi, G., Gaudio, R., D'Ippolito, A., Lauria, A., Tafarojnoruz, A. and Artese, S. 2018. "Experimental and Numerical Study of Free-Surface Flows in a Corrugated Pipe." Water. **10**(5) p. 638. DOI:10.3390/w10050638.

[15] Riley, K. L., Langley, J. R., Pressburg, B. S., and Whitehurst, C. A., 1966. "Flow losses in flexible hose." Southeastern symposium on missiles and aerospace vehicles. American Astronautical Society. https://ntrs.nasa.gov/api/citations/19660024205/downloads/19660024205.pdf.

[16] Shah, R. K., and London, A. L., 1978, Laminar Flow Forced Convection in Ducts, Academic Press, New York. DOI:10.1016/C2013-0-06152-X

[17] White, F. M., 1991, Viscous Fluid Flow, McGraw Hill, New York. ISBN: 9781264423101

[18] Riley, K. L. 1967. "Flow Losses in Flexible Hose." PhD diss., Louisiana State University. https://repository.lsu.edu/gradschool_disstheses/1313.

[19] Bernhard, D. M. and Hsieh, C. K. 1995, "Pressure Drop in Corrugated Pipes." ASME J. of Fluids Eng. **118**(2), pp. 409-410. DOI:10.1115/1.2817393.

[20] Popiel, C. O., Kozak, M., Malecka, J., and Michalak, A., 2013, "Friction Factor for Transient Flow in Transverse Corrugated Pipes." ASME J. of Fluids Eng. **135**(7), pp. 074501-074501-4. DOI:10.1115/1.4023945.

[21] van der Linden, B. J., Ory, E., Dam, J., and Tijsseling, A. S., Pisarenco, M., 2009. “Efficient Computation of Three-Dimensional Flow in Helically Corrugated Hoses Including Swirl.” ASME Paper No. PVP2009-77997. DOI: 10.1115/PVP2009-77997

[22] Ahn, H., and Uslu, I., 2013, “Experimental Investigation on Pressure Drop in Corrugated Pipes.” Proceedings of the ASME 2013 International Mechanical Engineering Congress & Exposition. pp. V07AT08A050. DOI:10.1115/IMECE2013-66061.

[23] Ünal, E., Ahn, H., and Sorguven, E., 2016, "Experimental Investigation on Flows in a Corrugated Channel." ASME. J. of Fluids Eng., **138**(7) p. 070908. DOI:10.1115/1.4032754.

[24] Daniels, C.M., 1956. “Pressure losses in flexible metal tubing.” Prod. Eng. **34** pp. 223–227.

[25] Daniels, C.M., Cleveland, J. R., 1965. “Determining pressure drop in flexible metal hose.” Machine Des. pp.187–8.

[26] Jaiman, R. K., Oakley, O. H. Jr., and Adkins, J. D., 2010, "CFD Modeling of Corrugated Flexible Pipe." Proceedings of the OMAE2010 29th International. Shanghai, China. pp. 661-670. DOI:10.1115/OMAE2010-20509.

[27] Calomino, F., Tafarojnoruz, A., De Marchis, M.; Gaudio, R.; and Napoli, E. 2015. “Experimental and Numerical Study on the Flow Field and Friction Factor in a Pressurized Corrugated Pipe.” ASCE Journal of Hydraulic Engineering. **141**(11) pp. 04015027-04015027-12. DOI:10.1061/(ASCE)HY.1943-7900.0001046.

[28] Nishimura, T., Ohori, Y., and Kawamura, Y., 1984, “Flow Characteristics in a Channel With Symmetric Wavy Wall for Steady Flow,” J. Chem. Eng. Jpn., **17** pp. 466–471. DOI:10.1252/jcej.17.466.

[29] Gibson, A. H., 1925. “The flow of water in a corrugated pipe.” The London, Edinburgh, and Dublin Philosophical Magazine and Journal of Science. Series 6. **50**(295) pp. 199-204. DOI:10.1080/14786442508634731.

[30] Jotkar, M. R., Swaminathan, G., Sahu, K. C., and Govindarajan, R., 2016, "Global Linear Instability of Flow Through a Converging-Diverging Channel." ASME J. of Fluids Eng., **138**(3) p. 031301. DOI:10.115/1.4031429.

[31] Konda, H., Kumar Tripathi, M., and Chandra Sahu, K., 2016, “Bubble Motion in a Converging–Diverging Channel,” J. Fluids Eng., 138(6), DOI:10.1115/1.4032296.

[32] Lahbabi, A., and Chang, H., 1986. “Flow in periodically constricted tubes: Transition to inertial and nonsteady flows.” Chemical Engineering Science. **41**(10) pp. 2487-2505. DOI:10.1016/0009-2509(86)80034-3.

[33] Esquivel, P. I. R. & Boonkkamp, J.H.M. and Dam, J., 2012. “An asymptotic formula for the friction factor of laminar flow in pipes of varying cross section.” Mathematics in Engineering, Science, and Aerospace. **3**(1). pp. 63-78.

[34] Inaba, T., Ohnishi, H., Miyake, Y., and Susmu, M. 1979. “Laminar flow in Corrugated Pipe.” JSME. **22**(171). pp. 1198-1204. DOI: 10.1299/jsme1958.22.1198.

[35] Cotrell, D. L., McFadden, G. B., and Alder, B. J. 2008. "Instability in Pipe Flow." Proceedings of the National Academy of Sciences of the United States of America. **105**(2) pp. 482-430. DOI:10.1073/pans.0709172104.

[36] Shipton, R. J., 1976. "Flow in Corrugated Pipes." Journal of the Hydraulics Division, **102**(9), pp. 1343-1351. DOI: 10.1061/JYCEAJ.0004616.

[37] Webster, M. J., 1959. "Friction Factors in Corrugated Metal Pipe." Journal of the Hydraulics Division. **85**(9) pp. 35-67. DOI: 10.1061/JYCEAJ.0000348.

[38] Russ, G., and Beer, H. 1996. "Heat transfer and flow field in a pipe with sinusoidal wavy surface-II. Experimental investigation." International Journal of Heat and Mass Transfer. 40(5) pp. 1071-1081. DOI:10.1016/0017-9310(96)00159-7.

[39] Kim, Y. J., Kim, M., Kim, S., Min, J., and Ha, M., 2016. "Numerical study of fluid flow and convective heat transfer characteristics in a sinusoidal wavy circular tube." Journal of Mechanical Science and Technology. **30**(3) pp. 1885-1196. DOI:10.1007/S12206-0222-6.

[40] Bian, Y., and Baoju, J., 2009. "Mass transfer characteristics in an axisymmetric wavy-walled tube for pulsatile flow with backward flow." Heat Mass Transfer. **45** pp. 693-702. DOI:10.1007/s00231-008-0471-8.

[41] Mahmud, S., Sadrul Islam, A. K. M., Feroz, C. M., 2003. "Flow and heat transfer characteristics inside a wavy tube." Heat and Mass Transfer. **39** pp. 387-393. DOI:10.1007/s00231-002-0369-9.

[42] Deiber, J. A., and Schowalter, W. R., 1979. “Flow through tubes with sinusoidal axial variations in diameter.” American Institute of Chemical Engineers Journal, **25**(4), pp. 638–645. DOI:10.1002/aic.690250410.

[43] Develi, A. C., and Ahn, H., 2015, “Experimental Investigation on Friction and Acoustics in Corrugated Pipes,” International Conference on Advances in Mechanical Engineering, Istanbul, Turkey, Paper No. ICAME2015-298. DOI:10.1115/IMECE2013-66061.

[44] Nishimura, T., and Matsune, S., 1998. “Vortices and wall shear stress in asymmetric and symmetric channels with sinusoidal wavy walls for pulsating flow at low Reynolds numbers.” International Journal of Heat and Fluid Flow. 19 pp. 583-593. DOI:10.1016/S0142-727X(98)10005-X.

[45] Chow, J. C. F., and Soda, K., 1972. “Laminar Flow in Tubes with Constriction.” The Physics of Fluids. **15**(10), pp. 1700-1706. DOI:10.1063/1.1693765.

[46] Saha, S., Klewicki, J. C., Ooi, A., and Blackburn, H. M., 2015. “On scaling pipe flows with sinusoidal transversely corrugated walls: analysis of data from the laminar to the low-Reynolds-number turbulent regime.” J. Fluid Mech. (Cambridge University Press) **779** pp. 245-274. DOI:10.1017/jfm.2015.414.

[47] Loh, S. A., and Blackburn, H. M., 2011. "Stability of steady flow through an axially corrugated pipe." Physics of Fluids **23**(11) p. 111703. DOI:10.1063/1.3660522.

[48] Stel, H., Morlaes, R. E. M., Franco, A. T., Junqueira, S. L. M., Erthal, R. H., and Gonçalves, M. A. L., 2010, "Numerical and Experimental Analysis of Turbulent Flow in Corrugated Pipes." ASME J. of Fluids Eng. **132**(7), pp. 071203-071203-13. DOI:10.1115/1.4002035.

[49] Stel, H., Franco, A. T., Junqueira, S. L. M., Erthal, R. H., Mendes, R., Gonçalves, M. A. L., and Morales, R. E. M., 2012, "Turbulent Flow in D-Type Corrugated Pipes: Flow Pattern and Friction Factor." ASME J. of Fluids Eng., **134**(12) p. 121202. DOI:10.1115/1.4007899.

[50] Ohira, K., Okuyama, J., Nakagomi, K., and Takahashi, K., 2012, "Pressure drop of slush nitrogen flow in converging-diverging pipes and corrugated pipes." Elsevier Cryogenics, **52** pp. 771-783, DOI:10.1016/j.cryogenics.2012.09.001.

[51] Djenidi, L., R. Elavarasan, and R. A. Antonia. 1999. "The turbulent boundary layer over transverse square cavities." J. of Fluid Mech. (Cambridge University Press) **395** pp. 271-294. DOI:10.1017/S0022112099005911.

[52] Vijiapurapu S., Cui, J., 2007, "Simulation of Turbulent Flow in a Ribbed Pipe Using Large Eddy Simulation." Numerical Heat Transfer, Part A: Applications: An International Journal of Computation and Methodology, **51**(12), p. 1137-1165, DOI:10.1080/10407780601112829.

[53] Ismail, O.S. and Tairu, O. O., 2012. "Effects of Pipes Corrugated Shapes on the Friction Factor." HEFAT. http://hdl.handle.net/2263/44838.

[54] Silberman, E. F., 1970. "Effect of Helix Angle on Flow in Corrugated Pipes." Journal of the Hydraulics Division, **96**(11), pp. 2253-2263. DOI: 10.1061/JYCEAJ.0002760.

[55] Aroonrat, K., Dalkilic, A. S., and Wongwises, S., 2013, "Experimental Study on Evaporative Heat Transfer and Pressure Drop of R-134a Flowing Downward Through Vertical Corrugated Tubes with Different Corrugation Pitches." Experimental Heat Transfer. **26**(1) pp. 41-63. DOI:10.1080/08916152.2011.631080.

[56] Pisarenco, M., Linden, B., Tijsseling, A., Ory, E., and Dam, J., 2011, "Friction Factor Estimation for Turbulent Flows in Corrugated Pipes with Rough Walls." ASME Journal of Offshore Mechanics and Arctic Engineering. **133**(1). DOI:10.1115/1.4001439.

[57] Kareem, Z. S., Abdullah, S., Lazim, T. M., Jaafar, M. N. M., and Wahid, A. F. A., 2015. "Heat transfer enhancement in three-start spirally corrugated tube: Experimental and numerical study." Chemical Engineering Science. **134**. pp. 746-757. DOI:10.1016/j.ces.2015.06.009.

[58] Wang, C. Y., 2006. "Effect of Helical Corrugations on the Low Reynolds Number Flow in a Tube." AIChE Journal. Fluid Mechanics and Transport Phenomena. **52** pp. 2008-2012. DOI:10.1002/aic.10817.

[59] Darzi, A. A. R., Farhadib, M., Sedighia, K., Shafaghata, R., Zabihic, K., 2012. "Experimental investigation of turbulent heat transfer and flow characteristics of SiO_2/water nanofluid within helically corrugated tubes." International Communications in Heat and Mass Transfer. **39**(9). pp. 1425-1434. DOI:10.1016/j.icheatmasstransfer.2012.07.027.

[60] García, A., Solano, J. P., Vicente, P. G., and Viedma, A., 2012, "The Influence of Artificial Roughness Shape on Heat Transfer Enhancement: Corrugated Tubes, Dimpled Tubes and Wire Coils," Applied Thermal Eng., **35**. pp. 196–201. DOI:10.1016/j.applthermaleng.2011.10.030.

[61] De Azevedo, H. S., Morales, R. E. M., Franco, A. T. F., Junqueira, S. L. M., Erthal, R. H., and Goncalves, M., 2008, "Numerical Simulation of Turbulent Flow in Corrugated Pipes." 12th Brazilian Congress of Thermal Engineering and Sciences.
https://abcm.org.br/app/webroot/anais/encit/2008/artigos/6_5112.pdf.

[62] Selvam, K., Öngüner, E., Peixinho, J., and Zanoun, E., 2018. "Wall Pressure in Developing Turbulent Pipe Flows." ASME J. of Fluids Eng., **140**(8) pp. 081203-081203-7. DOI:10.1115/1.4039294.

[63] Joshi, Y., and Vinoth, B.R., 2018. "Entry Lengths of Laminar Pipe and Channel Flows." ASME J. of Fluids Eng., **140**(6) pp. 061203-061203-8. DOI:10.1115/1.4038668.

[64] Pethkool S., Eiamsa-ard, S., Kwankaomeng, S., and Promvonge, P., 2011, "Turbulent Heat Transfer Enhancement in a Heat Exchanger Using Helically Corrugated Tube," Int. Commun. Heat Mass Transf., 38, pp. 340–347. DOI:10.1016/j.icheatmasstransfer.2010.11.014.

[65] Allen, J. 1964. "Flow of incompressible fluids through corrugated pipes", The Institute of Civil Engineers., **28** pp. 31-38. DOI:10.1680/iicep.1964.10120.

[66] Hawthorne, R.C., Von Helms, H. C., 1963. "Fluid expansion theory computes flow in corrugated hose." Prod. Eng. **34** pp. 98–100.

[67] Dean, W.R. M.A., 1928. “LXXII. The stream-line motion of fluid in a curved pipe (Second paper).” The London, Edinburg, and Dublin Philosophical Magazine and Journal of Science. B(30), 673-695, DOI:10.1080/14786440408564513

[68] Dean, W. R., 1927, “Note on the Motion of Fluid in a Curved Pipe,” Philos. Mag., 4(20), pp. 208–223. 10.1112/S0025579300001947

[69] Taylor, G. I., and F. R. S., 1929. “The Criterion for Turbulence in Curved Pipes.” Yarrow Research Professor of the Royal Society. **124** pp. 243-249. DOI:10.1098/rspa.1929.0111.

[70] Keulegan, G. H., and Beij, K. H., 1937. “Pressure losses for fluid flow in curved pipes.” Research Paper RP965. Journal of Research of the National Bureau of Standards **18** pp. 89-114. https://nvlpubs.nist.gov/nistpubs/jres/18/jresv18n1p89_a1b.pdf

[71] Beij, K. H., 1938. “Pressure Loss for Fluid Flow in 90° pipe bends.” Journal of Research of the National Bureau of Standards. **21** pp. 1-18. https://nvlpubs.nist.gov/nistpubs/jres/21/jresv21n1p1_A1b.pdf

[72] Berger, S. A., Talbot, L., and Yao, L. S., 1983. “Flow in Curved Pipes.” Annual Review of Fluid Mechanics **15** pp. 461-512. DOI:10.1146/annurev.fl.15.010183.002333.

[73] Ault, J., Rallabandi, B., Shardt, O., Chen, K., and Stone, H., 2017. "Entry and exit flows in curved pipes." J. of Fluid Mech. (Cambridge University Press) **815** pp. 570-591. DOI:10.1017/jfm.2017.72.

[74] Vester, A. K., Örlü, R., Alfredsson, P. H., 2016. "Turbulent Flows in Curved Pipes: Recent Advances in Experiments and Simulations." ASME Appl. Mech. Rev. **68**(5). pp. 050802-050802-25. DOI:10.1115/1.4034135.

[75] Sakakibara, J., and Machida, N., 2012. "Measurement of turbulent flow upstream and downstream of a circular pipe bend." Physics of Fluids **24** p. 041702. DOI:10.1063/1.4704196.

[76] Carlsson, C., Alenius, E., and Fuchs, L., 2015. "Swirl switching in turbulent flow through 90° pipe bends." Physics of Fluids, **27** p. 085112. DOI:10.1063/1.4928971.

[77] Shusser, M., Ramus, A., and Gendelman, O., 2016. "Flow in a Curved Pipe with a Sudden Expansion." ASME J. of Fluids Eng., **138**(2) p. 021203. DOI:10.1115/1.4031259.

[78] Datta, A. K., Hayamizu, Y., Kouchi, T., Nagata, Y., Yamamoto, K., and Yanase, S., 2017. "Numerical Study of Turbulent Helical Pipe Flow With Comparison to the Experimental Results." ASME J. of Fluids Eng., **139**(9) p. 091204. DOI:10.1115/1.4036477.

[79] Zachár, A. 2010. "Analysis of coiled-tube heat exchangers to improve heat transfer rate with spirally corrugated walls." International Journal of Heat and Mass Transfer. **53**(19-20) pp. 3928-3939. DOI:10.1016/j.ijheatmasstransfer.2010.05.011.

[80] Rainieri, S., Bozzoli, F., Cattani, L., and Pagliarini, G. 2013. “Compound convective heat transfer enhancement in helically coiled wall corrugated tubes.” International Journal of Heat and Mass Transfer. **59** pp. 353-362. DOI: 10.1016/j.ijheatmasstransfer.2012.12.037.

[81] Mitchell, W., Blagun, B., Johnson, D., and Midgett, M., 2002. “Angular Flow Insensitive Pitot Tube Suitable for use with Standard Stack Testing Equipment.” U.S. Environmental Protection Agency, Washington, D.C., EPA/600/4-79/042 (NTIS PB80102007).

[82] Eaton, J., and Johnston, J., 1981. "A Review of Research on Subsonic Turbulent Flow Reattachment", AIAA Journal, **19**(9) pp. 1093-1100. DOI:10.2514/3.60048.

[83] Ma. X., Geisler, R., and Schröder, A., 2017. “Experimental Investigation of Separated Shear Flow under Subharmonic Perturbations over a Backward-Facing Step.” J. Flow, Turbulence and Combustion. **99**(1) pp. 71–91. DOI:10.1007/s10494-017-9814-1.

[84] Wengle, H., Huppertz, A., Barwolff, G., and Janke, G., 2001. “The manipulated transitional backward-facing step flow: an experimental and direct numerical simulation investigation.” Eur. J. Mech. B-Fluids **20**(1) pp. 25–46. DOI:10.1016/S0997-7546(00)01105-5.

[85] Šarić, S., Jakirlić, S., and Tropea, C. 2005, “A Periodically Perturbed Backward-Facing Step Flow by Means of LES, DES and T-RANS: An Example of Flow Separation Control.” ASME J. of Fluid Eng. **127**(5) pp. 879-887. DOI:10.1115/1.2012502.

[86] Roache, P. J., 2016, "Verification and Validation in Fluids Engineering: Some Current Issues." ASME J. of Fluids Eng., **138**(10) p. 101205. DOI:10.1115/1.4033979.

[87] Blackburn, H. M., Ooi, A., and Chong, M. S., 2007. "The effect of corrugation height on flow in a wavy-walled pipe." 16th Australasian Fluid Mechanics Conference. https://www.researchgate.net/publication/43472471

[88] Coleman, H. W., and Steele, W. G., *Experimentation, Validation, and Uncertainty Analysis for Engineers*. 3rd ed. Hoboken, N.J.: John Wiley & Sons, 2009. ISBN:978-0-470-16888-2.

[89] Rudenko, O., Nakiboğlu, G., Holten, A., and Hirschberg, A. 2013. "On whistling of pipes with a corrugated segment: Experiment and theory." Journal of Sound and Vibration. 332. pp.7226-7242. DOI:10.1016/j.jsv.2013.08.034.

[90] Popescu, M., Johansen, S., and Shyy, W., 2011, "Flow-Induced Acoustics in Corrugated Pipes." Commun. Comput. Phys. **10**(1), pp. 120-139, DOI:10.4208/cicp.301209.230710a.

[91] Ziada, S., and Lafon, P., 2014. "Flow-Excited Acoustic Resonance Excitation Mechanism, Design Guidelines, and Counter Measures." ASME Applied Mechanics Reviews, **66**(1) pp. 010802-010802-22. DOI:10.1115/1.4025788.

[92] Balaguru, R., "Acoustical Studies on Corrugated Tubes." PhD diss. Stevens Institute of Technology, 2014.

[93] Rajavel, B. and Prasad, M.G., 2013. “Acoustics of Corrugated Pipes: A Review." ASME Applied Mechanics Reviews. **65**(5) pp. 1-24. DOI:10.1115/1.4025302.

[94] Rudenko, O., Nakiboğlu, G., and Hirschberg, A., 2014. “Onset of Flow Induced Tonal Noise in Corrugated Pipe Segments.” ASME J. of Pressure Vessel Technology. **136**(5) p. 051308. DOI:10.1115/1.4026595.

[95] Crawford, F. S., 1973. “Singing corrugated pipes.” Lawrence Berkeley National Laboratory.

[96] Cadwell, L. 1994. “Singing corrugated pipes revisited.” American Association of Physics Teachers. DOI: 10.1119/1.17600.

[97] Golliard, J., and Nakiboğlu, G., 2013. “U-RANS model for the prediction of the acoustic sound power generated in a whistling corrugated pipe.” ASME Pressure Vessels and Piping Conference. pp. V004T04A040-6. DOI:10.1115/PVP2013-97385.

[98] Tonon, D., Landry, B. J. T., Belfroid, S. P. C., Willems, J. F. H., Hofmans, G. C. J., Hirschberg, A., 2010. “Whistling of a pipe system with multiple side branches: Comparison with corrugated pipes.” Journal of Sound and Vibration. **329**(8) pp. 1007-1024. DOI:10.1016/j.jsv.2009.10.020.

[99] Lien, F. S., Kalitzin, G., and Durbin, P. A., 1998. “RANS modeling for compressible and transitional flows.” Center for Turbulence Research.

[100] Lien, F.S., Chen, W. L., and Leschziner, M.A., 1996. "Low-Reynolds-Number Eddy-Viscosity Modelling Based on Non-Linear Stress-Strain/Vorticity Relations." Engineering Turbulence Modelling and Experiments 3. pp. 91-100.

[101] Wilcox, D., 2007. "Formulation of the κ-ω Turbulence Model Revisited." 45th AIAA Aerospace Sciences Meeting and Exhibit. DOI:10.2514/6.2007-1408.

[102] Wilcox, D., 2008. "Formulation of the κ-ω Turbulence Model Revisited." AIAA Journal. **46**(11) pp. 2823-2838 DOI:10.2514/1.36541.

[103] Wray, T. J., and Agarwal, R. K., 2014. "A New Low Reynolds Number One-Equation Turbulence Model based on a κ-ω Closure." AIAA Aviation Forum DOI:10.2514/6.2014-2208.

[104] Abe, K., Kondoh, T., and Nagano, Y., 1994. "A new turbulence model for predicting fluid flow and heat transfer in separating and reattaching flows-I. Flow field calculations." Int. J. Heat Mass Transfer. 37(1) pp. 139-151. DOI: 10.1016/0017-9310(94)90168-6

[105] Davidson, L., Nielsen, P. V., Sveningsson, A., 2003. "Modifications of the V2 Model of Computing the Flow in a 3D Wall Jet." In Proceedings of the International Symposium on Turbulence, Heat and Mass Transfer. pp. 577-584.

[106] Brown, K. K., Coleman, H. W., Steele, W. G., and Taylor, R. P., 1996. "Evaluation of Correlated Bias Approximations in Experimental Uncertainty Analysis." AIAA Journal, **34**(5) pp. 1013-1018. DOI:10.2514/3.13181.

[107] International Organization for Standardization (ISO), Guide to the Expression of Uncertainty in Measurement, ISO, Geneva, 1993. Corrected and reprinted, 1995.

[108] Hudson, S. T., Bordelon Jr., W. J., and Coleman, H. W., 1996. "Effect of Correlated Precision Errors on Uncertainty of a Subsonic Venturi Calibration." AIAA Journal, **34**(9) pp. 1862-1867. DOI:10.2514/3.13319.

Appendix A – Experimental Setup

Picture and Schematic of electrical interface DAQ System

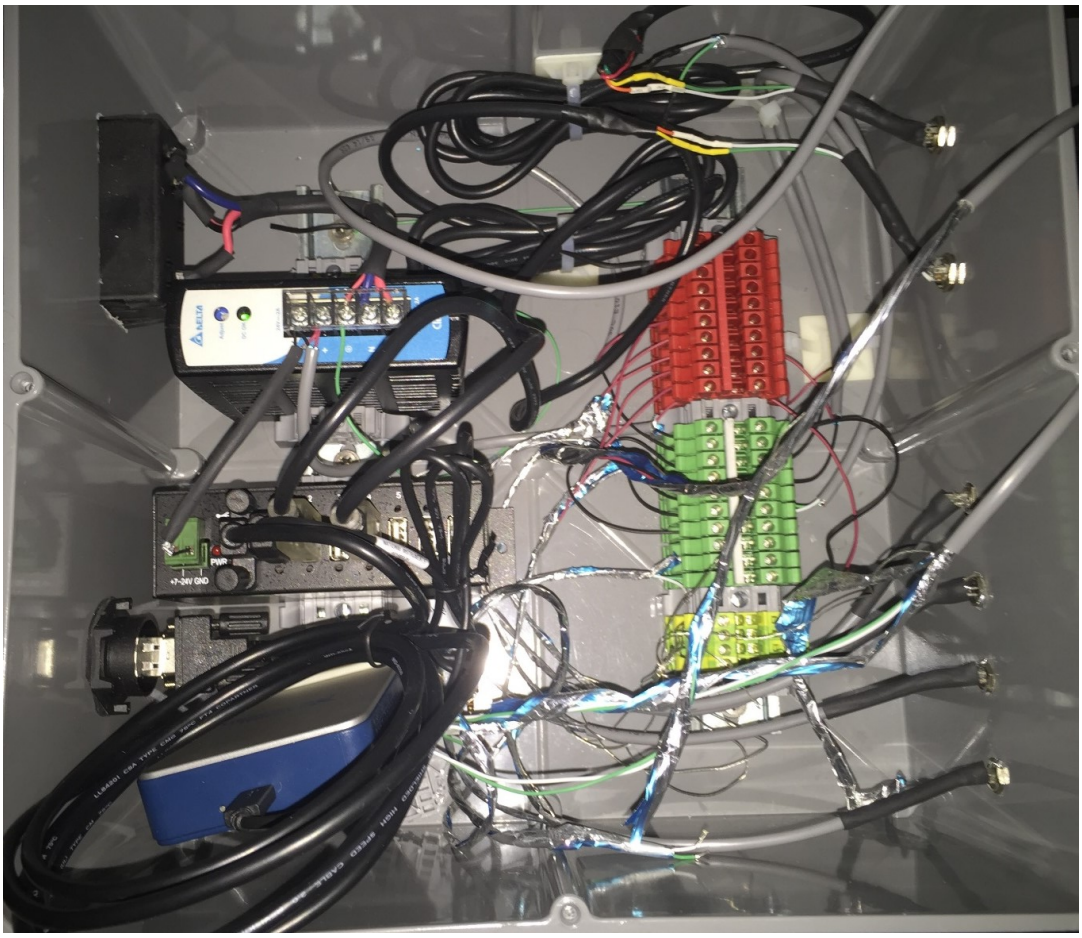

Figure 31 — Picture of electrical interface DAQ system

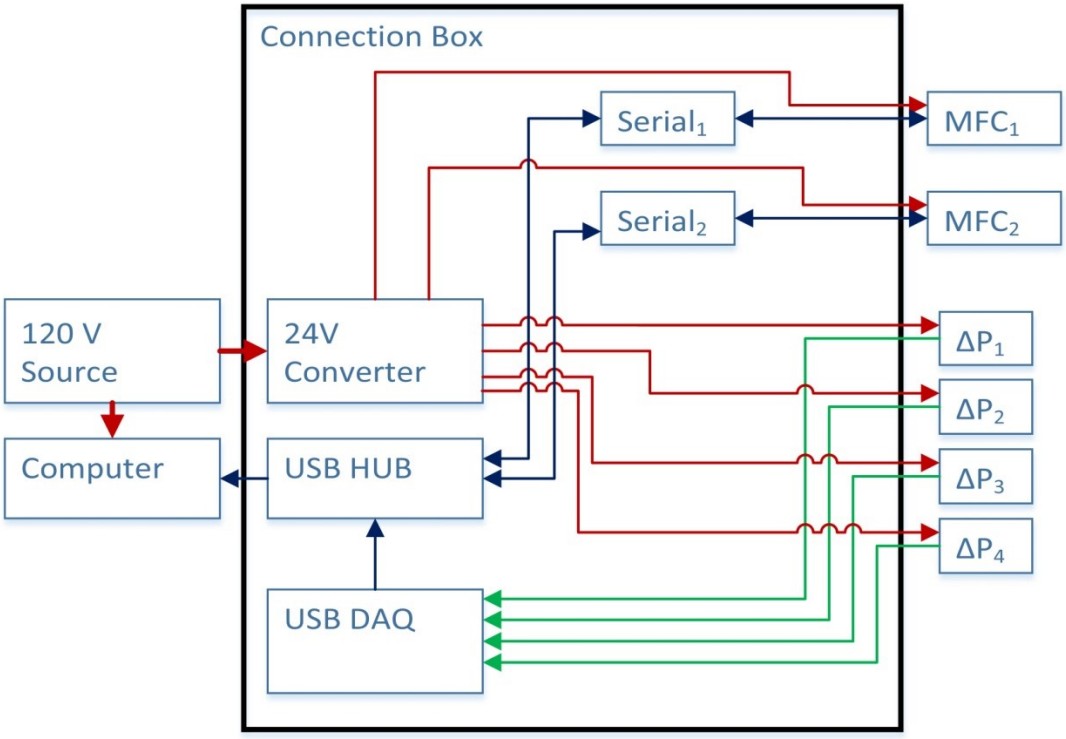

Figure 32 — Schematic of electrical interface DAQ system

Table 8 — Inner Diameter Measurements (all measurements in inches)

	1/4" Annuflex	1/4" Masterflex	3/8" Annuflex	3/8" Masterflex	1/2" Annuflex	1/2" Masterflex	3/4" Annuflex	3/4" Masterflex	1/4" Titeflex	3/8" Titeflex
	0.2725	0.2620	0.4215	0.4170	0.5395	0.5290	0.7925	0.7695	0.2440	0.3460
	0.2735	0.2620	0.4200	0.4125	0.5355	0.5285	0.7940	0.7705	0.2430	0.3510
	0.2750	0.2600	0.4220	0.4145	0.5365	0.5275	0.7965	0.7670	0.2435	0.3515
	0.2725	0.2575	0.4185	0.4140	0.5380	0.5275	0.7825	0.7705	0.2425	0.3535
	0.2740	0.2615	0.4205	0.4130	0.5395	0.5260	0.7785	0.7755	0.2420	0.3520
Port 1	0.2705	0.2570	0.4200	0.4135	0.5340	0.5285	0.7770	0.7690	0.2425	0.3495
	0.2740	0.2640	0.4210	0.4175	0.5385	0.5255	0.7865	0.7770	0.2430	0.3525
	0.2735	0.2615	0.4205	0.4125	0.5395	0.5225	0.7980	0.7695	0.2420	0.3510
	0.2720	0.2620	0.4195	0.4140	0.5335	0.5235	0.7910	0.7780	0.2425	0.3485
	0.2710	0.2580	0.4225	0.4170	0.5390	0.5235	0.7870	0.7720	0.2430	0.3475
	0.2735	0.2605	0.4215	0.4120	0.5365	0.5235	0.7880	0.7815	0.2435	0.3530
Port 2	0.2730	0.2565	0.4210	0.4135	0.5365	0.5245	0.7850	0.7745	0.2430	0.3515
	0.2730	0.2645	0.4195	0.4170	0.5375	0.5235	0.7875	0.7800	0.2435	0.3450
	0.2745	0.2635	0.4205	0.4140	0.5390	0.5235	0.7885	0.7810	0.2430	0.3495
	0.2720	0.2635	0.4195	0.4140	0.5365	0.5230	0.7990	0.7775	0.2425	0.3535
	0.2735	0.2590	0.4225	0.4140	0.5380	0.5240	0.7840	0.7745	0.2440	0.3480
	0.2720	0.2635	0.4215	0.4145	0.5395	0.5225	0.7900	0.7675	0.2445	0.3520
Port 2*	0.2725	0.2585	0.4210	0.4145	0.5340	0.5245	0.7835	0.7695	0.2425	0.3470
	0.2730	0.2645	0.4205	0.4145	0.5375	0.5270	0.7865	0.7735	0.2435	0.3505
	0.2740	0.2635	0.4210	0.4150	0.5425	0.5280	0.7900	0.7725	0.2440	0.3435
	0.2730	0.2640	0.4195	0.4155	0.5350	0.5275	0.7955	0.7695	0.2435	0.3485
Port 3	0.2715	0.2580	0.4190	0.4155	0.5370	0.5265	0.7820	0.7860	0.2435	0.3475

	0.2720	0.2635	0.4200	0.4105	0.5380	0.5275	0.7835	0.7720	0.2445	0.3435
	0.2720	0.2580	0.4205	0.4125	0.5370	0.5275	0.7855	0.7815	0.2430	0.3475
	0.2720	0.2625	0.4195	0.4135	0.5355	0.5225	0.7775	0.7695	0.2425	0.3520
	0.2725	0.2645	0.4205	0.4130	0.5385	0.5235	0.7885	0.7725	0.2425	0.3510
	0.2700	0.2615	0.4185	0.4165	0.5360	0.5245	0.7785	0.7635	0.2410	0.3460
	0.2730	0.2640	0.4210	0.4130	0.5390	0.5240	0.7875	0.7715	0.2420	0.3495
	0.2750	0.2620	0.4205	0.4140	0.5385	0.5240	0.7880	0.7730	0.2435	0.3525
Port 8	0.2730	0.2580	0.4225	0.4170	0.5340	0.5250	0.7955	0.7740	0.2420	0.3450
	0.2740	0.2590	0.4190	0.4175	0.5365	0.5235	0.7825	0.7780	0.2445	0.3500
	0.2715	0.2580	0.4215	0.4180	0.5395	0.5245	0.7805	0.7695	0.2415	0.3525
	0.2720	0.2590	0.4215	0.4165	0.5350	0.5235	0.7865	0.7755	0.2440	0.3510
	0.2720	0.2580	0.4195	0.4145	0.5375	0.5235	0.7885	0.7780	0.2430	0.3450
	0.2715	0.2615	0.4215	0.4140	0.5400	0.5230	0.7835	0.7700	0.2435	0.3540
Port 9	0.2730	0.2610	0.4195	0.4155	0.5365	0.5240	0.7840	0.7730	0.2425	0.3500
Avg.	0.2727	0.2610	0.4205	0.4146	0.5373	0.5250	0.7870	0.7735	0.2430	0.3495
Std. Dev.	0.0012	0.0025	0.0011	0.0018	0.0020	0.0020	0.0057	0.0048	0.0008	0.0030

Distances between Pressure Ports

Table 9 — Distances between pressure taps (all measurements in inches)

Line Name	P1 to P2	P1 to P3	P1 to P4	P1 to P5	P1 to P6	P1 to P7	P1 to P8	P1 to P9	P1 to P10
0.25” Annuflex #3	12 3/4	25 5/16	37 15/16	50 5/8	63 5/16	75 15/16	88 5/8	101 1/4	113 15/16
0.25” Masterflex #4	11 7/8	23 13/16	35 13/16	47 3/4	59 3/4	71 11/16	83 11/16	95 5/8	107 5/8
0.375” Annuflex #7	12 7/8	25 3/4	38 5/8	51 3/8	64 3/4	77 1/8	89 7/8	102 3/4	115 5/8
0.375” Masterflex #8	12 5/8	25 5/16	37 15/16	51 9/16	63 3/16	75 3/4	88 7/16	101 1/16	113 11/16
0.50” Annuflex #11	12 11/16	25 5/16	37 15/16	50 9/16	63 3/16	75 13/16	88 7/8	101	113 5/8
0.50” Masterflex #12	12 5/8	25 1/4	38	50 3/4	63 3/8	76	88 3/4	101 7/16	114 1/8
0.75” Annuflex #15	12 11/16	25 5/16	37 7/8	50 9/16	63 1/4	75 7/8	88 1/2	101 1/8	113 13/16
0.75” Masterflex #16	12 5/8	25 1/8	37 9/16	50	62 9/16	75	87 1/2	100 1/16	112 5/8
0.25” Titeflex #17	12 9/16	25 1/32	37 9/16	50 1/8	62 23/32	75 9/32	87 7/8	100 1/2	113 1/8
0.375” Titeflex #18	12 5/8	25 1/4	37 7/8	50 1/2	63 1/4	75 7/8	88 3/8	101 1/16	113 3/4
0.625” EMT #19	12	24	36	48	60	72	84	95 15/16	N/A
0.825” EMT #20	12	24	36	48	60	72	84	96	N/A

Port Manifold Detail Examples

Figure 33 — Picture of port manifold system to direct static ports to differential pressure transducer

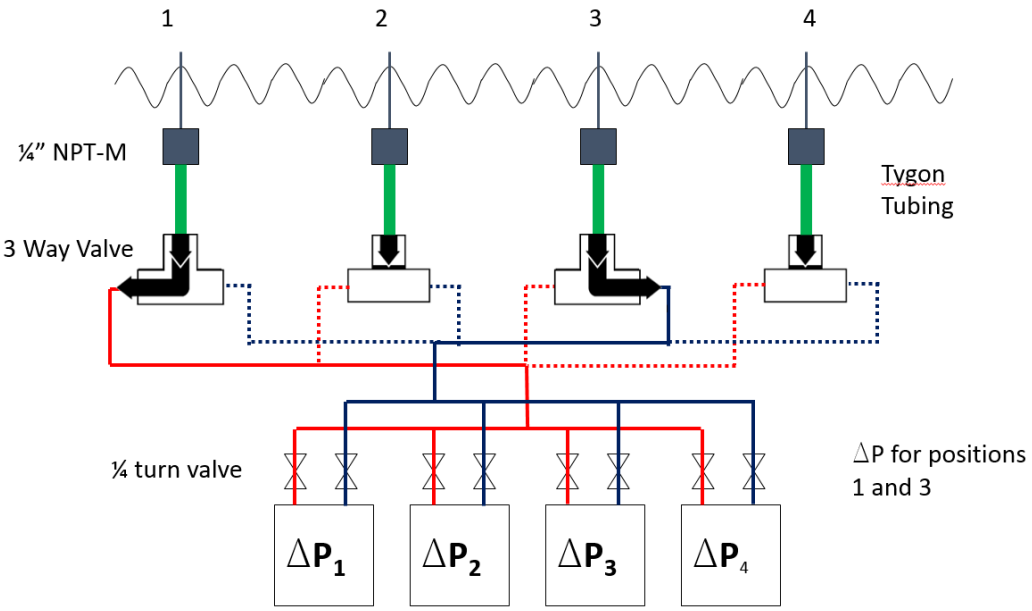

Figure 34 — Example 1: Using three-way valves to select Port 1 as high pressure and Port 3 as low pressure

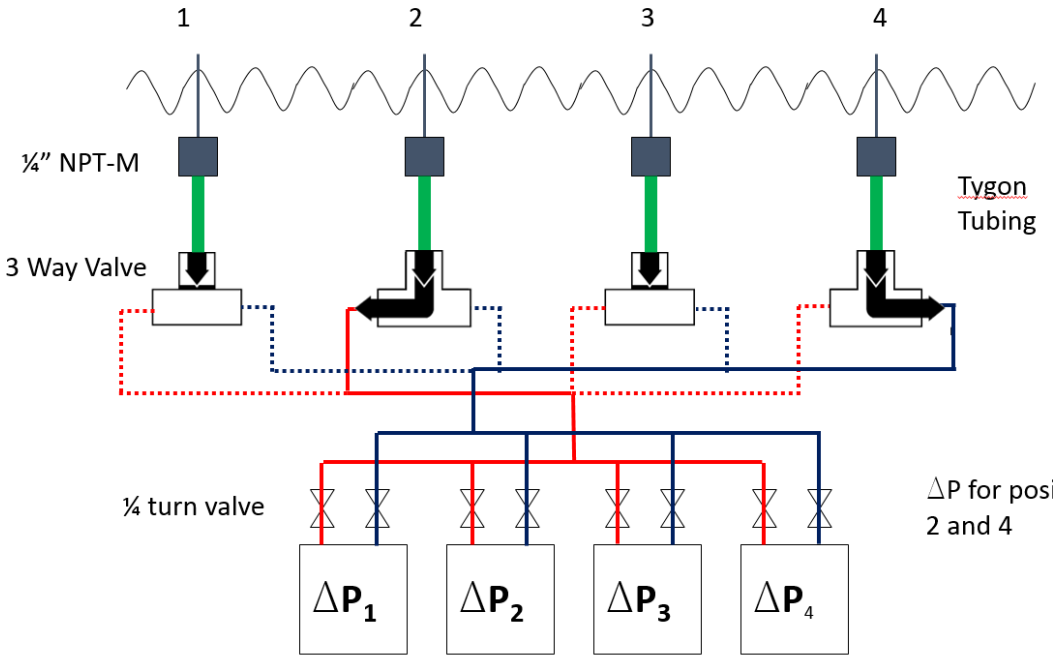

Figure 35 — Example 2: Using three-way valves to select Port 2 as high pressure and Port 4 as low pressure

Figure 36 — Picture of automated valve switching system

Appendix B – Uncertainty Analysis

Introduction

Uncertainty analysis provides a confidence interval associated with a measurement. This interval is representative of the distribution of measurements in relation to the true value of a measurement. Uncertainty can be reported as a percentage of the mean measurement (12 inches +/- 0.52%) or a bias range (i.e., 12 inches +/- 0.0625 inches) and can be converted between the two. For example, by taking the mean measured value and dividing by the bias range to obtain the percentage of the mean measurement, namely 0.52% = (12 inches / 0.0625 inches). The percentage of the mean measurement is easier to read and understand the scale of the uncertainty of the measurement (especially when comparing the magnitude of different uncertainties) while the bias range is used in the calculations and propagation of individual fixed bias errors into data reduction equations.

Using methodology described by Coleman and Steele [88], a 95% confidence interval was used to determine the uncertainty for all measurements and data reduction equations presented. Equation (17)

quantifies the general uncertainty of any result, r, where B_x are the individual systematic errors (SSU) and P_x are the random error (RSU) effects.

$$\left(\frac{U_r}{r}\right)^2 = \sum_{i=1}^{J}\left\{\left(\frac{\partial r}{\partial X_i}\right)^2 B_i^2\right\} + 2\sum_{i=1}^{J-1}\sum_{k=i+1}^{J}\left\{\left(\frac{\partial r}{\partial X_i}\right)\left(\frac{\partial r}{\partial X_k}\right)[B_i B_k]_{correlated}\right\} + \sum_{i=1}^{J}\left\{\left(\frac{\partial r}{\partial X_i}\right)^2 P_i^2\right\} + 2\sum_{i=1}^{J-1}\sum_{k=i+1}^{J}\left\{\left(\frac{\partial r}{\partial X_i}\right)\left(\frac{\partial r}{\partial X_k}\right)[P_i P_k]_{correlated}\right\} \quad (17)$$

An example of a governing equation (18) determines the average differential pressure per unit length of a given pipe where n is the number different port lengths tested, ΔP_n is the differential pressure measurement and Δd_n is the length measurement between port locations. This averaged result is then used to calculate the friction factor of a corrugated pipe.

$$r_1 \stackrel{\text{def}}{=} \left(\frac{\Delta P}{L}\right)_{Avg} = \frac{1}{N}\sum_{n=1}^{N}\left(\frac{\Delta P_n}{d_n}\right) \quad (18)$$

$$r_2 \stackrel{\text{def}}{=} f = \left(\frac{\Delta P}{L}\right)_{Avg}\frac{\rho\pi^2 D^5}{8\dot{m}^2} \quad (19)$$

$$r_3 \stackrel{\text{def}}{=} Re = \frac{4\dot{m}}{\pi D\mu} \quad (20)$$

Elemental Bias Sources

From ISO guide and book [Eq. 5.16] to the expression of Uncertainty and Measurements [107], u_X is found from the combination of all the standard elemental uncertainties as described in equation (21):

$$(u_X)^2 = (u_1)^2 + (u_2)^2 + (u_3)^2 + (u_4)^2 + (u_5)^2 \quad (21)$$

Examples of systematic uncertainty include calibration, data acquisition, data reduction and conceptual errors. The systematic uncertainty of the independent variables (diameter, differential pressure, distance between static ports, dynamic viscosity, and mass flow rate) described below:

Inner Diameter

An email correspondence provided the minimum and maximum tolerances for the inner diameter of the corrugated pipes outlined in Table 10 and an example of how to convert the systematic standard uncertainty as a percentage of the mean with equation (22):

$$SSU_{ID} = \frac{Tolerance_{ID}}{Mean_{ID}} * 100\% \quad (22)$$

Table 10 — Inner Diameter Systematic Standard Uncertainty (SSU)

Pipe	ID (mm)	ID (in)	ID Tolerance (in)	ID SSU
Annuflex				
6.35 (¼")	6.883	0.271	0.007	2.58%
9.53 (3/8")	10.668	0.420	0.01	2.38%
12.70 (½")	13.538	0.533	0.01	1.88%
19.05 (¾")	19.888	0.783	0.01	1.28%
Masterflex				
6.35 (¼")	6.604	0.26	0.007	2.69%
9.53 (3/8")	10.643	0.419	0.01	2.39%
12.70 (½")	13.462	0.53	0.01	1.89%
19.05 (¾")	19.634	0.773	0.01	1.29%
Titeflex[10]				
6.35 (¼")	5.842	0.23	0.007	3.04%
9.53 (3/8")	8.636	0.34	0.01	2.94%

Differential Pressure Transducers

Table 11 — Differential Pressure Transducers

Differential Pressure Transducer	Scale Factor (in. H_2O/V)	Linearity (% of full scale)	Range (in. H_2O)	Voltage Output (V)
PX654-0.05BD5V	0.025	0.3%	+/- 0.05	1-5
PX654-0.5D5V	0.125	0.3%	0-0.5	1-5
PX654-5D5V	1.125	0.3%	0-5	1-5
PX653-50D5V	12.5	0.3%	0-50	1-5
PX656-200DI	50	0.3%	0-200	1-5

[10] ID values taken from catalog and ID tolerances assumed to be the same even with a different manufacturer

The overall bias ($b_{\Delta P_n}$) associated with measuring differential pressure using equation (21) with elemental sources from the pressure transducer itself, data acquisition and installation effects (assuming 1% for each of the following: angle misalignment, depth of needle in flow, swaying of needle during testing). First, the systematic standard uncertainty associated with only the pressure transducer is shown in Figure 37. Note: The spiking nature of the uncertainty represents the different ranges of the individual pressure transducers – the discontinuity happens between the sensors.

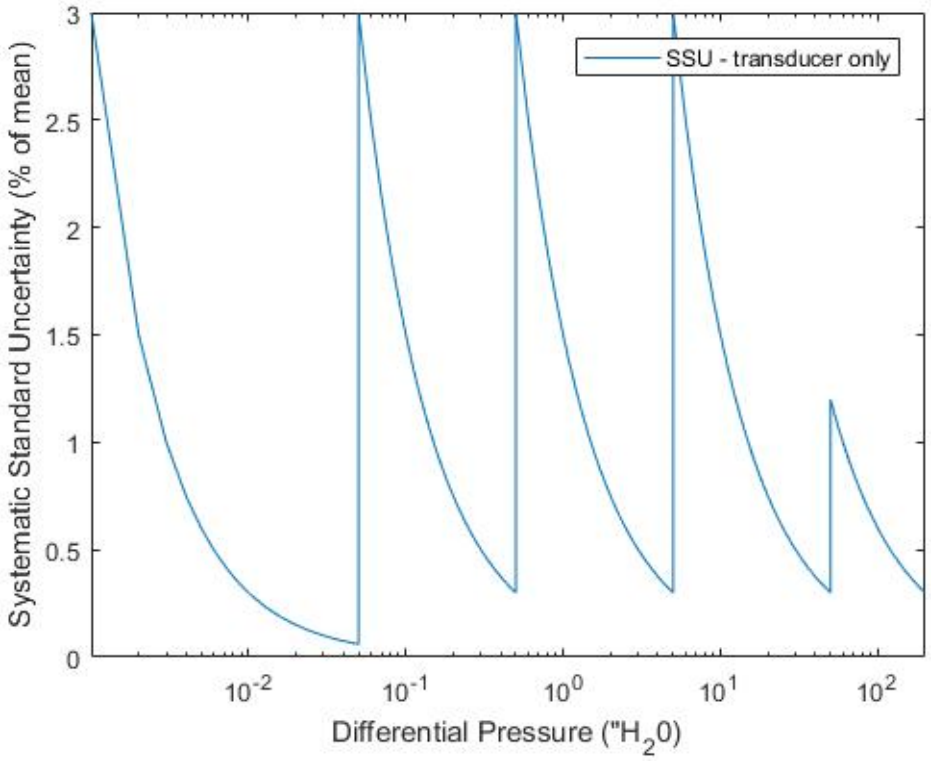

Figure 37 — Systematic Standard Uncertainty for the Differential Pressure Transducers over the measuring range

Second, the bias associated with the Data Acquisition System (16-bit resolution, -10 V to 10 V analog inputs) yields a bias of 20 V / 2^16 = 0.000305 V. The systematic standard uncertainty associated with only the DAQ is shown in Figure 38. Note: Similar to the previous plot, the spiking nature of the uncertainty represents the different ranges of the individual pressure transducers – the discontinuity happens between the sensors.

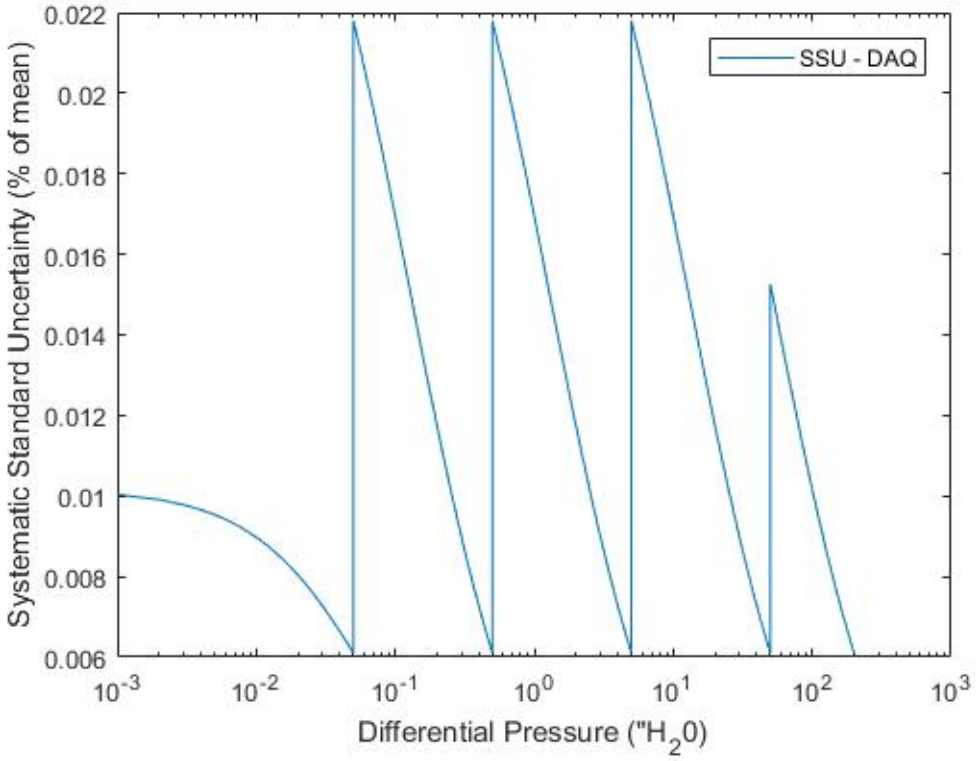

Figure 38 — Systematic Standard Uncertainty for the DAQ of the Differential Pressure Transducers over the measuring range

Finally, the installation effects were considered. The pressure transducer installation bias was estimated by needle angle with respect to nominal axial flow direction. Assuming 2° misalignment, due to either non-vertical installation or due to non-straightness of the needles themselves, for both needles at location n and m, as well as any potential movement of the needles due to flow resonance or vortices, the relative bias of these combined effects was estimated as 1%. Combination of elemental sources by (21),

yielding a maximum worst case relative bias for the differential pressure readings of 0.03162 or 3.162%. The total systematic standard uncertainty over the measurement range is shown in Figure 39.

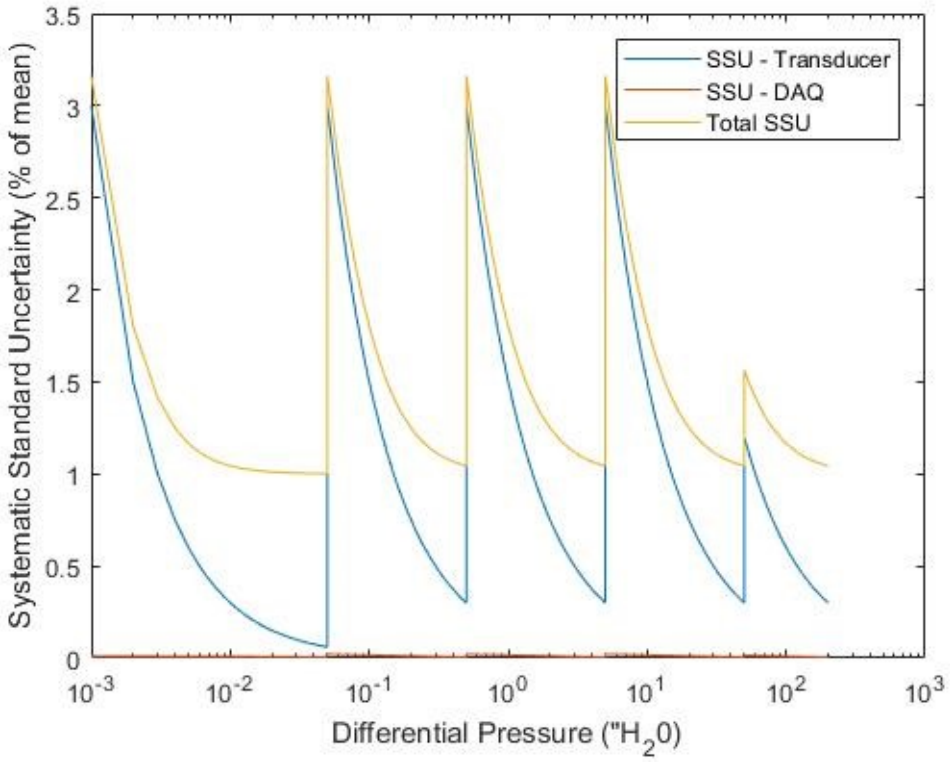

Figure 39 — Combined Systematic Standard Uncertainty for the Differential Pressure Transducers over the range

Distance between Static Pressure Ports

The bias associated with distance between the holes used for the installation of the static pressure port needles (b_{d_n}) include the 1/16" bias of

the tape measure used to verify distance between the ports, as well as the biases associated with installation.

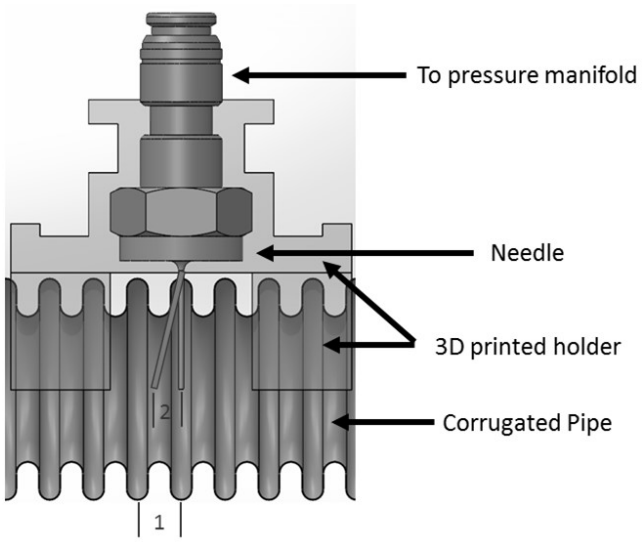

Figure 40 — Cross sectional CAD for the static pressure port holder with exaggerated outline of the needle in a bent configuration

The following distance installation error effects were considered and estimated (see Figure 40):

1. Linear needle offset: a potential installation error associated with locating the needles on the incorrect corrugation peak. This error is taken as identically zero because needle holes were verified to be located on the properly identified corrugation peak.
2. Linear needle offset due to needle installation angle: Assuming 10° installation angle offset from vertical, with a needle length of 15.24 mm (0.6”) would yield a bias of 2.67 mm (0.105”).

3. Needle straightness. Assuming the pipe contains two arc-lengths with a maximum centerline deviation of 6.35 mm (0.25”) over a 317.5 mm (12.5”) span, would yield a bias of (arc-length – original length) = 318.85 mm – 317.5 mm (12.553”-12.5”) = 1.35 mm (0.053”).
4. Needle concentricity with corresponding installation hole: the hole size was drilled to 1.19 mm (3/64”, 0.046875”) while the needle OD is 0.711 mm (0.028”). The range would then be: 1.19 mm-0.711 mm = 0.0479 mm (0.046875”- 0.028” = 0.019”) or 0.00 mm ± 0.241 mm (0.000” ±0.0095”). The smallest distance being 304.8 mm (12.000”) in between holes would give a biased of 0.241 mm*2 holes = 0.482 mm (0.0095” *2 holes = 0.019”).

The biased associated with installation effects would yield an installation bias of 3.03 mm (0.1191”) and the total systematic standard uncertainty associated with the distance between pressure ports is b_{d_n} = 3.13 mm (0.1232”).

This bias was used for all distance combinations between needles, however the larger the distance between the needles there less error. For example, a differential pressure measurement between two needles will comprise of the static pressure and dynamic pressure. This dynamic pressure term is an error induced through the angle of the needles not being perfectly

perpendicular to the stream. The relative amount of influence of this error term to the overall reading decreases with increasing distance between the needles. The authors used data associated with the largest needle separation distances to determine friction loss factors to reduce this bias.

Dynamic Viscosity

The systematic standard uncertainty associated with the dynamic viscosity was assumed to be 1.5%. A conservative estimate was accounted for by approximating the minimum and maximum range that the dynamic viscosity over the range of environmental temperatures and pressures.

Mass Flow Rate

Both mass flow controllers (MC20 and MCH100) had an elemental bias of ±0.8% of reading +0.2% of full scale. This results in a systematic standard uncertainty over the control range as follows:

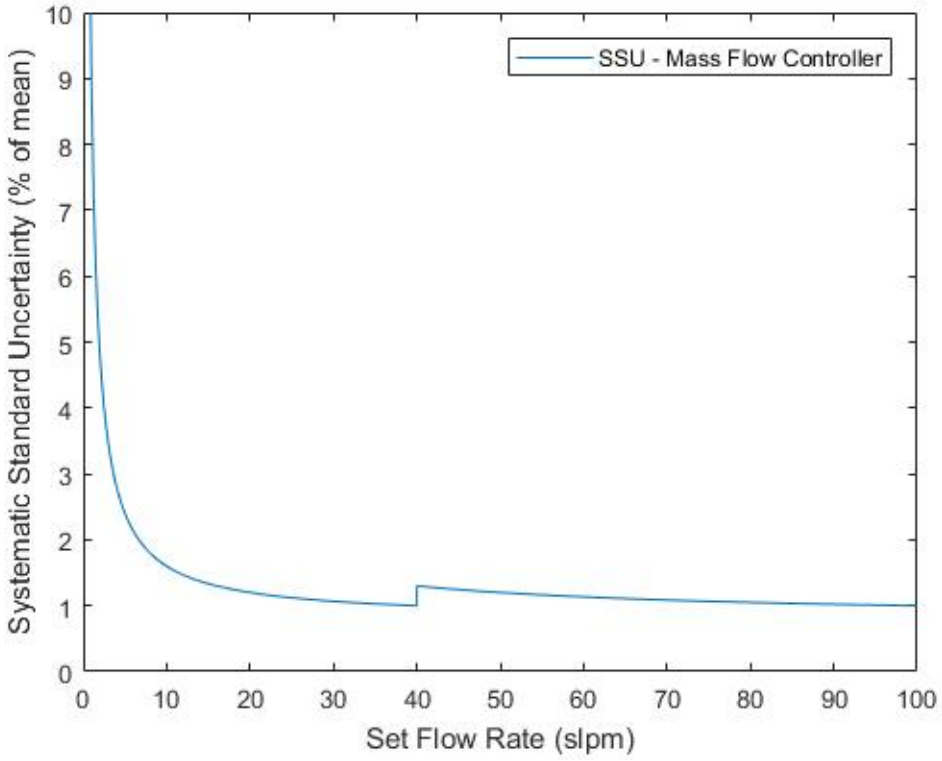

Figure 41 — Systematic Standard Uncertainty for the Mass Flow Rate Controllers over their range

Systematic Correlated Bias

Systematic correlated bias, as in Hudson [108], appears when several measurements are taken with the same instrument, or several instruments calibrated with respect to the same standard. An example provided by Brown [106] is when multiple pressures are sequentially ported (rake) to the same transducer as its traversed across a flow field. For these studies, only the first

result (r_1) included systematic correlated bias (the rest of the correlated bias terms were assumed to be zero). For the first result, assume that the following pairs of bias terms are perfectly correlated: $\Delta P_n \; with \; all \; other \; \Delta P_n$ when the same differential pressure transducer is used for reading the measurement and all $d_n's$ with all other $d_n's$. The other terms are not assumed to not be correlated ($\Delta P_n \; wrt. \; d_n's$).

Using Coleman and Steele [88], Eq. 5.17, p. 145, the number of elemental error sources that are common is one for both delta pressure measurement and distance measured the correlated bias error for differential pressure is given by equation (23) and for distance by equation (24).

$$b^2_{\Delta P_n \Delta P_m} = \left(b_{\Delta P_n}\right)\left(b_{\Delta P_m}\right) \tag{23}$$

$$b^2_{d_n d_m} = \left(b_{d_n}\right)\left(b_{d_m}\right) \tag{24}$$

Note that the above can (and should) be completed during the planning phase of an experimental set up to possibly identify major sources or contributors to the systematic uncertainty.

Since the systematic standard uncertainty associated with the distance measurement is so low, the correlated bias effects associated with the distances are also negligible. Alternatively, the pressure transducer correlated bias errors approximately accounted for 50% of the overall bias in result 1.

Random Standard Uncertainty (RSU)

The random standard uncertainty associated with a particular confidence level can be determined using a coverage factor. If enough samples are taken, the central limit theorem shows that the error distribution of a measurement will approach a Gaussian distribution. This allows one to use the t-distribution for a lower number of samples (or degrees of freedom) in determining the factor to multiply the combined standard uncertainty by determining the overall uncertainty of a result. For most engineering applications, the large-sample approximation is used and for a 95% confidence interval, the factor is 2*standard deviation of measurements collected.

For the data collected, the quantity of mass flow rate measurements averaged around 30 samples (degrees of freedom) per run and the t-distribution was programmed and used while the quantity of differential pressure measurements (roughly 300 per sample) allowed for the large-sample approximation to be used. The random standard uncertainty for inner diameter, distance between ports, dynamic viscosity was all assumed to be zero. For the average differential pressure per length, the degrees of freedom varied from 3-9 depending on the data analysis and if there was an error associated with a particular needle.

Expanded Uncertainty (EU) (Revised Bias Equation)

The overall expanded uncertainty is given by:

$$\left(\frac{U_{\left(\frac{\Delta P}{L}\right)_{Avg}}}{\left(\frac{\Delta P}{L}\right)_{Avg}}\right)^2 = \left(\frac{1}{N}\right)^2\left[\sum_{j=1}^{N}\left[\left(\frac{b_{\Delta P_n}^2}{d_n^2}\right)\right] + \sum_{j=1}^{N}\left[\left(\frac{\Delta P_n}{(d_n)^2}\right)^2 b_{d_n}^2\right] + 2\sum_{j=1}^{n}\sum_{k\neq j}\left[\left(\frac{1}{d_n}\right)\left(\frac{1}{d_m}\right) b_{\Delta P_n \Delta P_m}^2\right] + 2\sum_{j=1}^{N}\left[\left(\frac{\Delta P_n}{(d_n)^2}\right)\left(\frac{\Delta P_m}{(d_m)^2}\right) b_{d_n d_m}^2\right] + \sum_{j=1}^{N}\left[\left(\frac{P_{\Delta P_n}^2}{d_n^2}\right)\right]\right] \quad (25)$$

$$(U_{Re})^2 = \left[\left(\frac{\partial Re}{\partial \dot{m}}\right)^2 B_{\dot{m}}^2 + \left(\frac{\partial Re}{\partial D}\right)^2 B_{\mathrm{D}}^2 + \left(\frac{\partial Re}{\partial \mu}\right)^2 B_{\mu}^2 + 2\sum_{i=1}^{J-1}\sum_{k=i+1}^{J}\left\{\left(\frac{\partial r}{\partial X_i}\right)\left(\frac{\partial r}{\partial X_k}\right)[B_i B_k]_{correlated}\right\} + \left(\frac{\partial Re}{\partial \dot{m}}\right)^2 P_{\dot{m}}^2 + \left(\frac{\partial Re}{\partial D}\right)^2 P_{\mathrm{D}}^2 + \left(\frac{\partial Re}{\partial \mu}\right)^2 P_{\mu}^2 + 2\sum_{i=1}^{J-1}\sum_{k=i+1}^{J}\left\{\left(\frac{\partial r}{\partial X_i}\right)\left(\frac{\partial r}{\partial X_k}\right)[P_i P_k]_{correlated}\right\}\right] \quad (26)$$

where:

$$\frac{\partial Re}{\partial \dot{m}} = \frac{4}{\pi D \mu}$$

$$\frac{\partial Re}{\partial D} = \frac{-4\dot{m}}{\pi D^2 \mu} \tag{27}$$

$$\frac{\partial Re}{\partial \mu} = \frac{-4\dot{m}}{\pi D \mu^2}$$

$$\begin{aligned}\left(\frac{U_{Re}}{Re}\right)^2 = \Bigg[& \left(\frac{B_{\dot{m}}}{\dot{m}}\right)^2 + \left(-\frac{B_D}{D}\right)^2 + \left(-\frac{B_\mu}{\mu}\right)^2 - 2\frac{[B_{\dot{m}} B_D]_{corr}}{\dot{m} * D} \\ & - 2\frac{\left[B_{\dot{m}} B_\mu\right]_{corr}}{\dot{m} * \mu} + 2\frac{\left[B_{\mathrm{D}} B_\mu\right]_{corr}}{\mathrm{D} * \mu} + \left(\frac{P_{\dot{m}}}{\dot{m}}\right)^2 + \left(-\frac{P_D}{D}\right)^2 \\ & + \left(-\frac{P_\mu}{\mu}\right)^2 - 2\frac{[P_{\dot{m}} P_D]_{corr}}{\dot{m} * D} - 2\frac{\left[P_{\dot{m}} P_\mu\right]_{corr}}{\dot{m} * \mu} \\ & + 2\frac{\left[P_{\mathrm{D}} P_\mu\right]_{corr}}{\mathrm{D} * \mu}\Bigg]\end{aligned} \tag{28}$$

$$
\begin{aligned}
\left(U_f\right)^2 = \Bigg[& \left(\frac{\partial f}{\partial \Delta P}\right)^2 B_{\Delta P}^2 + \left(\frac{\partial f}{\partial \mathrm{L}}\right)^2 B_{\mathrm{L}}^2 + \left(\frac{\partial f}{\partial \rho}\right)^2 B_{\rho}^2 + \left(\frac{\partial f}{\partial \mathrm{D}}\right)^2 B_{D}^2 \\
& + \left(\frac{\partial f}{\partial \dot{m}}\right)^2 B_{\dot{m}}^2 \\
& + 2 \sum_{i=1}^{J-1} \sum_{k=i+1}^{J} \left\{ \left(\frac{\partial r}{\partial X_i}\right) \left(\frac{\partial r}{\partial X_k}\right) [B_i B_k]_{correlated} \right\} \\
& + \left(\frac{\partial f}{\partial \Delta P}\right)^2 P_{\Delta P}^2 + \left(\frac{\partial f}{\partial \mathrm{L}}\right)^2 P_{\mathrm{L}}^2 + \left(\frac{\partial f}{\partial \rho}\right)^2 P_{\rho}^2 + \left(\frac{\partial f}{\partial \mathrm{D}}\right)^2 P_{D}^2 \\
& + \left(\frac{\partial f}{\partial \dot{m}}\right)^2 P_{\dot{m}}^2 \\
& + 2 \sum_{i=1}^{J-1} \sum_{k=i+1}^{J} \left\{ \left(\frac{\partial r}{\partial X_i}\right) \left(\frac{\partial r}{\partial X_k}\right) [P_i P_k]_{correlated} \right\} \Bigg]
\end{aligned}
\tag{29}
$$

where:

$$
\begin{aligned}
\left(\frac{\partial f}{\partial \Delta P}\right) &= \frac{\pi^2 \rho D^5}{8 \mathrm{L} \dot{m}^2} \\
\left(\frac{\partial f}{\partial \mathrm{L}}\right) &= -\frac{\pi^2 \Delta P \rho D^5}{8 L^2 \dot{m}^2} \\
\left(\frac{\partial f}{\partial \rho}\right) &= \frac{\pi^2 \Delta P D^5}{8 \mathrm{L} \dot{m}^2} \\
\left(\frac{\partial f}{\partial \mathrm{D}}\right) &= \frac{\pi^2 5 \Delta P \rho D^4}{8 L \dot{m}^2}
\end{aligned}
\tag{30}
$$

$$\left(\frac{\partial f}{\partial \dot{m}}\right) = -\frac{\pi^2 \Delta P \rho D^5}{4 L \dot{m}^3}$$

$$\begin{aligned}\left(\frac{U_f}{f_{Avg}}\right)^2 = \Bigg[& \left(\frac{B_{\Delta P}}{\Delta P}\right)^2 + \left(-\frac{B_L}{L}\right)^2 + \left(\frac{B_\rho}{\rho}\right)^2 + \left(5\frac{B_D}{D}\right)^2 + \left(-\frac{B_{\dot{m}}}{\dot{m}}\right)^2 \\ & - 2\frac{[B_{\Delta P} B_L]_{corr}}{\Delta P * L} + 2\frac{\left[B_{\Delta P} B_\rho\right]_{corr}}{\Delta P * \rho} + 2 \\ & * 5\frac{[B_{\Delta P} B_D]_{corr}}{\Delta P * D} - 2\frac{[B_{\Delta P} B_{\dot{m}}]_{corr}}{\Delta P * \dot{m}} - 2\frac{\left[B_L B_\rho\right]_{corr}}{L * \rho} + 2 \\ & * 5\frac{[B_L B_D]_{corr}}{L * D} + 2\frac{[B_L B_{\dot{m}}]_{corr}}{L * \dot{m}} + 2 * 5\frac{\left[B_\rho B_D\right]_{corr}}{\rho * D} \\ & - 2\frac{\left[B_\rho B_{\dot{m}}\right]_{corr}}{\rho * \dot{m}} - 2 * 5\frac{[B_D B_{\dot{m}}]_{corr}}{D * \dot{m}} + \left(\frac{P_{\Delta P}}{\Delta P}\right)^2 \\ & + \left(-\frac{P_L}{L}\right)^2 + \left(\frac{P_\rho}{\rho}\right)^2 + \left(5\frac{P_D}{D}\right)^2 + \left(-\frac{P_{\dot{m}}}{\dot{m}}\right)^2 \\ & - 2\frac{[P_{\Delta P} P_L]_{corr}}{\Delta P * L} + 2\frac{\left[P_{\Delta P} P_\rho\right]_{corr}}{\Delta P * \rho} + 2 * 5\frac{[P_{\Delta P} P_D]_{corr}}{\Delta P * D} \\ & - 2\frac{[P_{\Delta P} P_{\dot{m}}]_{corr}}{\Delta P * \dot{m}} - 2\frac{\left[P_L P_\rho\right]_{corr}}{L * \rho} + 2 * 5\frac{[P_L P_D]_{corr}}{L * D} \\ & + 2\frac{[P_L P_{\dot{m}}]_{corr}}{L * \dot{m}} + 2 * 5\frac{\left[P_\rho P_D\right]_{corr}}{\rho * D} - 2\frac{\left[P_\rho P_{\dot{m}}\right]_{corr}}{\rho * \dot{m}} \\ & - 2 * 5\frac{[P_D P_{\dot{m}}]_{corr}}{D * \dot{m}} \Bigg]\end{aligned} \tag{31}$$

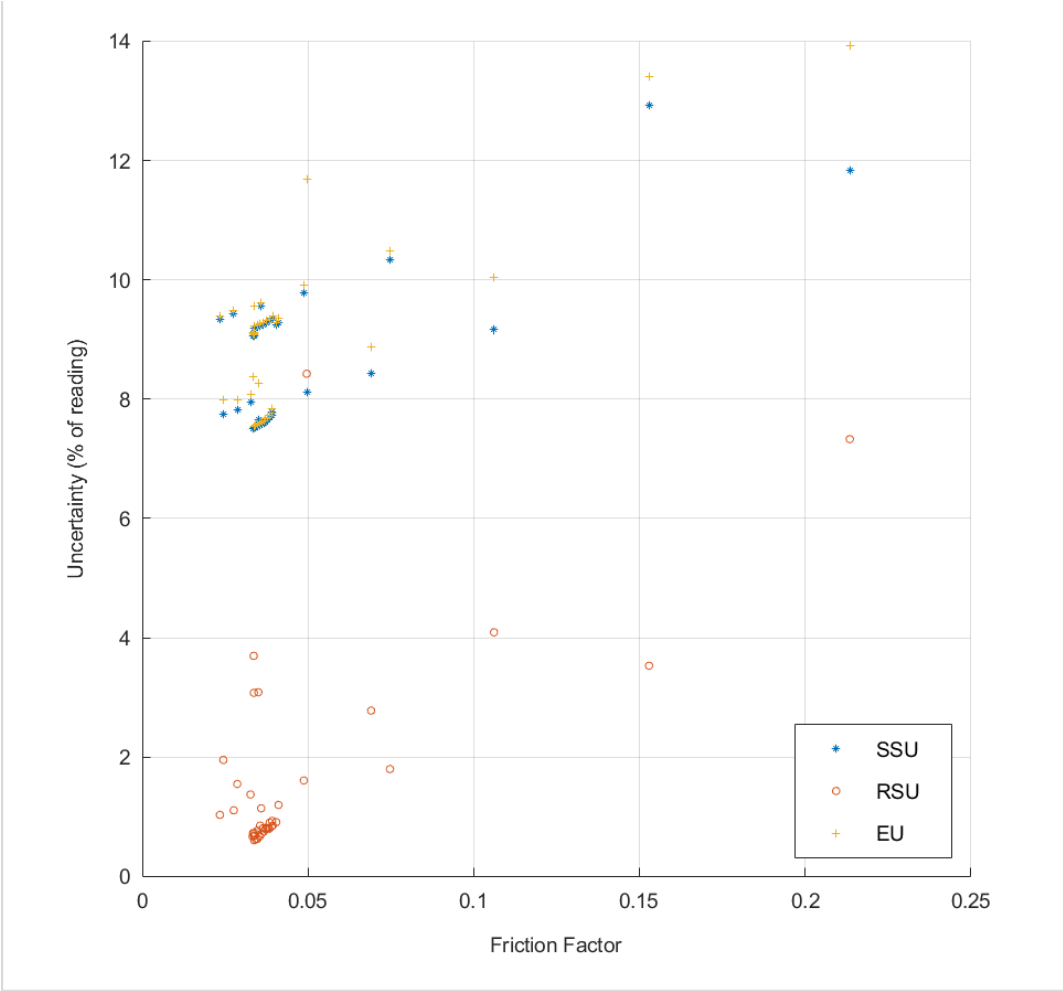

Figure 42 — Plot of expanded uncertainty of friction factor for smooth EMT lines

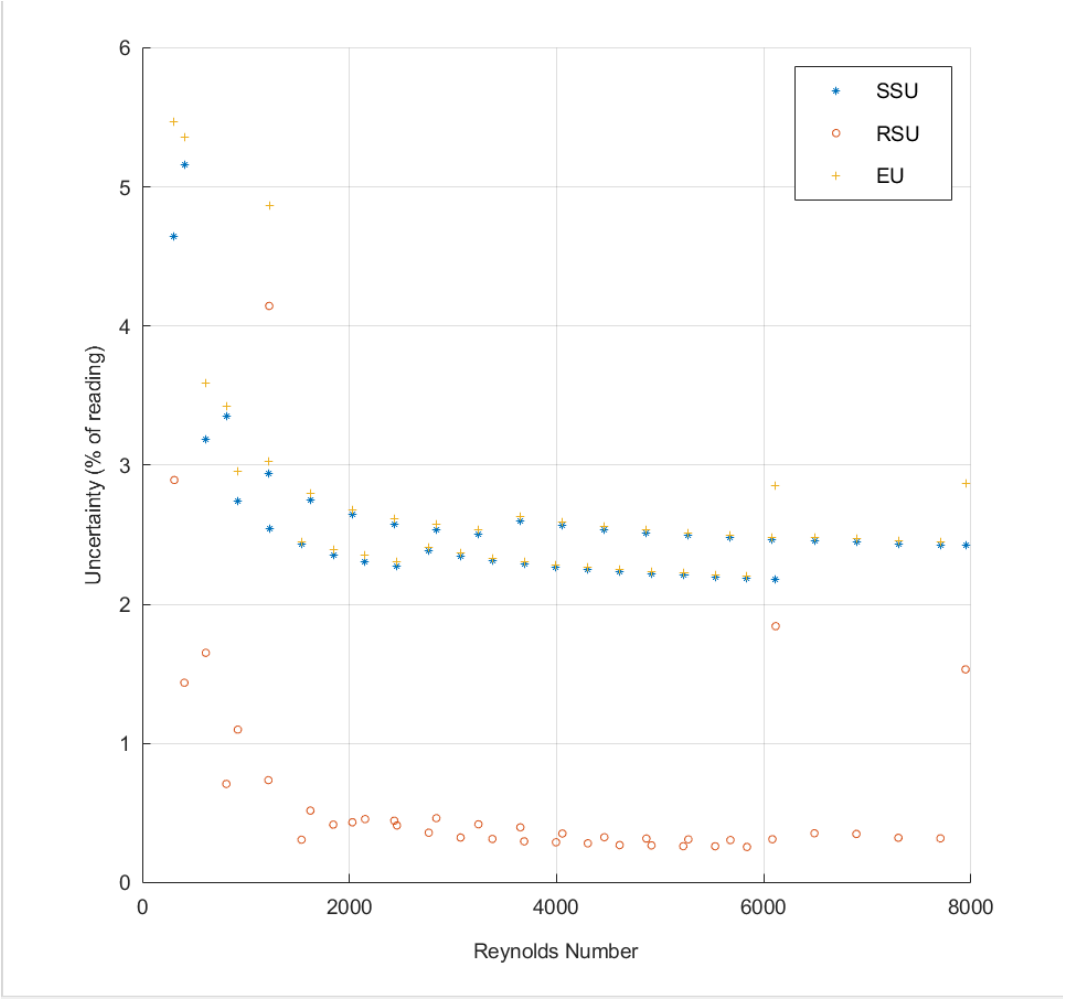

Figure 43 — Plot of expanded uncertainty of Reynolds number for smooth EMT lines

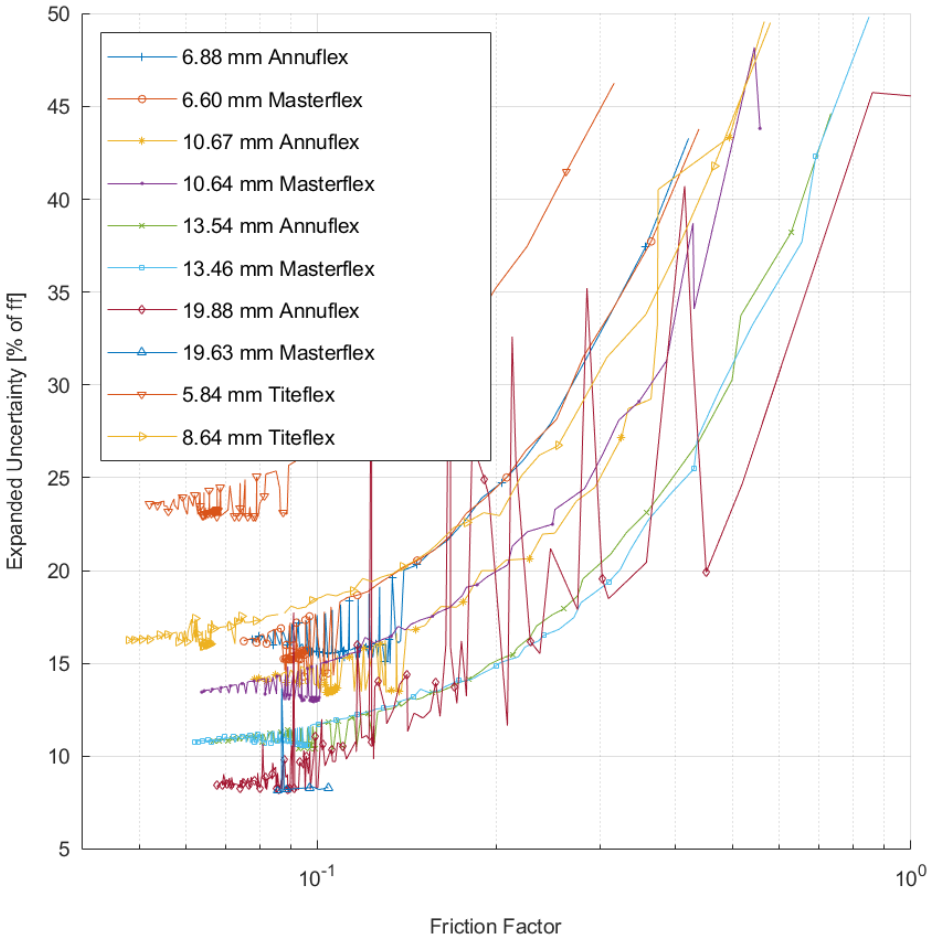

Figure 44 — Expanded Uncertainty for Friction Factor for tested corrugated pipes

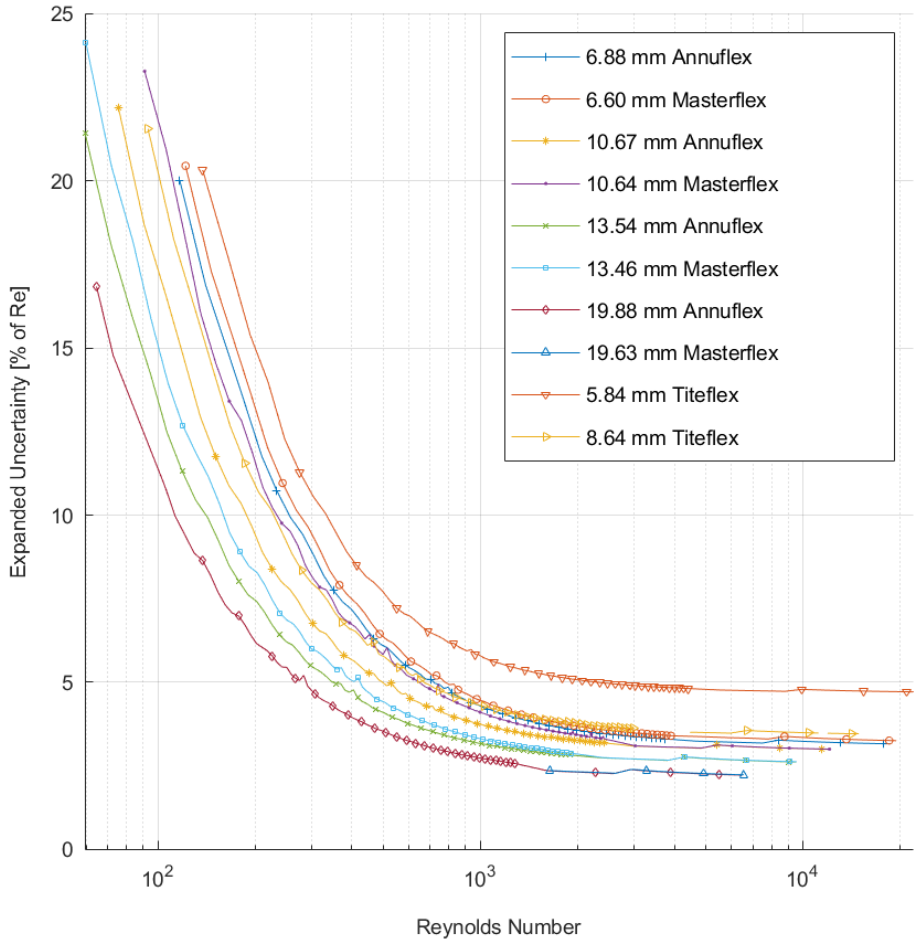

Figure 45 — Expanded Uncertainty for Reynolds Number for tested corrugated pipes

Appendix C – Plots of Results

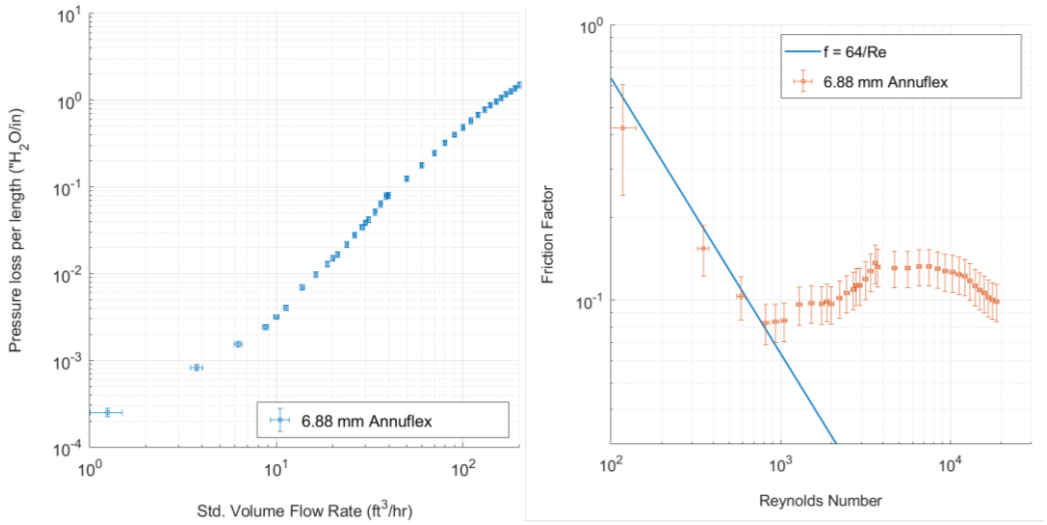

Figure 46 — 0.25" Annuflex Experimental Results

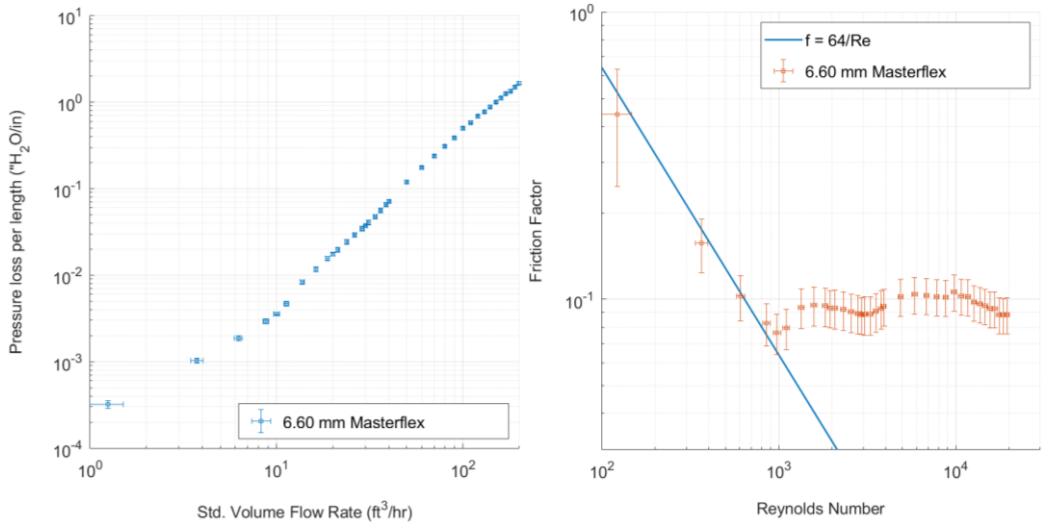

Figure 47 — 0.25" Masterflex Experimental Results

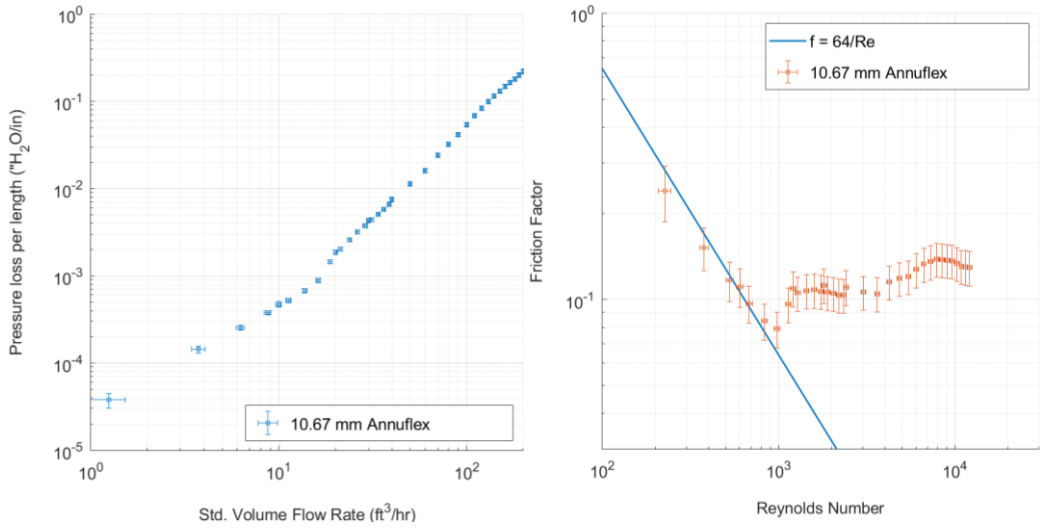

Figure 48 — 0.375" Annuflex Experimental Results

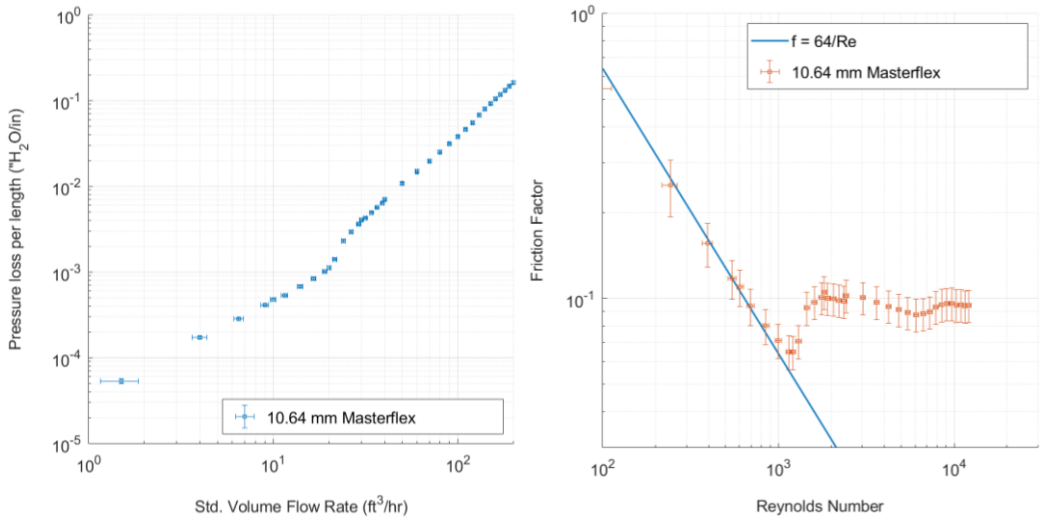

Figure 49 — 0.375" Masterflex Experimental Results

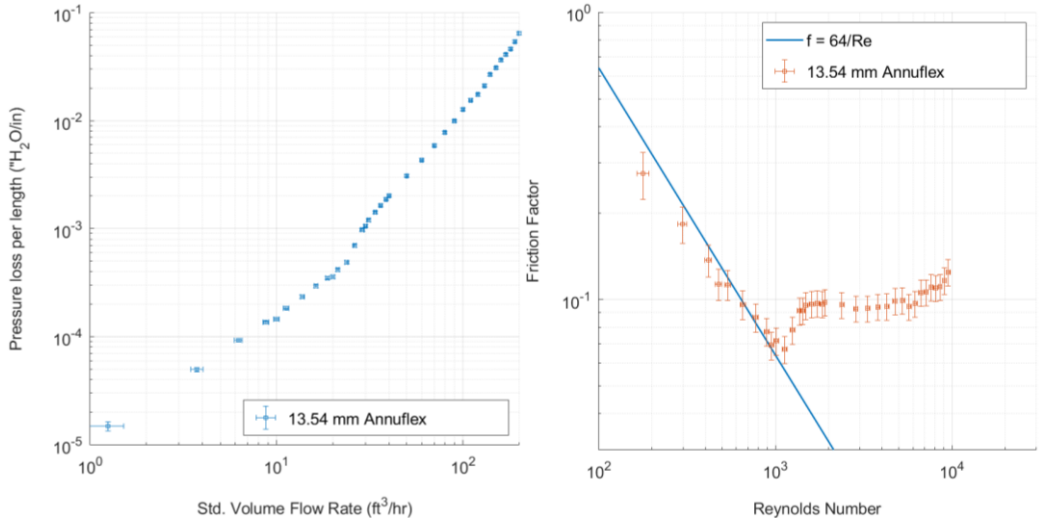

Figure 50 — 0.50" Annuflex Experimental Results

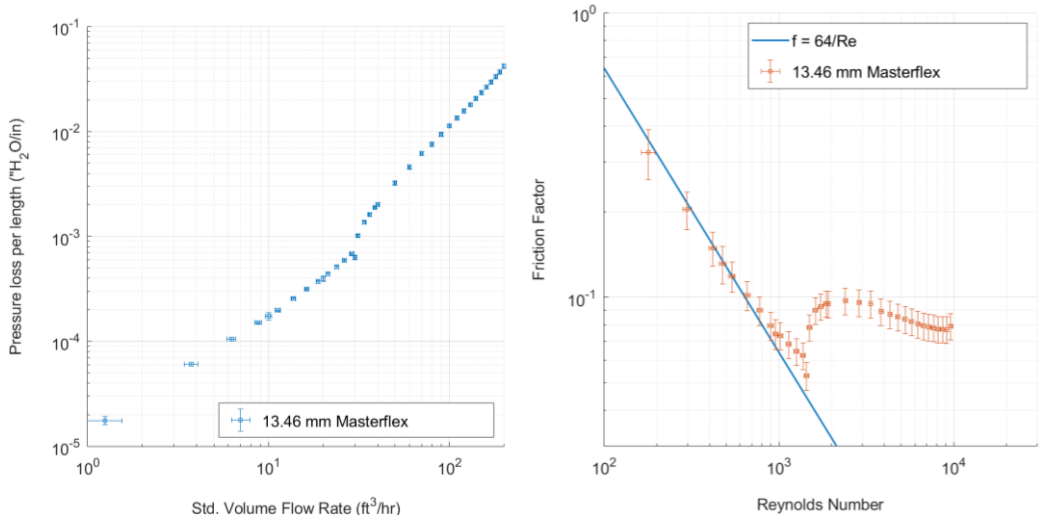

Figure 51 — 0.50" Masterflex Experimental Results

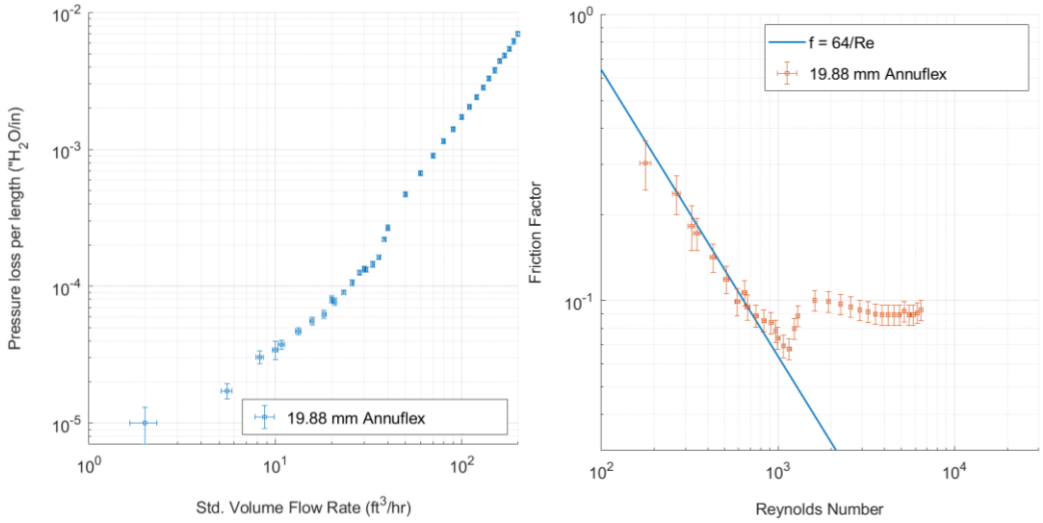

Figure 52 — 0.75" Annuflex Experimental Results

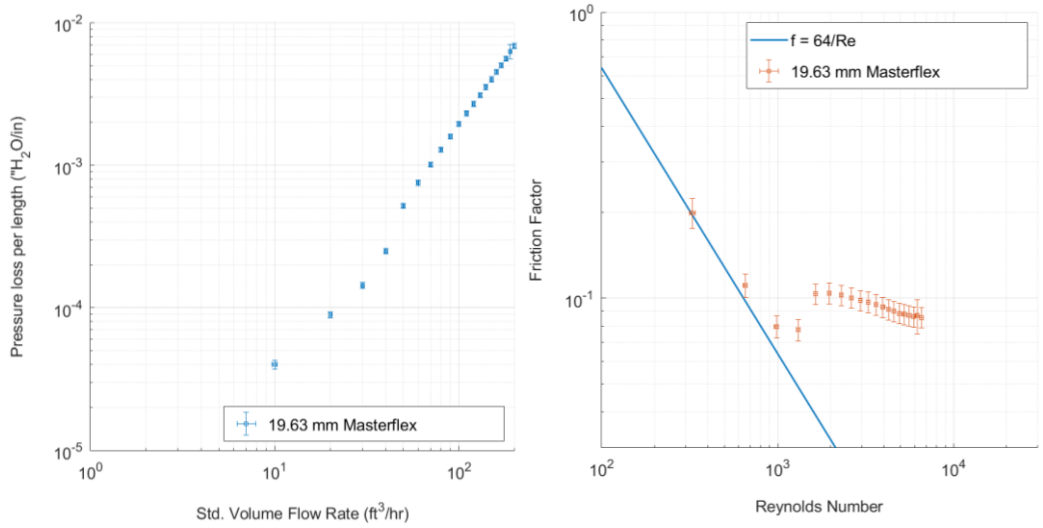

Figure 53 — 0.75" Masterflex Experimental Results

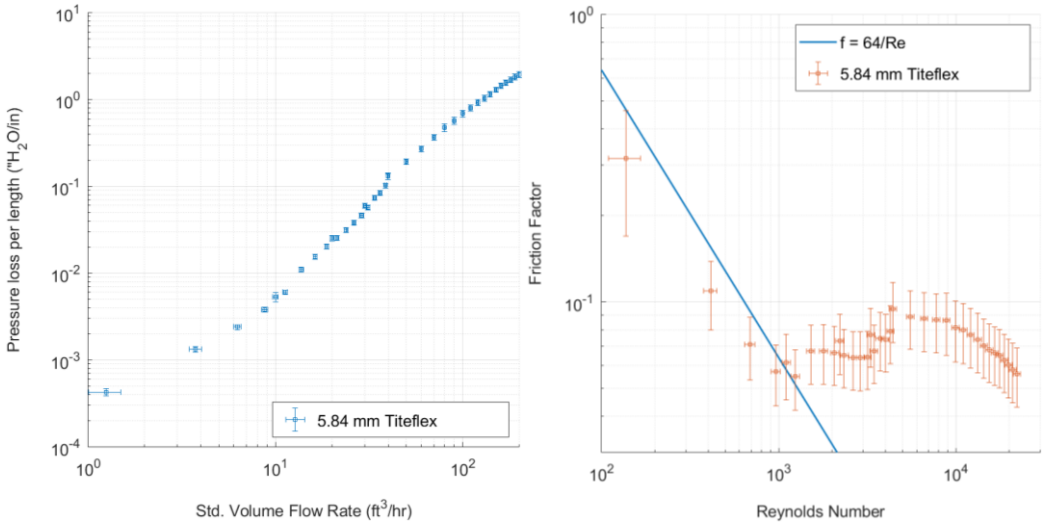

Figure 54 — 0.25" Titeflex Experimental Results

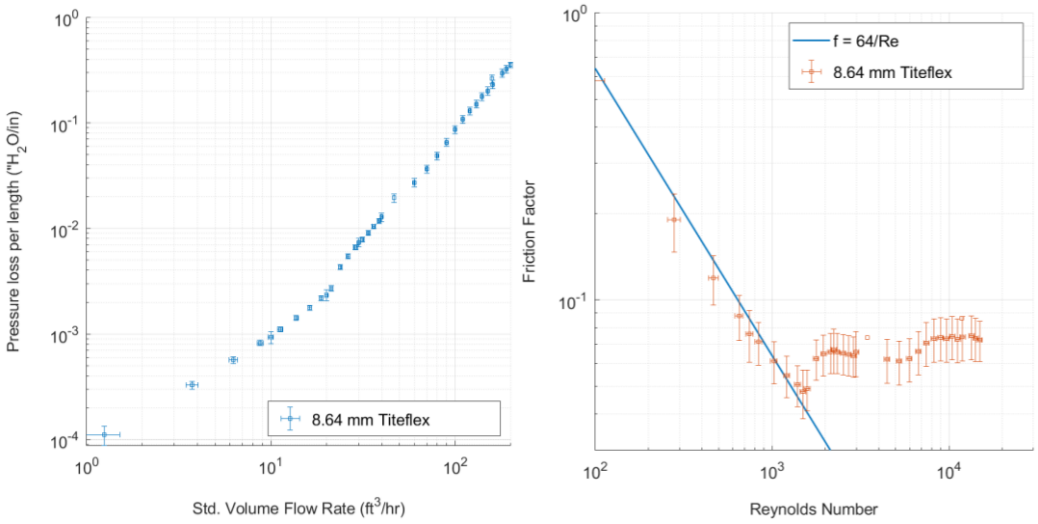

Figure 55 — 0.375" Titeflex Experimental Results

Appendix D – Tables of Results

Additional Tables of Individual Pipes

Table 12 — Final results of differential pressure per unit length (psi/in) (rows) at various flow rates (columns) for all pipes

Line Name	10	20	30	40	50	60	70	80	90	100
0.25” Annuflex #3	2.23E-04	7.09E-04	1.58E-03	2.79E-03	3.12E-03	5.89E-03	7.95E-03	1.04E-02	1.31E-02	2.23E-04
0.25” Masterflex #4	1.95E-04	5.47E-04	1.07E-03	1.83E-03	2.12E-03	5.47E-03	7.68E-03	1.01E-02	1.26E-02	1.95E-04
0.375” Annuflex #7	2.79E-05	1.21E-04	2.78E-04	5.02E-04	7.57E-04	1.09E-03	1.59E-03	2.13E-03	2.66E-03	2.79E-05
0.375” Masterflex #8	1.66E-05	3.93E-05	1.39E-04	2.28E-04	3.82E-04	5.32E-04	7.03E-04	9.04E-04	1.11E-03	1.66E-05
0.50” Annuflex #11	5.94E-06	1.35E-05	3.79E-05	6.84E-05	1.03E-04	1.45E-04	1.97E-04	2.64E-04	3.37E-04	5.94E-06
0.50” Masterflex #12	5.88E-06	1.54E-05	3.19E-05	1.09E-04	1.13E-04	1.61E-04	2.10E-04	2.70E-04	3.35E-04	5.88E-06
0.75” Annuflex #15	1.52E-06	2.42E-06	3.73E-06	8.96E-06	1.58E-05	2.18E-05	2.95E-05	3.80E-05	4.67E-05	1.52E-06
0.75” Masterflex #16	1.80E-06	3.84E-06	5.72E-06	8.68E-06	2.00E-05	2.94E-05	3.94E-05	5.01E-05	6.18E-05	1.80E-06
0.25” Titeflex #17	2.39E-04	1.02E-03	2.27E-03	4.34E-03	5.86E-03	8.71E-03	1.17E-02	1.54E-02	1.83E-02	2.39E-04
0.375” Titeflex #18	2.60E-05	1.22E-04	2.46E-04	5.44E-04	6.00E-04	8.15E-04	1.04E-03	1.36E-03	1.74E-03	2.60E-05

0.625” EMT #19	3.13E-06	5.68E-06	8.12E-06	1.02E-05	1.16E-05	1.36E-05	3.90E-05	5.05E-05	6.25E-05	3.13E-06
0.825” EMT #20	9.29E-07	1.82E-06	2.55E-06	3.09E-06	3.15E-06	3.75E-06	3.57E-06	9.50E-06	1.44E-05	9.29E-07

Line Name	110	120	130	140	150	160	170	180	190	200
0.25” Annuflex #3	1.56E-02	1.82E-02	2.11E-02	2.30E-02	2.56E-02	2.81E-02	3.08E-02	3.34E-02	3.65E-02	4.05E-02
0.25” Masterflex #4	1.64E-02	1.94E-02	2.26E-02	2.60E-02	2.94E-02	3.27E-02	3.60E-02	3.89E-02	4.24E-02	4.61E-02
0.375” Annuflex #7	3.41E-03	4.20E-03	4.94E-03	5.92E-03	6.81E-03	7.80E-03	8.97E-03	9.95E-03	1.10E-02	1.20E-02
0.375” Masterflex #8	1.34E-03	1.60E-03	1.88E-03	2.20E-03	2.55E-03	2.93E-03	3.37E-03	3.83E-03	4.33E-03	4.81E-03
0.50” Annuflex #11	4.25E-04	5.18E-04	5.81E-04	7.35E-04	9.03E-04	1.06E-03	1.23E-03	1.37E-03	1.53E-03	1.72E-03
0.50” Masterflex #12	4.08E-04	4.86E-04	5.70E-04	6.60E-04	7.54E-04	9.39E-04	1.07E-03	1.19E-03	1.33E-03	1.48E-03
0.75” Annuflex #15	5.63E-05	6.69E-05	7.83E-05	9.23E-05	1.07E-04	1.24E-04	1.40E-04	1.60E-04	1.79E-04	2.06E-04
0.75” Masterflex #16	7.47E-05	8.88E-05	1.04E-04	1.20E-04	1.37E-04	1.46E-04	1.63E-04	1.82E-04	2.03E-04	2.24E-04
0.25” Titeflex #17	2.24E-02	2.59E-02	2.97E-02	3.20E-02	3.66E-02	4.25E-02	4.79E-02	5.26E-02	5.65E-02	6.00E-02
0.375” Titeflex #18	2.33E-03	2.90E-03	3.59E-03	4.23E-03	5.08E-03	5.85E-03	6.70E-03	7.63E-03	8.64E-03	9.42E-03
0.625” EMT #19	7.52E-05	8.88E-05	1.03E-04	1.18E-04	1.34E-04	1.51E-04	1.67E-04	1.83E-04	1.96E-04	2.12E-04

0.825” EMT #20	1.78E-05	2.14E-05	2.52E-05	2.91E-05	3.32E-05	3.76E-05	4.21E-05	4.67E-05	5.15E-05	5.67E-05

Table 13 — Uncertainty of differential pressure per unit length (psi/in) (rows) at various flow rates (columns)

Line Name	10	20	30	40	50	60	70	80	90	100
0.25” Annuflex #3	1.07E-10	1.42E-09	6.02E-09	1.8E-08	2.23E-08	8.44E-08	1.79E-07	3.02E-07	5.98E-07	8.49E-07
0.25” Masterflex #4	9.12E-11	8.71E-10	4.46E-09	9.04E-09	1.99E-08	7.54E-08	1.71E-07	2.94E-07	5.63E-07	9.36E-07
0.375” Annuflex #7	2.68E-12	5.07E-11	1.85E-10	8.36E-10	1.91E-09	4.03E-09	8.43E-09	1.53E-08	4.27E-08	5.62E-08
0.375” Masterflex #8	9.6E-13	3.28E-12	6.74E-11	1.16E-10	3.2E-10	6.62E-10	1.33E-09	2.86E-09	4.33E-09	6.31E-09
0.50” Annuflex #11	1.37E-13	4.98E-13	3.18E-12	1.16E-11	3.05E-11	5.81E-11	8.44E-11	1.43E-10	2.35E-10	3.98E-10
0.50” Masterflex #12	1.25E-13	8.29E-13	2.12E-12	2.64E-11	3.63E-11	9E-11	9.07E-11	1.5E-10	2.32E-10	3.63E-10
0.75” Annuflex #15	4.34E-14	8.4E-14	6.29E-14	3.1E-13	6.69E-13	1.01E-12	1.85E-12	3.33E-12	5E-12	8.18E-12
0.75” Masterflex #16	7.27E-14	1.12E-13	1.64E-13	3.01E-13	9.06E-13	1.89E-12	3.47E-12	6.1E-12	9.23E-12	1.56E-11
0.25” Titeflex #17	2.16E-10	3.69E-09	1.26E-08	4.11E-08	8.46E-08	2.18E-07	4.82E-07	8.22E-07	1.16E-06	1.74E-06
0.375” Titeflex #18	1.44E-12	5.38E-11	1.34E-10	7.58E-10	1.19E-09	2.35E-09	3.79E-09	5.31E-09	8.37E-09	1.18E-08
0.625” EMT #19	2.95E-08	2.95E-08	2.95E-08	2.95E-08	2.95E-08	2.95E-08	2.95E-08	2.95E-08	2.95E-08	2.95E-08

0.825” EMT #20	2.95E-08	2.95E-08	2.95E-08	2.95E-08	2.95E-08	2.95E-08	3.01E-08	2.95E-08	2.95E-08	2.95E-08

Line Name	110	120	130	140	150	160	170	180	190	200
0.25” Annuflex #3	1.16E-06	1.54E-06	1.83E-06	2.27E-06	2.73E-06	3.26E-06	3.85E-06	4.6E-06	5.67E-06	6.36E-06
0.25” Masterflex #4	1.31E-06	1.77E-06	2.35E-06	2.98E-06	3.69E-06	4.49E-06	5.24E-06	6.23E-06	7.36E-06	8.46E-06
0.375” Annuflex #7	7.77E-08	1.04E-07	1.4E-07	1.75E-07	2.24E-07	2.88E-07	3.48E-07	4.22E-07	4.92E-07	5.66E-07
0.375” Masterflex #8	8.92E-09	1.07E-08	1.15E-08	1.43E-08	1.83E-08	2.42E-08	3.15E-08	4.04E-08	4.97E-08	6.75E-08
0.50” Annuflex #11	6.64E-10	8.34E-10	1.54E-09	2.33E-09	3.2E-09	5.2E-09	6.03E-09	7.36E-09	8.72E-09	1.06E-08
0.50” Masterflex #12	5.78E-10	7.97E-10	1.25E-09	1.63E-09	2.64E-09	3.88E-09	4.5E-09	6.16E-09	6.9E-09	8.07E-09
0.75” Annuflex #15	1.15E-11	1.84E-11	2.53E-11	3.43E-11	4.55E-11	4.44E-11	5.5E-11	7.43E-11	8.82E-11	1.11E-10
0.75” Masterflex #16	2.19E-11	3.75E-11	4.97E-11	6.52E-11	7.5E-11	9.26E-10	9.23E-10	9.42E-10	2.19E-09	3.77E-09
0.25” Titeflex #17	2.32E-06	3.06E-06	3.54E-06	4.62E-06	6.23E-06	7.93E-06	9.57E-06	1.11E-05	1.25E-05	1.52E-05
0.375” Titeflex #18	1.88E-08	3.12E-08	4.28E-08	6.94E-08	9.11E-08	1.18E-07	1.8E-07	2.3E-07	2.72E-07	3.46E-07
0.625” EMT #19	2.95E-08	2.95E-08	2.95E-08	2.95E-08	2.95E-08	2.96E-08	2.95E-08	2.96E-08	2.96E-08	2.96E-08
0.825” EMT #20	2.95E-08	2.95E-08	2.95E-08	2.95E-08	2.95E-08	2.95E-08	2.95E-08	2.95E-08	2.95E-08	2.95E-08

Appendix E – Plots of CFD Results

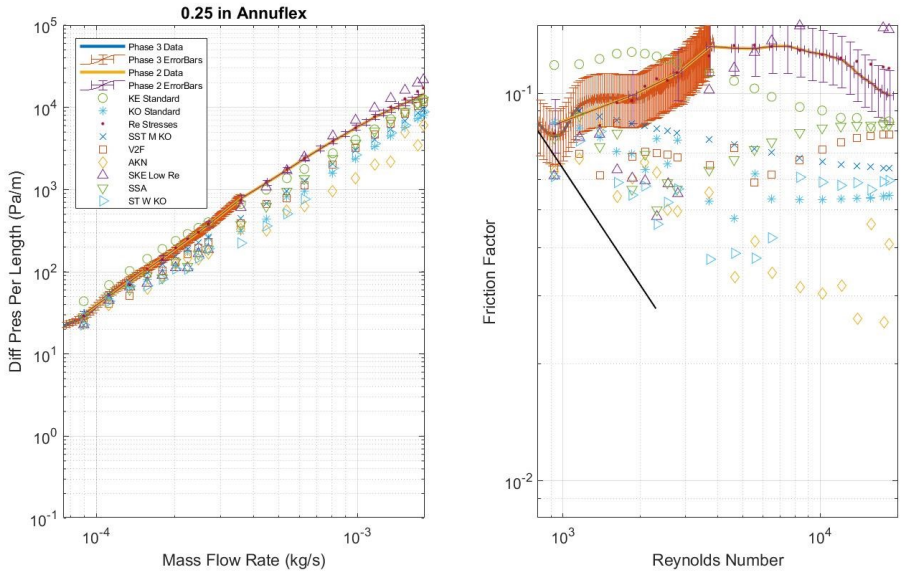

Figure 56 — CFD compared to experimental results for 0.25" Annuflex

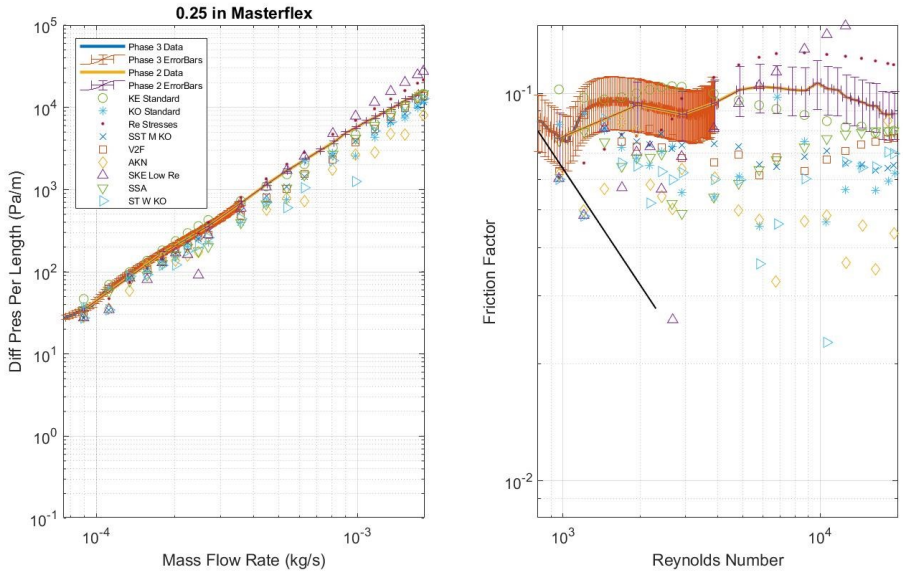

Figure 57 — CFD compared to experimental results for 0.25" Masterflex

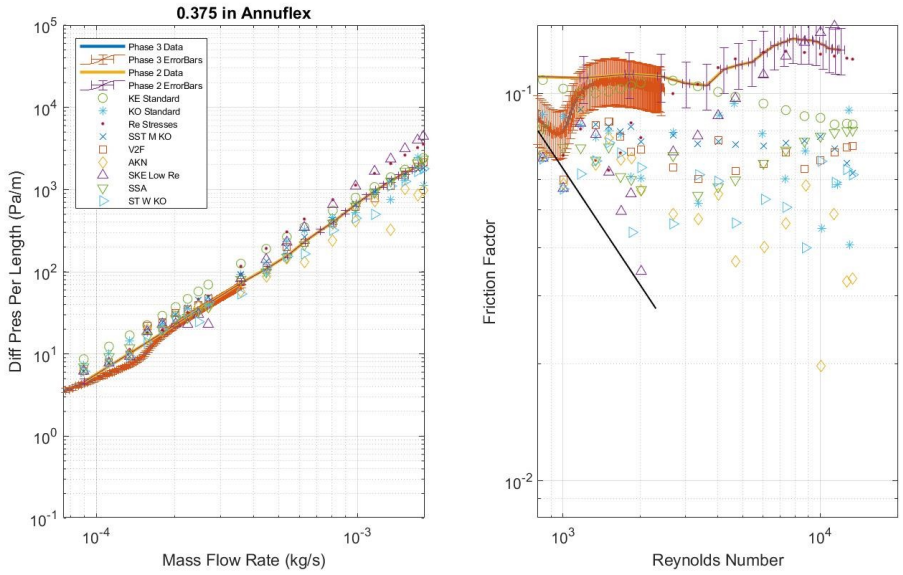

Figure 58 — CFD compared to experimental results for 0.375" Annuflex

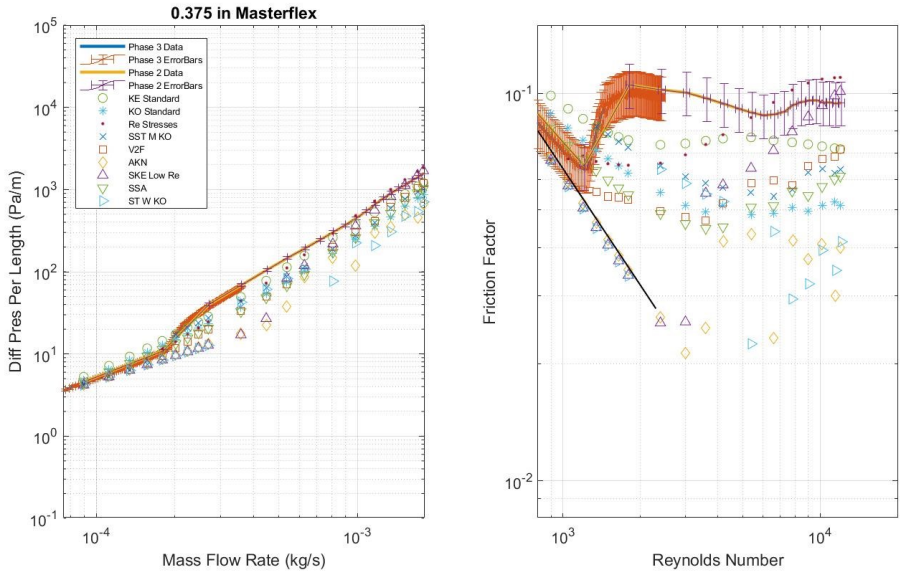

Figure 59 — CFD compared to experimental results for 0.375" Masterflex

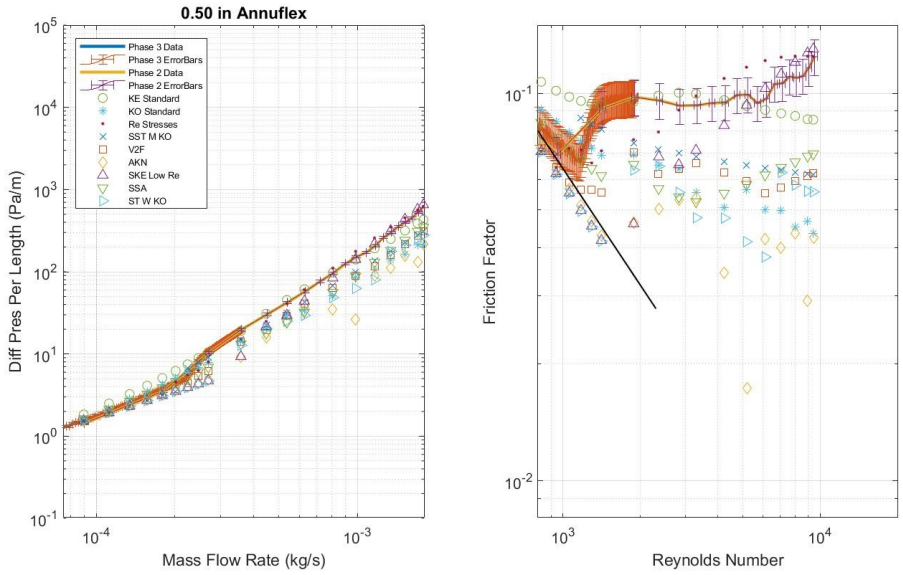

Figure 60 — CFD compared to experimental results for 0.50" Annuflex

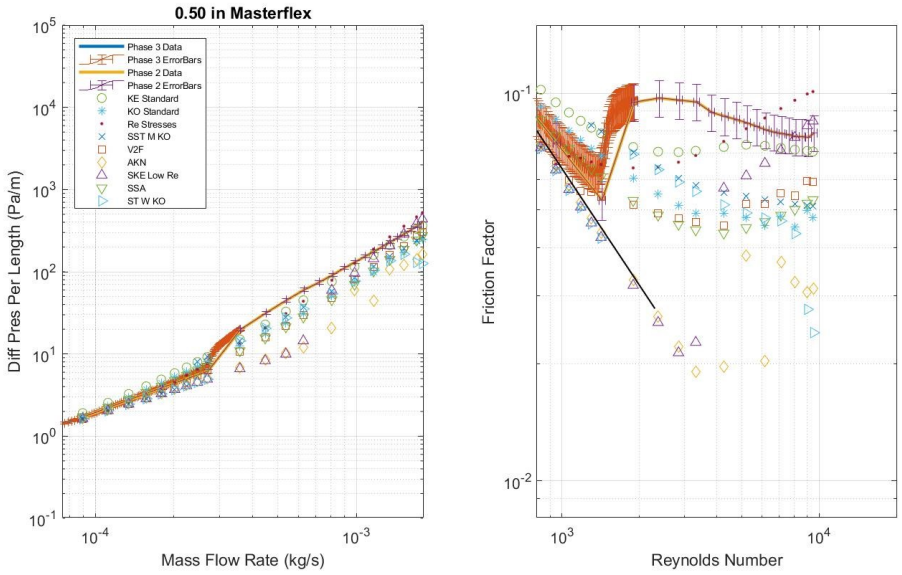

Figure 61 — CFD compared to experimental results for 0.50" Masterflex

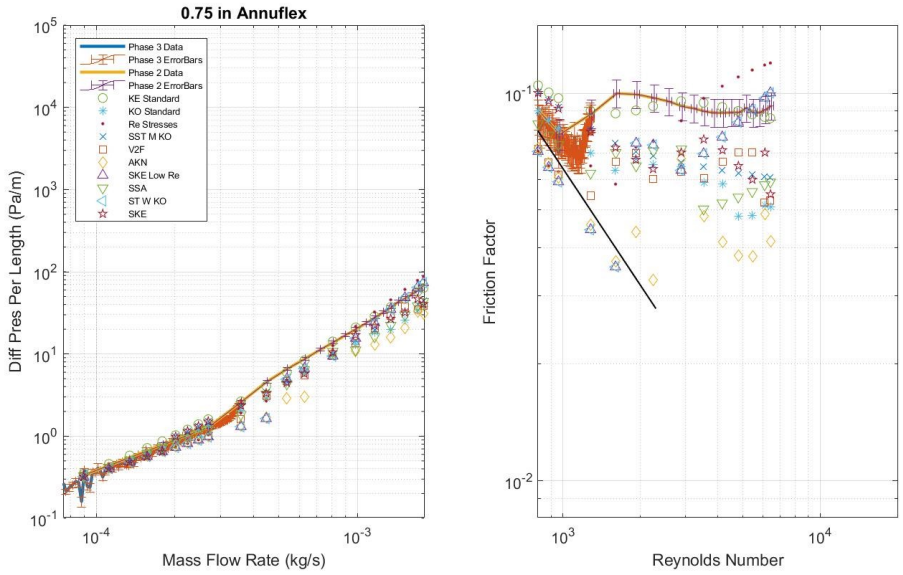

Figure 62 — CFD compared to experimental results for 0.75" Annuflex

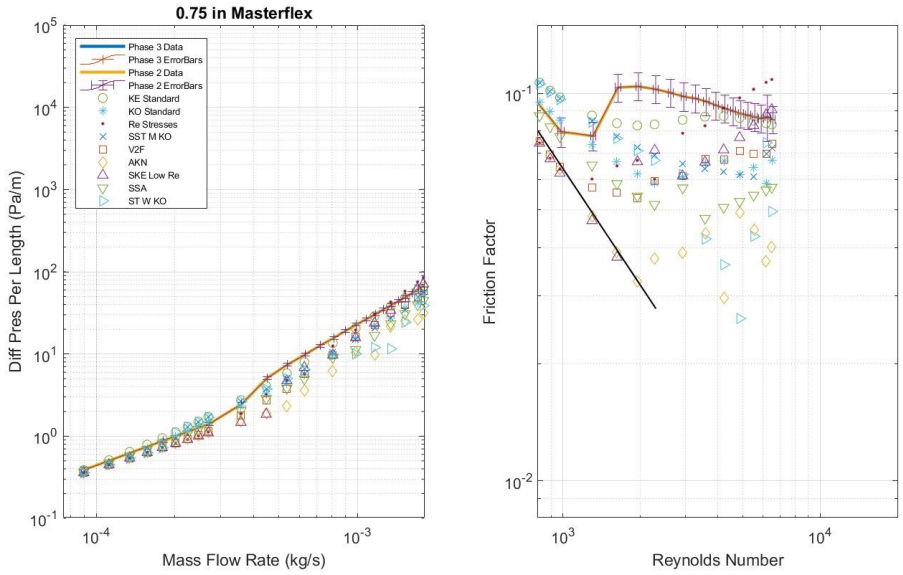

Figure 63 — CFD compared to experimental results for 0.75" Masterflex

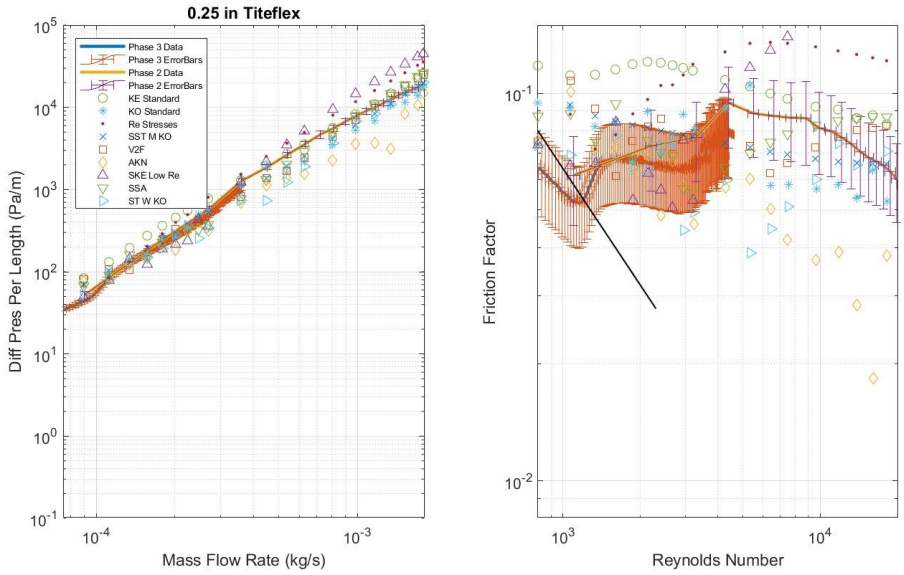

Figure 64 — CFD compared to experimental results for 0.25" Titeflex

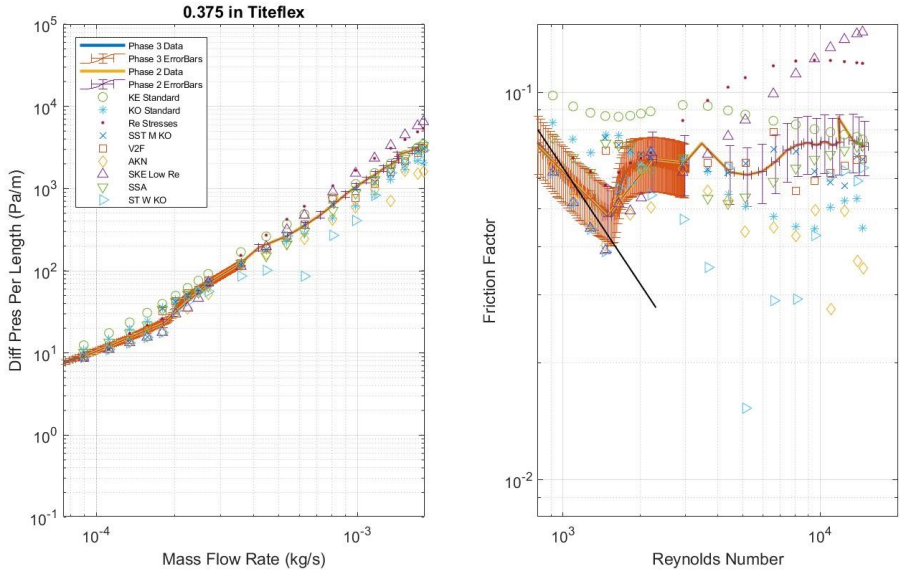

Figure 65 — CFD compared to experimental results for 0.375" Titeflex

Table 14 — Summary of CFD Turbulence Model Resulting average % error for each geometry over all flow rates

Pipe	KE Std.	KO Std.	Re Stresses	SST M KO	V2F	AKN	SKE L Re	SSA	ST W KO
0.25" Annuflex	12.5	24.3	3.6	17.2	18.3	36.2	16.1	17.2	29.0
0.25" Masterflex	7.5	16.0	11.7	14.0	11.9	24.2	19.1	12.9	20.6
0.375" Annuflex	20.7	17.4	22.8	14.2	12.1	20.6	26.0	11.1	13.3
0.375" Masterflex	11.7	18.1	9.2	13.8	15.7	30.2	16.9	17.5	25.6
0.50" Annuflex	8.7	17.1	6.7	13.2	14.7	25.0	11.4	13.7	19.7
0.50" Masterflex	10.3	15.5	9.5	14.3	15.1	30.0	18.2	15.0	19.7
0.75" Annuflex	6.5	12.7	10.0	11.5	12.6	19.5	10.3	11.7	10.8
0.75" Masterflex	22.5	26.6	27.3	26.5	28.5	38.6	27.3	30.4	32.7
0.25" Titeflex	14.5	12.0	21.2	8.7	10.8	22.1	27.7	12.1	12.0
0.375" Titeflex	11.7	11.8	14.1	5.9	5.7	14.5	16.5	8.0	15.0